ABSTRACT

Title of dissertation: Precision Control of Intense Electron Beams in a Low-Energy Ring

Chao Wu, Doctor of Philosophy, 2009

Directed by: Professor Eyad H. Abed
and Professor Patrick G. O'Shea
Department of Electrical and Computer Engineering
University of Maryland, College Park

Many applications of particle accelerators require beams with high intensity and low emittance in a stable fashion. An important research area involves the study of space-charge forces in beams, which are significant at low energy. Research reported in this dissertation was done on the University of Maryland Electron Ring (UMER), a particle accelerator designed for research on space-charge-dominated beams.

High-precision control of space-charge-dominated beams is very challenging. However, standard beam control approaches do not work well on UMER. This is due to UMER's unique structure, in which there are fewer beam position monitors than beam position correctors and a complex coupling between the horizontal and vertical kicker magnets. In this work, a novel beam control algorithm was developed based on the closed-orbit response matrix, and this algorithm was applied to UMER. The algorithm markedly improves UMER's multi-turn operation while reducing closed orbit distortion. Using the orbit response matrix, a diagnosis method

was developed that expeditiously detected malfunctions in components such as beam position monitors and magnets.

Space-charge forces can greatly affect the resonant properties of rings. With the electrostatic particle-in-cell code WARP, ring resonances were analyzed under a variety of conditions. This resulted in an improved understanding of and capability to predict beam losses and improve machine performance. Simulation results using WARP were obtained for several magnet models and compared with results from other simulation codes. Experimental results on resonance analysis were also given using wall current monitor signals.

PRECISION CONTROL OF INTENSE ELECTRON BEAMS IN A LOW-ENERGY RING

by

Chao Wu

Dissertation submitted to the Faculty of the Graduate School of the
University of Maryland, College Park in partial fulfillment
of the requirements for the degree of
Doctor of Philosophy
2009

Advisory Committee:
Professor Eyad H. Abed, Chair/Advisor
Professor Patrick G. O'Shea, Co-Chair/co-advisor
Professor Rami A. Kishek
Professor William S. Levine
Professor Balakumar Balachandran

ACKNOWLEDGMENT

I am deeply grateful to many people who have helped me during my study and research at the University of Maryland. I would like to thank my advisor Dr. Eyad H. Abed for his invaluable guidance and enthusiastic support to this successful completion of my Ph.D. dissertation. I would like to thank my co-advisor Dr. Patrick G. O'Shea. He has led me into the accelerator physics field and provided me a positive environment of independent research. I would like to thank Dr. Rami A. Kishek for his direct assistance in the research and patient revisions of my papers and dissertation.

I would like to thank Dr. William S. Levine and Dr. Balakumar Balachandran for serving on my Ph.D. dissertation committee. I would like to thank Dr. Gang Qu for serving on my Ph.D. proposal committee in 2007.

Moreover, I'm indebted to people working with the University of Maryland Electron Ring: Dr. Santiago Bernal, Dr. Massimo Cornacchia, Dr. Donald Feldman, Dr. Karen Fiuza, Dr. Terry Godlove, Dr. Irving Haber, Dr. David Sutter, Dr. Martin Reiser, Dr. Diktys Stratakis, Dr. Kai Tian, and Dr. Mark Walter.

I would like to thank those students I have been working together: Gang Bai, Brian Beaudoin, Eric Montgomery, Zhigang Pan, Christos Papadopoulos, Brian Quinn, Charles Thangaraj, Eric Voorhies and Hao Zhang from this group. I would like to thank many friends like Guojian Lin, Xue Mei, Peng Qiu, and many more at the Institute for Systems Research and the Department of Electrical and Computer Engineering and others at the University of Maryland. I will remember these days

forever.

I would like to thank other faculty and staff members for their help in the Department of Electrical and Computer Engineering, the Institute for Systems Research, and the Institute for Research in Electronics and Applied Physics.

Most of all, I would like to thank my wife and my family for their support and love.

Table of Contents

List of Tables

List of Figures

List of Abbreviations

UMER	University of Maryland Electron Ring
ISR	Institute for Systems Research
IREAP	Institute for Research in Electronics and Applied Physics
BPM	Beam position monitor
PIC	Particle-in-cell
FODO	A quadrupole combination which control beam envelope
WARP	A beam simulation code
SLAC	Stanford Linear Accelerator Center
FFT	Fast Fourier Transform

Chapter 1

Background and Motivation

A particle accelerator is a device that uses electric fields to accelerate charged particles in vacuum to high speeds and to transport them in guided fields. There are two basic types of accelerators: linear accelerators and circular accelerators. Linear accelerators, depicted in the left diagram of Figure 1.1, are long and present a relatively simple beam steering problem. Circular accelerators, depicted in the right diagram of Figure 1.1, are more complicated to control.

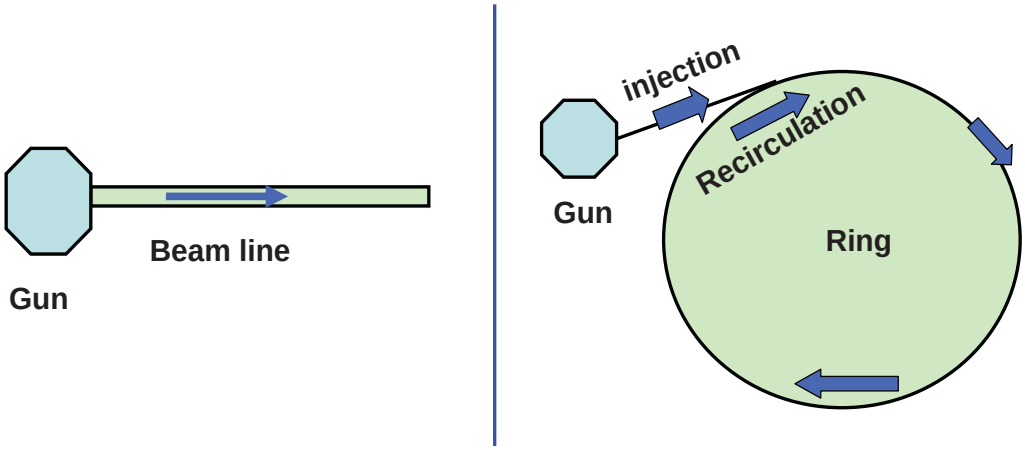

Figure 1.1: Left: Schematic of a linear accelerator. Right: Schematic of the University of Maryland Electron Ring, an example of a circular accelerator.

Particle accelerators make high-energy beams available for many important applications, ranging from basic scientific research to medical treatments. Specific applications include heavy ion fusion [1, 2], free electron lasers [3] and proton therapy

facilities [4]. The growing demand for proton therapy facilities, which are used to accurately destroy tumors with minimal harm to nearby healthy tissues, illustrates the increasing importance of this technology beyond the laboratory.

All of these applications require precise control of beam generation, transportation, acceleration and targeting; it takes effort to produce a high quality beam of a desired distribution and intensity. Rings are difficult to control because they usually include many different components, such as bending magnets, focusing magnets, RF cavities, among others [5]. Moreover, beams themselves are quite complicated. A beam usually consists of millions of particles, each of which has its own dynamics and interacts with other particles. The forces between particles in a beam, called space-charge forces, can affect the overall properties of the beam. Since the 1920s, there have been many efforts around the world devoted to increasing particle energy, controlling beams precisely, and understanding beam dynamics [6].

Circular accelerators have been limited in beam current and brightness by the effects of space-charge tune shift [7]. In simple terms, *tune* is the number of oscillations of the beam per turn. This quantity characterizes the machine's stability, and certain undesirable tune values should be avoided for stable operations. A detailed introduction to accelerator tune will be presented in Chapter 3. When beams with different space-charge are operated in the same accelerator condition, the tune values will be different. This difference is called the tune shift. Tune shift can lead to dangerous beam resonances and beam loss [7, 8, 9]. Therefore, it is useful to understand how space-charge forces affect beam dynamics through theory, simulation and experiment. We use the dimensionless intensity parameter χ [7]

to characterize the strength of the space-charge forces in the beam. The quantity $\chi \in [0, \quad 1]$ is the ratio of the space-charge forces to the external focusing force at the beam; $\chi = 1$ means the space charge forces fully determine the beam dynamics, while $\chi = 0$ means the space charge forces are negligible. It is advantageous to have a machine that can operate in both regimes, especially the space-charge-dominated regime. The University of Maryland Electron Ring (UMER) is such a machine, designed to offer a unique opportunity to study intense beam physics.

1.1 The University of Maryland Electron Ring

UMER is a low-energy, high-current circular accelerator intended for the study of beam physics. This accelerator has been used for scaled studies that are applicable to many larger accelerators; this is especially so for space-charge studies [10, 11, 12, 13]. A recent photograph of UMER is shown in Figure 1.2. The UMER beam current can be varied from 0.6 mA to 100 mA, which covers a wide range of space charge levels.

In order to conduct experiments with space-charge-dominated beams at UMER, we need the beam to circulate the ring for many turns with minimal beam loss. Beam control is crucial to achieve these. However, there are several difficulties with beam control in UMER. Because of the limited number of beam position monitors (BPMs), the beam is under-diagnosed. Power saturation of the magnets is another limiting factor for achieving optimal ring performance. Furthermore, unknown disturbances, magnet errors, and coupling between horizontal and vertical kickers complicate the

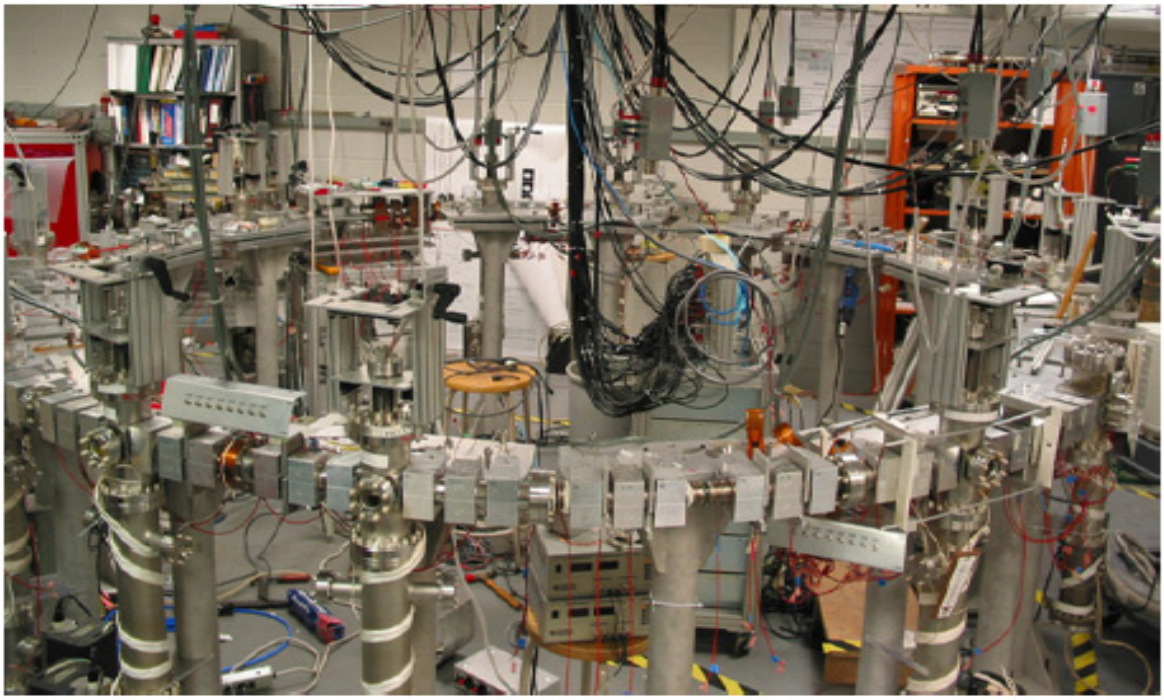

Figure 1.2: Photograph of the University of Maryland Electron Ring.

control effort.

It is important to understand and predict beam losses, and improve machine performance for high intensity synchrotrons or storage rings. There are many causes for beam loss such as mechanical misalignments, imperfect beam steering, and unstable operating points. If the ring quadrupoles operate at certain undesirable values, the multi-turn beam quality will deteriorate quickly. When space-charge forces are taken into consideration, the induced tune shift affects the beam quality and shifts the resonance point [7, 8, 9]. In order to maximize the number of turns and minimize the beam loss, we need to identify each possible reason for beam loss.

1.2 Previous Work on Beam Control

Excellent beam steering can guarantee good multi-turn beam operation. There have been many algorithms available for beam steering: harmonic correction [14], eigenvector method [15], orbit response matrix and LOCO [16, 17], etc. However, these algorithms cannot be directly applied to UMER because of its unique structure, which will be discussed in Chapter 2.

Control of UMER beams, in simulation and experiment, has been addressed by other researchers. There were two researchers, Li [18] and Walter [19], who worked on beam control of UMER in the past. Li developed algorithms for beam steering and envelope matching before the UMER ring was closed. His control technique used the linear optics theory and involved scanning the quadrupoles, taking beam photos at downstream phosphor screens, and computing resulting beam position changes. His solution achieves a local minimum of beam positions in BPMs with respect to half of the quadrupoles in the ring. Walter further developed this approach and set up solutions for multi-turn operations, but he found it difficult to implement it for closed-orbit correction [19, 20, 21]. The fast drop of beam current measured by the wall current monitor begs for the development of new control algorithms that improve multi-turn operation.

In addition, work has been done to understand various aspects of beam behavior, especially of ring resonances [23, 24, 25]. Various simulation codes have been used to model the injector, ring, and recirculation, both in single-particle simulation and in space-charge simulation. There are three main simulation codes used

by UMER researchers: WARP [22], WinAgile [23] and Elegant [26]. WARP is a particle-in-cell (PIC) code which can model the space charge force. WinAgile is a linear matrix code which treats all particles as being equivalent to a single particle. Elegant is a particle-tracking code which does not include space-charge effect. Results were reported in [23, 24, 25]. Benchmarking simulation results from different codes helps us to understand the UMER system better.

1.3 Goals and Approach

There are two primary goals we want to accomplish in this work. The first goal is to optimize the performance of UMER. The second goal is to better understand the physics within the ring. We believe this work can help others in the accelerator community and other related fields who may face similar problems.

One aspect of optimizing ring performance is to optimize beam centroid control. For centroid control, the general approaches introduced in Section 1.2 do not work on UMER. This will be discussed in Chapter 2. This motivates us to find a new method for steering the beam. Moreover, it is desirable to develop a control algorithm which can accommodate system changes such as replacement of malfunctioning quadrupoles or changes in laboratory layout.

Measuring tune and understanding resonances constitute our second goal. The results of our study of tune reveal discrepancies between simulation and experiment. Understanding these discrepancies requires effort in both simulation and experiment. Our approach is to use the 3-D simulation code WARP and compare with other

simulation codes and experiment to find a model for UMER that has high fidelity.

1.4 Outline of Dissertation

The dissertation is organized as follows.

In Chapter 2, we discuss the challenges of beam control and simulation in UMER. Challenges in simulation require us to refine our modeling of several types of magnets, including quadrupoles, steering dipoles, and pulsed dipoles as well as the noise associated with magnets and power supplies. Trying to decrease the discrepancy between simulation and experiment drives us to better understand the UMER system. Challenges in experiment, especially in beam centroid control, require us to understand the system, develop improved diagnostics, refine control algorithms, and achieve a superior control solution.

In Chapter 3, we focus on resonance analysis and investigation of tune. When the tune of an accelerator is close to an integer or half-integer or other resonance values, multi-turn beam operation becomes difficult since any disturbance can destabilize the beam, leading to large centroid oscillation and emittance growth, which result in early beam loss. By using wall-current monitor signals and BPM signals, we can effectively detect these resonances. At the same time, tune is a very important parameter for accelerators and should be measured precisely. However, due to the limitations of multi-turn operation, it is difficult to obtain a precise tune value. Beam loss, beam distribution change and BPM signal noise can all contribute to the discrepancy between experimental and theoretical values. By improving the mod-

eling of the magnets, we close the gap between simulation and experiment for the calculated tune.

In Chapter 4, we introduce an approach to system diagnosis for UMER. This method has been developed based on the orbit response matrix. Because circular accelerators are constructed to be periodic from one chamber to another, corresponding elements in the response matrix should be identical or nearly so. If there is something wrong with the quadrupoles, dipoles, BPMs or other elements, the periodicity will be broken, which will be reflected in the response matrix. We have applied the method introduced in this chapter to UMER, successfully detecting and localizing mechanical and electrical problems in BPMs and dipoles. Previously, there was no systematic method for locating sources of problems in UMER operation.

In Chapter 5, we identify major control problems for UMER and propose different approaches to address these problems. The problems in injection differs from those in the ring. Each problem has unique characteristics and requires a tailored approach. Nonlinearities, coupling, noise, model mismatch and other factors complicate the analysis. The widely used algorithm based on the orbit response matrix [16] does not provide a satisfactory solution. Hence, through introduction of the closed orbit response matrix, a new iterative control algorithm is proposed. Application of this new algorithm has resulted in significant improvement of multi-turn operation and reduction of closed orbit distortion.

Finally, in Chapter 6 we summarize the contribution of this dissertation and provide suggestions for future research.

Chapter 2

Background and Issues of UMER Beam Control

There are two main challenges in improving the performance and understanding the University of Maryland Electron Ring (UMER). One challenge is to improve beam control and the other is to understand the physics of beams with intense space charge. Addressing these challenges requires a combined approach involving modeling, simulation and experiment. The UMER research group is consistently improving the modeling of the system. For example, improved quadrupole modeling by Bernal [27] defines a new factor where the quadrupole field has a wider flat region. This modeling leads to a closer agreement between simulation and experimental results. On the one hand, improvement in the simulation codes helps us refine the modeling, which leads to a more accurate prediction of the beam dynamics. On the other hand, improvements in the experiment such as better beam centroid control, beam matching, and multi-turn operation give us a better opportunity to study the beam dynamics. Therefore, improving ring performance in experiments is interwoven with understanding the physics of the UMER in simulations.

As discussed in Chapter 1, beam control is critical to the quality of sustained beam transport over a long distance or in multi-turn operations. It includes beam centroid control and beam envelope control. In UMER, the horizontal and vertical kicker magnets are employed for beam centroid control, and the quadrupoles are

used for beam envelope control. A beam with satisfactory steering solution and matching solution results in a good ring performance, partially because it minimizes the closed orbit distortion, as discussed in Section 2.3. In the following sections, we elaborate on the problems addressed in this dissertation and also provide some necessary mathematical knowledge used in later chapters.

2.1 Layout and Key Parameters of UMER

A schematic diagram is presented in Figure 2.1 to help readers familiarize themselves with the UMER system. Most of the work focuses on using the dipoles and quadrupoles. UMER has three parts: injection, ring, and recirculation. As in Figure 2.1, The electron beam is first generated at the E-Gun, and then introduced into the ring through the matching section. After that, the beam recirculates in the ring with the help of dipoles and quadrupoles.

Some important parameters are listed in Table 2.1 for future reference, where v is the beam speed and c is the speed of light in vacuum.

The motion of each particle is characterized by six state variables (x, y, z, p_x, p_y, p_z), where (x, y, z) define the position and (p_x, p_y, p_z) define the momentum. The coordinates of beam dynamics are shown in Figure 2.2.

Assume the beam distribution $f(x, x', y, y')$ is known, then the total number of particles N, the centroid $< x >$, the beam angle $< x' >$ and the emittance ϵ_x are defined as follows, respectively.

$$\int\int\int\int f(x, x', y, y')dxdx'dydy' = N(\text{total number of particles}) \tag{2.1}$$

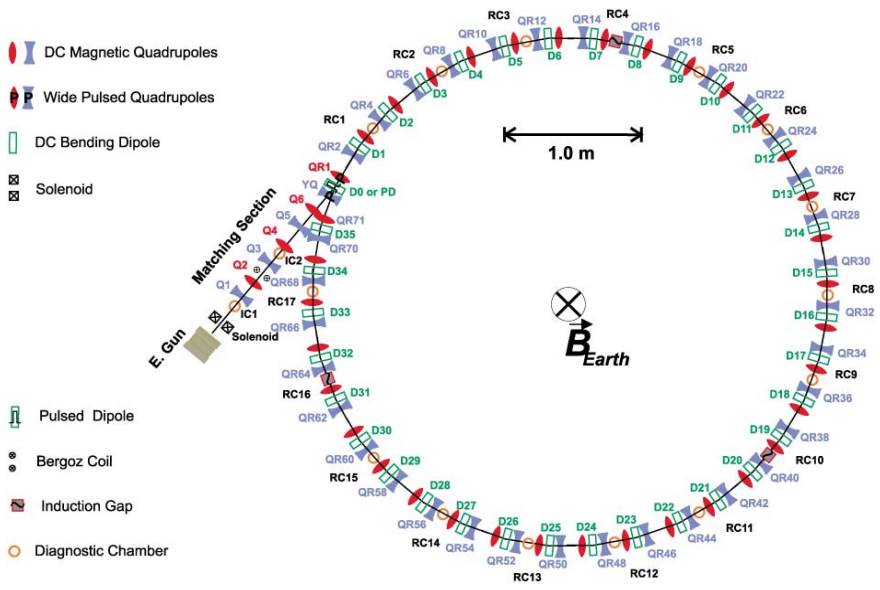

Figure 2.1: Layout of the University of Maryland Electron Ring.

$$\text{Beam centroid in x} :< x >= \frac{1}{N}\int\int\int\int x f(x,x',y,y')dxdx'dydy' \tag{2.2}$$

$$\text{Beam angle} :< x' >= \frac{1}{N}\int\int\int\int x' f(x,x',y,y')dxdx'dydy' \tag{2.3}$$

$$\epsilon_x = \sqrt{< x^2 >< x'^2 > - < xx' >^2} \tag{2.4}$$

Here Equation (2.1) is the normalization equation. Roughly speaking, the emittance describes how much area the beam occupies in the phase space. Note that centroid is not affected by space charge since the beam has zero current with respect to the centroid. For detailed information, please refer to [7].

2.2 Beam Matching Problem

In order to reduce beam rotation and beam loss in a multi-turn operation, we need to maintain a matched beam, where the beam size is kept constant in a uni-

Table 2.1: Typical UMER system parameters

Beam energy	10 keV
$\beta = \frac{v}{c}$	0.2
Beam pulse length	100ns
Ring circumference	11.52 m
Number of ring chamber	18
Lap Time	197ns
Beam size at the aperture (100 mA)	3.2 mm
Beam size at the aperture (0.6 mA)	0.25 mm

form channel. In a FODO section (focusing quadrupole-drift-defocusing quadrupole-drift), the beam is matched when the external focusing force on average equals the internal defocusing force in the beam [7]. In Chapter 5, we will present a more detailed introduction of this.

There are three matching problems to be solved: injection matching, ring matching, and recirculation matching. Injection matching is crucial to the quality of the multi-turn operation. In the UMER injection, there is only one beam position monitor or one phosphor screen available, and they cannot be used at the same time. This measurement limitation constrains our ability to calibrate the beam and test how well the matching solution is. We have to use BPMs and phosphor screens far

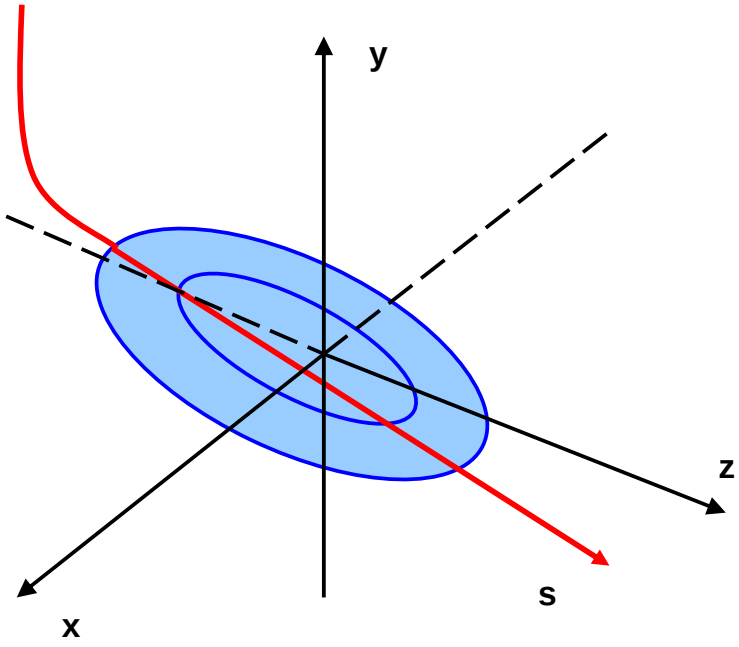

Figure 2.2: Coordinates of beam dynamics, where x and y define the transverse direction, z defines the longitudinal direction, and s is the actual direction where beam travels.

from the injection to assist in beam matching. In the ring, each chamber has four quadrupoles and these four quadrupoles are connected in series to the same power supply with alternating polarity. Usually, all ring quadrupoles are set to the same current. So beam matching in the ring is relatively simple. In the recirculation, there are two specially designed quadrupoles (YQ and QR_1) which are different from the conventional UMER quadrupoles since they focus and bend the beam. These two magnets make beam matching difficult by coupling beam matching with beam steering [28].

2.3 Beam Steering Problem

Long distance beam transport requires beam centroid to follow a designed orbit as closely as possible, which requires optimal beam steering. Many efforts by Li [18] and Walter [19] have been invested in beam steering at UMER. Li [18] used the beam based alignment to steer the beam along half the distance of the ring using phosphor screen when the ring was still under construction and was not closed yet. After Li left the group, Walter continued the steering task. Walter [19, 20, 21] used the quadrupole scan technique and the BPMs to find centers of quadrupoles from one quadrupole to another, which rendered a coarse steering solution, and set up an initial complete beam steering configuration . This method does not offer a good multi-turn solution. Although Walter's approach works for beam steering, they either lead to a local optimal steering solution or cannot converge easily, or even diverge. This will be discussed with more details in Chapter 5.

In the beam-based alignment above, there was an assumption for convenience that the horizontal and vertical beam steering are decoupled [18, 19]. However, this assumption is unduly optimistic. In Chapter 4, we observe a strong coupling in the injection and a weaker coupling in the ring in experiment. This is one reason why beam control results obtained in previous beam steering solutions, which assume decoupling, are far from perfect.

The paucity of BPMs is another big problem for beam control. In larger accelerators such as SLAC [4], the beam position monitors are distributed densely such that there is one BPM per quadrupole. However, UMER does not have many

BPMs because of limited space for the ring construction. At UMER, no quadrupoles contain BPMs. There are 14 BPMs and 72 quadrupoles in the ring. The BPMs are not co-located with the quadrupoles. In the UMER injection line, there is only one BPM, 6 quadrupoles and 13 steering dipoles. It is difficult to distinguish the individual dipole effect through one BPM or phosphor screen only. Then we have to use downstream BPMs in the ring to assist in this calibration. In addition, there is a complicated beam transport line between the injection and the ring. This transport line is imperfectly calibrated because of two magnets YQ and QR_1 [28].

We will present an approach for beam steering that can overcome these difficulties in Chapter 5.

2.4 Closed Orbit Distortion

Let us denote the beam centroid position and angle in one transverse direction (x direction) in the beam line as $(x(s), x'(s))$ with the initial beam position and angle $(x(0), x'(0))$. Assume the beam transfer matrix (defined in the next section) for the ring is M, after one turn, the beam positions are

$$\begin{cases} x(s) = Mx_0(s) \\ x'(s) = Mx'_0(s) \end{cases} \tag{2.5}$$

The same principle applies to the y direction in the transverse space for $(y(s), y'(s))$ and $(y(0), y'(0))$.

If the following equations are satisfied

$$x(C) = x(0), x(C) = x'(0) \quad \text{and} \quad y(C) = y(0), y'(C) = y'(0) \tag{2.6}$$

where C is the circumference of the ring, we claim the orbit is closed. Otherwise, the orbit is distorted. The objective of beam centroid control or beam steering is to minimize the distortion of the orbit such that the beam follows the design orbit [29].

2.5 Mathematical Background

Two mathematical terms, *transfer matrix* and *singular value decomposition*, which will be used in later chapters, are introduced as follows.

2.5.1 The Transfer Matrix

The concept of the transfer matrix is fundamental to many theories of beam transport and simulation codes in beam physics [5, 7, 33].

The matrix formalism in linear beam dynamics assumes that the magnet strength parameters are constant within each individual magnet. The particle trajectory can be represented by analytical functions within each uniform element of a transport line. The particles in the beam are treated as a single particle, i.e., the ensemble of particles is assumed to behave like a single particle.

The coordinates for typical beam optics are as shown in Figure 2.2 in previous section. The transverse beam dynamics are described in the $x-y$ plane. The longitudinal dynamics are described in the z direction. Here, we neglect the longitudinal beam dynamics.

For simplicity, three basic and widely used types of beam line elements are

introduced in this section. They are the drift space as shown in Figure 2.3, the quadrupole magnet as shown in Figure 2.5 and the bending magnet as shown in Figure 2.4. Assume the initial beam condition is $(u(s_0), u_0'(s))$ where $u(s_0)$ is the beam position at the start and $u'(s_0)$ is the beam angle at the start. The beam profile is $(u(s), u'(s))$ after the last magnet.

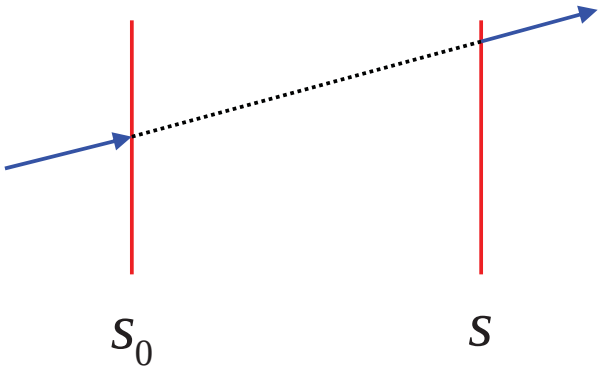

Figure 2.3: Beam traveling in a drift space. There is empty space between the two vertical lines.

A drift space is an empty space in the beam transport line. Using Figure 2.3, we have

$$\begin{bmatrix} u(s) \\ u'(s) \end{bmatrix} = \begin{bmatrix} 1 & L \\ 0 & 1 \end{bmatrix} \begin{bmatrix} u(s_0) \\ u_0'(s) \end{bmatrix} = M_{\text{drift}} \begin{bmatrix} u(s_0) \\ u_0'(s) \end{bmatrix} \tag{2.7}$$

where L is the drift space length.

A sector dipole bends the beam. As shown in Figure 2.4, we have

$$\begin{bmatrix} u(s) \\ u'(s) \end{bmatrix} = \begin{bmatrix} cos\theta & \rho sin\theta \\ -\frac{1}{\rho} sin\theta & cos\theta \end{bmatrix} \begin{bmatrix} u(s_0) \\ u_0'(s) \end{bmatrix} = M_{\text{dipo}} \begin{bmatrix} u(s_0) \\ u_0'(s) \end{bmatrix} \tag{2.8}$$

where $\theta = \frac{L}{\rho}$ is the orbiting angle and ρ is the bending radius. In the small-angle

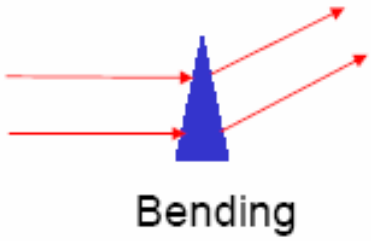

Figure 2.4: Beam traveling through a bending dipole.

approximation, the transfer matrix becomes

$$M_{\text{dipo}} = \begin{bmatrix} 1 & L \\ 0 & 1 \end{bmatrix} \tag{2.9}$$

where L is the length of the dipole. This means the effect of a dipole with a small bending angle is equivalent to that of a drift space.

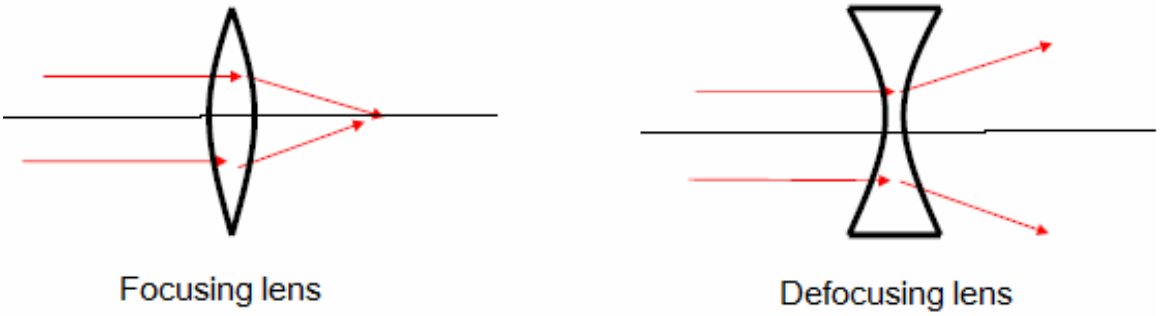

Figure 2.5: Beam traveling through a quadrupole. Left is a focusing lens. Right is a defocusing lens.

The quadrupole magnet focuses the beam in one direction and defocuses the beam in the other direction as shown in Figure 2.5. κ_0 is the focusing or defocusing functions of the quadrupole. In the focusing plane, the beam is focused and $\kappa_0 > 0$.

We have

$$\begin{bmatrix} u(s) \\ u'(s) \end{bmatrix} = \begin{bmatrix} cos\sqrt{\kappa_0}L & \frac{1}{\sqrt{\kappa_0}}sin\sqrt{\kappa_0}L \\ -\sqrt{\kappa_0}sin\sqrt{\kappa_0}L & cos\sqrt{\kappa_0}L \end{bmatrix} \begin{bmatrix} u(s_0) \\ u'_0(s) \end{bmatrix} \tag{2.10}$$

In the defocusing plane, the quadrupole defocuses the beam and $\kappa_0 < 0$. We have

$$\begin{bmatrix} u(s) \\ u'(s) \end{bmatrix} = \begin{bmatrix} cosh\sqrt{-\kappa_0}L & \frac{1}{\sqrt{-\kappa_0}}sinh\sqrt{-\kappa_0}L \\ -\sqrt{-\kappa_0}sinh\sqrt{-\kappa_0}L & cosh\sqrt{-\kappa_0}L \end{bmatrix} \begin{bmatrix} u(s_0) \\ u'_0(s) \end{bmatrix} \tag{2.11}$$

With the thin lens approximation $L \to 0$, we have

$$M_{\text{focusing}} = \begin{bmatrix} 1 & 0 \\ -\frac{1}{f} & 1 \end{bmatrix} \quad \text{and} \quad M_{\text{defocusing}} = \begin{bmatrix} 1 & 0 \\ \frac{1}{f} & 1 \end{bmatrix} \tag{2.12}$$

where f is the focal length given by $f = lim_{L\to 0}\frac{1}{|\kappa_0|L}$.

The matrices M_{drift}, M_{dipo} and M_{quad} are called the transfer matrices for the drift space, the dipole magnet, and the quadrupole magnet, respectively.

For a typical beam transport, we can use the above beam transfer matrices to compute the overall transfer matrix. Let's look at a beam transport system which consists of 5 magnets with drift spaces between them.

For a combination of magnets as shown in Figure 2.6, assume the beam starts from the left with initial conditions as $(x(0), x'(0), y(0), y'(0))$, and after the combined magnets, final beam conditions are $(x(s), x'(s), y(s), y'(s))$. Then, the beam

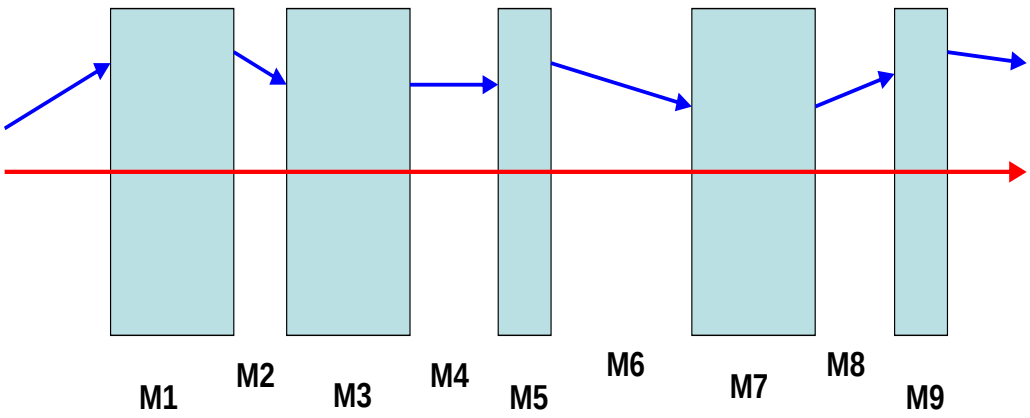

Figure 2.6: Beam traveling through several magnets. Each $M_i (i = 1, 2, ..., 9)$ represents a magnet or a drift space.

dynamics equation is expressed as:

$$\begin{bmatrix} x(s) \\ x'(s) \\ y(s) \\ y'(s) \end{bmatrix} = M9 \cdot M8 \cdots M2 \cdot M1 \cdot \begin{bmatrix} x(0) \\ x'(0) \\ y(0) \\ y'(0) \end{bmatrix} \tag{2.13}$$

Through this technique, more complicated accelerators can be modeled. And we can calculate how the beam is transported in the accelerators [7, 33].

2.5.2 Singular Value Decomposition

Singular value decomposition (SVD) has been widely used in many areas including linear algebra, signal processing, image processing, statistics, etc. [30]. This technique has been applied to beam control in the accelerator community since the 1980s.

Consider a matrix $A \in R^{m \times n}$. There exists a representation called the singular

value decomposition (SVD) as the following:

$$A = U\Sigma V^* \tag{2.14}$$

Here $\Sigma \in R^{m\times n}$ is a diagonal matrix, and $U \in R^{m\times m}$ and $V \in R^{n\times n}$ are unitary matrices, i.e, $UU^T = I, VV^T = I$, where I is the identity matrix of appropriate dimension.

The diagonal entries $s_i (i = 1, 2, ...)$ of Σ are the singular values of M, which are determined by A. When A is a nonsingular square matrix, all diagonal entries of Σ are nonzero. In general, Σ takes the form

$$\Sigma = \begin{bmatrix} s_1 & 0 & 0 & 0 & ... & 0 \\ 0 & s_2 & 0 & 0 & ... & 0 \\ 0 & ... & ... & ... & ... & 0 \\ ... & ... & 0 & s_k & 0 & ... \\ 0 & ... & ... & ... & ... & 0 \end{bmatrix} \tag{2.15}$$

Let us illustrate the SVD by decomposing the matrix

$$A = \begin{bmatrix} 1 & 2 \\ 3 & 4 \end{bmatrix} \tag{2.16}$$

The matrix A can be represented through the SVD as

$$\begin{aligned} A &= \begin{bmatrix} -0.4046 & -0.9145 \\ -0.9145 & 0.4046 \end{bmatrix} \times \begin{bmatrix} 5.4650 & 0 \\ 0 & 0.3660 \end{bmatrix} \times \begin{bmatrix} -0.5760 & 0.8174 \\ -0.8174 & -0.5760 \end{bmatrix} \\ &= U\Sigma V^* \end{aligned} \tag{2.17}$$

In this example, the columns of V form a set of orthonormal input basis vector for A; the columns of U form a set of orthonormal output basis vectors for A; and

the singular values in Σ are the gains for corresponding input vectors. A larger singular value indicates larger gain, which implies greater influence on the output.

2.6 Introduction to Beam Measurement Devices

Three types of beam measurement devices are used in UMER. The first is the beam position monitor, which measures transverse beam position without intercepting the beam. The second is the phosphor screen which takes photos of the beam, but is interceptive. The third is the wall current monitor, which measures the beam current in multi-turn beam operation. A schematic diagram of the measurement chamber of UMER is given in Figure 2.7. It consists of a beam position monitor and a phosphor screen. They are connected through a movable rod inside the chamber.

2.6.1 Beam Position Monitor

The beam position monitor (BPM) measures transverse beam position. The BPM includes four plates: top, bottom, left and right. The horizontal beam position (x) is computed using the signals from the *top* and *bottom* plates, and the vertical beam position (y) is computed using the signals of the $left$ and $right$ plates. These computations employ the following formulae:

$$x = k_2 \frac{left - right}{left + right}(horizontal) \tag{2.18}$$

$$y = k_1 \frac{top - bottom}{top + bottom}(vertical) \tag{2.19}$$

respectively, where k_1 and k_2 are corresponding coefficients. Figure 2.8 gives a screenshot of typical BPM signals as seen on an oscilloscope.

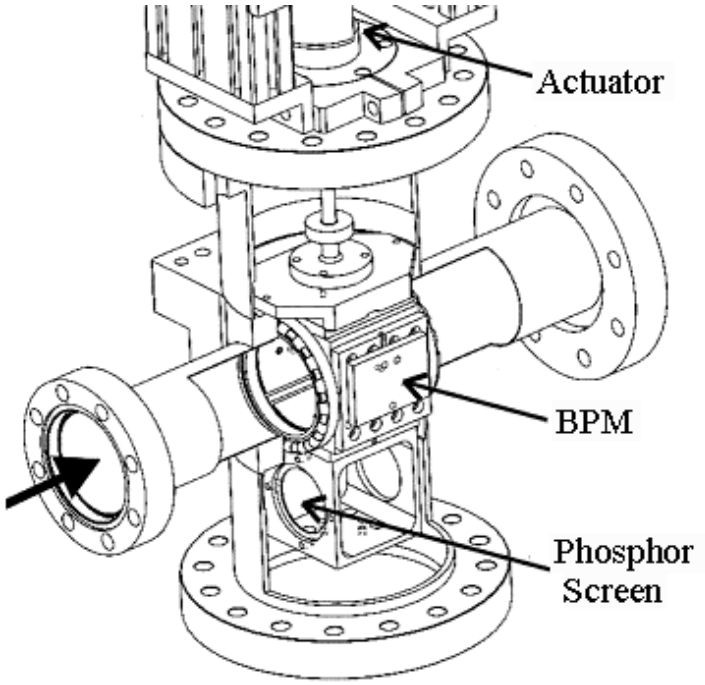

Figure 2.7: The diagnostic chamber for the University of Maryland Electron Ring.

These BPM measurements, which are non-destructive, are used in the automation of beam steering, especially for multi-turn.

2.6.2 Phosphor Screen

The phosphor screen is a specially designed screen that measures the beam profile. Through a camera mounted on the chamber, photos of the beam on the phosphor screen are taken. The beam photo reveals the beam intensity distribution, beam size, beam centroid, beam rotation, etc. The phosphor screen is mostly used for determining the beam profile, and Li [18] used it for beam control. However,

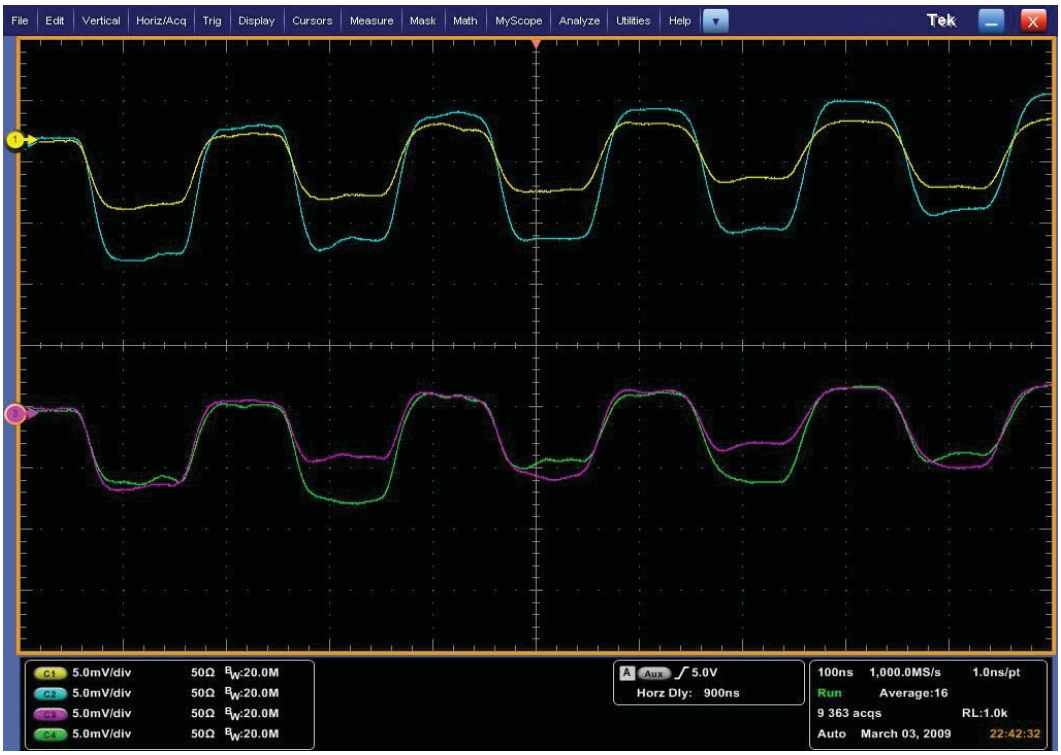

Figure 2.8: Screenshot of typical BPM signals on an oscilloscope. A discussion on how to process the BPM data appears in Appendix D.

this approach is not used often because it involves beam interception which will not work for multi-turn beam steering. Nevertheless, the phosphor screen is still used to enable assessing beam matching and control.

2.6.3 Wall Current Monitor

The wall current monitor is a device designed to measure the beam current without intercepting the beam [31]. The wall current monitor signal is proportional to the beam current. We use two quantities: the total current and the transmitted current rate to quantify the quality of the multi-turn operation. Larger first-turn total current implies better first-turn beam control. Larger transmitted current rate

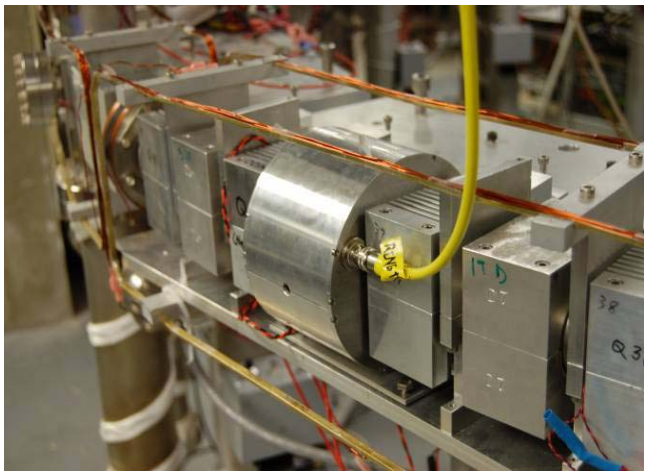

Figure 2.9: The wall current monitor for the University of Maryland Electron Ring.

as described in Chapter 3 implies less beam loss over multi-turn operation, and therefore better matching and steering.

Chapter 3

Resonance Analysis and Tune Investigation

Our goal in this chapter is to study the effect of space charge on the tune and map resonances as a function of the ring operating point. The operating tune and any resulting resonances have a decisive impact on multi-turn beam operation and beam quality. Our approach is to use the PIC code *WARP* to simulate electron beams at various conditions, and compare these results to other simulation codes and experiment. This helps us improve our system modeling and understand resonances in UMER. A series of experiments were carried out to test the simulation models and this improved our comprehension of simulation models.

The chapter is organized as follows. In the first section, we introduce the concept of accelerator tune and the stability criteria of an equilibrium orbit. An accelerator tune is defined as the number of betatron oscillations in one turn. In the second section, we introduce two approaches for computing the tune by experiment and simulation. In the third section we describe simulations and analyze the results. First, we evaluate different magnet models and compute the tune under those models. Then we introduce magnet errors to trigger resonances, which we map as a function of the operating point. Results from different magnet models and from different simulation codes are compared to understand the system. In the last section we repeat resonance analysis in experiment using wall current monitor

signals.

3.1 Introduction to Tune and Resonance

This section introduces the concepts of tune and resonance in a circular accelerator as discussed in [7, 32]. In a storage ring, the betatron tune is defined as the number of betatron oscillations (defined in Section 3.1.1) per revolution. Usually, the fractional part (the tune value minus its integer part) of the tune is more important because it determines the resonance behavior and hence the beam lifetime. At certain operating points, centroid oscillations due to machine errors are amplified and lead to beam loss. Furthermore, space charge in the beam can affect the beam dynamics and lead to a change of the tune value.

3.1.1 Accelerator Tune

In a circular accelerator, bending magnets are used to provide a complete revolution of the particle beams. For example, UMER has 36 horizontal ring bending dipoles. Each dipole is designed to bend the beam 10 degrees, and these bending dipoles define the closed orbit, which is the black circle shown in Figure 3.1. Particles displaced from the closed orbit performing oscillations around it are called betatron oscillations, whose frequency is determined by the quadrupoles. The definition of stability for a closed orbit is similar to the definition of asymptotical stability for an equilibrium point in control theory [30]: if a particle with a proper momentum for a given closed orbit has a small initial displacement and angular deviation from the

closed orbit, it will remain close to this orbit.

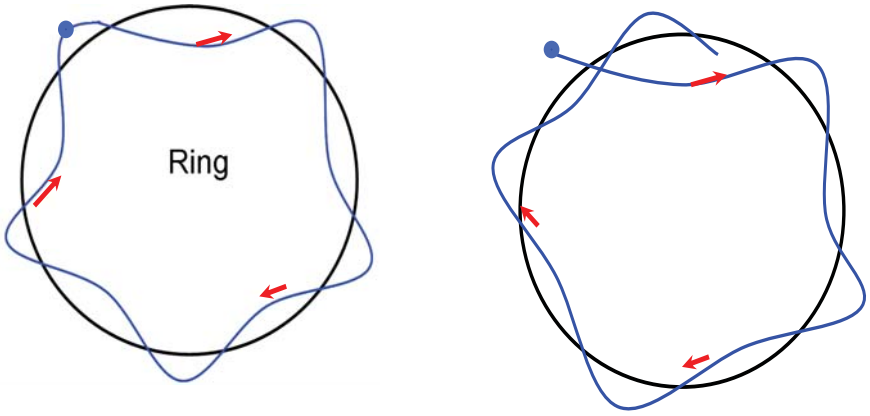

Figure 3.1: Schematic diagram of betatron oscillation, where the beam starts from the dot point and travels following the arrow direction. In the left figure, it has an integer tune and the beam returns to the starting point. In the right figure, it has a non-integer tune and it does return to the starting point in one turn.

If $x(s)$ and $y(s)$ are the displacements from the beam axis and s is the distance measure along the beam axis or the closed orbit in a circular machine, the transverse beam dynamics $x(s)$ and $y(s)$ are described by the following two equations

$$x''(s) + \kappa_x(s)x = 0 \tag{3.1}$$

$$y''(s) + \kappa_y(s)y = 0 \tag{3.2}$$

where κ_x and κ_y are the periodic-focusing functions, which satisfy the periodic condition $\kappa(s+L) = \kappa(s)$ and L is the length of the period. In a circular accelerator with circumference C and N focusing periods, we have the additional periodicity condition

$$\kappa(s + C) = \kappa(s)$$

where $C = N \times L$.

The second-order, linear differential equations with periodic coefficients are known as Hill's equations [7]. Their solutions take the form

$$X(s) = \begin{bmatrix} x(s) \\ \\ x'(s) \end{bmatrix} = M(s|s_0)X(s_0) = \begin{bmatrix} a & b \\ \\ c & d \end{bmatrix} \begin{bmatrix} x(s_0) \\ \\ x'(s_0) \end{bmatrix} \tag{3.3}$$

Note that the matrix M has the property

$$M(s + S|s_0) = M(s) \tag{3.4}$$

Thus the evolution of $x(s)$ and $x'(s)$ is determined only by the initial conditions $x(s_0), x'(s_0)$ and the matrix $M(s)$. To find the eigenvalues of the matrix M, consider the equation

$$Mz = \lambda z \tag{3.5}$$

where z are the eigenvectors and λ are the eigenvalues. The eigenvalues λ are obtained by solving the following equation

$$\begin{vmatrix} a - \lambda & b \\ \\ c & d - \lambda \end{vmatrix} = 0 \tag{3.6}$$

i.e.,

$$\lambda^2 - (a + d)\lambda + (ad - cb) = 0 \tag{3.7}$$

Note that $|ad - cb| = 1$ because $det|M| = 1$ [7, 32].

It is easy to see that the eigenvalues will be real if $|a + d| \leq 2$ and will be imaginary or complex if $|a + d| > 2$. In order for the system to be stable, we require $|a + d| < 2$.

Now we introduce a new parameter σ_0 as the following

$$cos\sigma_0 = \frac{1}{2}(a+d) = \frac{1}{2}\text{Trace(M)} \tag{3.8}$$

where σ_0 is called the *phase advance* or *phase shift* per period of the particle oscillation in one period. The units for σ_0 are degrees.

Furthermore, introduce the Courant-Snyder [7, 32] parameters $\hat{\alpha}, \hat{\beta}, \hat{\gamma}$ as follows:

$$2\hat{\alpha}sin\sigma_0 = a - d \tag{3.9}$$

$$\hat{\beta}sin\sigma_0 = b \tag{3.10}$$

$$\hat{\gamma}sin\sigma_0 = -c \tag{3.11}$$

Then the matrix M is expressed as

$$M = \begin{bmatrix} cos\sigma_0 + \hat{\alpha}sin\sigma_0 & \hat{\beta}sin\sigma_0 \\ -\hat{\gamma}sin\sigma_0 & cos\sigma_0 - \hat{\alpha}sin\sigma_0 \end{bmatrix} \tag{3.12}$$

$$= \begin{bmatrix} 1 & 0 \\ 0 & 1 \end{bmatrix} cos\sigma_0 + \begin{bmatrix} \hat{\alpha} & \hat{\beta} \\ -\hat{\gamma} & -\hat{\alpha} \end{bmatrix} sin\sigma_0 \tag{3.13}$$

$$= Icos\sigma_0 + Jsin\sigma_0 \tag{3.14}$$

where $\hat{\beta}$ is the *betatron function* and σ_0 is the phase advance per cell.

When the beam is transported by N periodic sections, we have

$$M^N = [(Icos\sigma_0 + Jsin\sigma_0)]^N$$

$$= Icos(N\sigma_0) + Jsin(N\sigma_0) \tag{3.15}$$

The *betatron tune* or *tune*, which is the number of betatron oscillations in one turn, is defined as

$$\nu_0 = N\frac{\sigma_0}{2\pi} = \frac{1}{2\pi}\int_{s_0}^{s_0+C}\frac{ds}{\hat{\beta}} \tag{3.16}$$

Note that σ_0, hence the tune ν_0, depends on the focusing strength κ which in turn depends on the focusing magnet settings.

3.1.2 Beam Resonance

In an ideal system where there is no dipole error, the particle beam perform radial betatron oscillations around the closed orbit. By using the smooth approximation method, we ignore the ripple in the oscillation amplitude and assume that the particle beam oscillation is sinusoidal [7, 33]. That is, it can be described by a differential equation as the following

$$\frac{d^2x}{d\theta^2} + k^2x = 0, \quad \text{where} \quad k^2 = \nu^2/R^2 \tag{3.17}$$

where ν is the tune, $\theta = s/R$ is the azimuth angle in the transverse direction, and R is the ring radius.

Assume there exists field error ΔB, then we have

$$\frac{d^2x}{d\theta^2} + \nu_0^2x = R\frac{\Delta B}{B} \tag{3.18}$$

i.e.,

$$\frac{d^2x}{d\theta^2} + \nu_0^2x = \delta cosn\theta \tag{3.19}$$

This has solution of the form

$$x = x_h + x_p \tag{3.20}$$

where

$$x_h = c_1 cos\nu_0\theta + c_2 sin\nu_0\theta \tag{3.21}$$

and

$$x_p = \frac{\delta}{\nu_0^2 - n^2} cosn\theta + c_3 cos\nu_0\theta + c_4 sin\nu_0\theta \tag{3.22}$$

When $\nu_0 = n =$ an integer, x_p blows up and the beam hits integer resonance.

Next, consider a quadrupole strength error $\Delta\kappa$.

$$\frac{d^2x}{d\theta^2} + \nu_0^2 x = R^2\Delta\kappa \tag{3.23}$$

which can be expressed as

$$\frac{d^2x}{d\theta^2} + (\nu_0^2 - \alpha cosn\theta)x = 0 \tag{3.24}$$

Equation (3.24) can be transformed into the equation

$$\frac{d^2x}{d\Phi^2} + (a - 2qcos2\Phi)x = 0 \tag{3.25}$$

The unstable betatron tune ν_0 is

$$\nu_0 = \frac{mn}{2} \tag{3.26}$$

In general, the condition above is equivalent to

$$m\nu_x + n\nu_y = p \tag{3.27}$$

where m, n and p are integers, ν_x is the tune in the x plane and ν_y is the tune in the y plane. When m or n takes a value of $\frac{1}{2}K$ with K odd, we say the beam is at half-integer resonance. In this chapter, we focus on the integer and half-integer resonances only.

3.1.3 Space Charge Tune Shift

Space charge forces in the beam cause a change of the tune value; this is called a tune shift. Depending on the type of tune shift, the tune shift is called "coherent" or "incoherent" tune shift. The defocusing effect of space charge on the betatron orbit of individual particle causes incoherent tune shift; the image forces between the accelerator pipe and the beam shifts the betatron orbit of the centroid and cause coherent tune shift.

We define the intensity parameter χ [7] as

$$\chi = \frac{1}{1 + \frac{2\beta\gamma I_0}{I}(\frac{\epsilon_n}{a})^2} = 1 - (\frac{\nu}{\nu_0})^2 \tag{3.28}$$

where I is the beam current, ϵ_n is the RMS normalized emittance, a is the RMS beam radius, and I_0 is the characteristic current ($I_0 = 17.0kA$ for electrons).

Thus the incoherent tune shift can be expressed as

$$\Delta\nu_{inc} = \nu_0(1 - \frac{\nu}{\nu_0}) = \nu_0(1 - \sqrt{1-\chi}) \tag{3.29}$$

where ν_0 is the zero-current tune, i.e., the tune based on the transfer matrix approach [7].

The coherent tune shift can be calculated from the ratio of the average beam radius a to the pipe radius b:

$$\Delta\nu_{coh} = \nu_0 - \nu_{coh} = \nu_0(1 - \sqrt{1 - (\frac{a}{b})^2}) \tag{3.30}$$

In Table 3.1, the incoherent and coherent tune shifts of three beams ranging from an emittance-dominated beam to space-charge-dominated beams are summarized.

Table 3.1: Coherent and incoherent tune shifts for the 83% operating point (calculated), where I is the beam current and a is the average beam radius (mm).

I (mA)	**a (mm)**	χ	$\Delta\nu_{inc}$	$\Delta\nu_{coh}$
0.7	2.0	0.40	1.12	0.02
7.0	5.3	0.82	2.88	0.11
23.0	7.8	0.93	3.70	0.25

3.2 Tune Calculation Techniques

As discussed earlier, precise knowledge of the betatron tune, especially the fractional part, is of crucial importance for both daily operations and theoretical investigations. In this section, we introduce two basic approaches for computing the tune from experimental and simulation data. The first approach is based on the Fast Fourier Transform. This approach requires beam circulation for a large number of turns with minimal beam loss to achieve acceptable resolution. The second approach is based on the beam position data. This approach is very sensitive to signal noise, the ring operation point and beam loss.

3.2.1 Fractional Tune Calculation Using FFT

The *Fast Fourier Transform* (FFT) is an efficient algorithm for computing the discrete Fourier transform and its inverse. The discrete Fourier transform is an interpolation method which is able to express a dataset as a combination of

sinusoidal functions with different coefficients. In this section, we describe how we can apply this method to compute the accelerator tune based on the measured beam position data.

A Fourier analysis of BPM measurement data up to N consecutive turns $(x_1, x_2, ..., x_N)$ proceeds as follows. First, we express these N data points as a Fourier series:

$$x(n) = \sum_{k=1}^{N} \phi(\nu_k) e^{i2\pi n\nu_k}, \quad \nu_k = \frac{k}{N} \tag{3.31}$$

Then, the frequency corresponding to the largest value of ϕ is taken as the tune. The error associated with this method is

$$|\delta\nu| < \frac{1}{N} \tag{3.32}$$

In order to achieve the desired precision of 0.01 in the tune, we need at least 100 turns without serious beam loss. This is difficult to achieve in UMER. We use the interpolated FFT method [34, 35] which can increase the computational resolution with the same number of turns.

In the interpolated FFT, we artificially insert extra points into the original data set, which improves the resolution of the conventional FFT. With this interpolation, a smaller turn number suffices to achieve a higher resolution in the tune.

Thus, we assume the unknown frequency ν_{interp} is close to the true tune and use the following form for $\phi(\nu_k)$ in Equation 3.31

$$\phi(\nu_k) = |\frac{sinN\pi(\nu_{interp} - \nu_k)}{Nsin\pi(\nu_{interp} - \nu_k)}| \tag{3.33}$$

where ν_{interp} is the unknown tune to be calculated.

The tune ν_{interp} can be expressed as the following

$$\nu_{interp} = \frac{k}{N} + \frac{1}{\pi} arctan(\frac{|\phi(\nu_m)| sin(\frac{\pi}{N})}{|\phi(\nu_k)| + |\phi(\nu_m)| cos(\frac{\pi}{N})}) \tag{3.34}$$

where $|\phi(\nu_k)|$ is the amplitude of the highest peak of the FFT spectrum and $|\phi(\nu_m)|$ is the amplitude of the second highest peak. The error is given by

$$|\delta\nu| < \frac{C_{Fint}}{N^2} \tag{3.35}$$

where C_{Fint} is a numerical constant.

Some other methods, for example windowing, help to increase the resolution of the interpolated FFT; these will not be discussed here. However, please see [29].

3.2.2 Tune Calculation Based on Four-Turn Beam Positions

In the FFT method above, we require the beam to transport for many turns without beam loss. However, that is a big challenge for fast cycling synchrotrons where the beam is not stored long enough, or for storage rings under commissioning. Therefore, we appeal to another approach for tune measurement, namely that used by Koutchouk [36]. This approach uses consecutive beam position monitor signals to calculate the fractional tune and equilibrium orbit.

Assume that the beam has small oscillations around an equilibrium orbit X. At turn n, without loss of generality, we can drop the dispersion and error terms in x_n [36], then the beam position x_n is

$$x_n = X + [cos(n\nu) + \hat{\alpha} sin(n\nu)]x_0 + \hat{\beta} x_0' sin(n\nu) \tag{3.36}$$

where $\hat{\alpha}$ and $\hat{\beta}$ are the Courant-Snyder parameters introduced in Section 3.1 and x_0

and x_0' are the unknown initial conditions. After some manipulation, the fractional tune ν and the equilibrium orbit are found to be given by

$$\nu = \frac{1}{2\pi} acos(\frac{x_n - x_{n+1} + x_{n+2} - x_{n+3}}{2(x_{n+1} - x_{n+2})}) \tag{3.37}$$

$$x_{co} = \frac{x_{n+1}^2 - x_{n+2}^2 + x_{n+1}x_{n+3} - x_{n+2}x_n}{3(x_{n+1} - x_{n+2}) + x_{n+3} - x_n} \tag{3.38}$$

respectively, where x_n, x_{n+1}, x_{n+2} and x_{n+3} are BPM readings for four consecutive turns at the same location.

By using this method, the computation can achieve enough resolution if the beam position data is reliable and the ring tune is not very close to an integer or half-integer value.

3.3 Tune and Resonance Analysis Based on Simulation

Simulation is a useful tool for understanding the system with the freedom to select various system modeling and configuration. In this section, we use several simulation codes to compute the tune, and to find out the best quadrupole model. Then we investigate how lattice errors and space charge affect the beam resonance.

3.3.1 Tune and Resonance Analysis Under Various Errors

The beam quality in a circular machine is affected by lattice errors, which are usually unknown. However, particle-in-cell simulation provides a powerful tool for checking how lattice errors affect the beam. At the same time, space charge plays an important role in beam dynamics. Simulation of beams for a set of currents helps us

understand the effect of space charge. Here, we first describe the simulation setup and then discuss the simulation results.

For the simulation code, we used the particle-in-cell code WARP [22], which was developed at Lawrence Livermore National Laboratory for heavy ion fusion applications. One important feature of WARP is its ability to deal with space-charge-dominated beams [37]. We have the following typical simulation setup:

1. An initial semi-Gaussian particle distribution, i.e, uniform in configuration space, Gaussian in velocity space and with a uniform temperature.

2. Use a constant earth field (0.4 Gauss).

3. Circulate the beam for 20 turns in the ring, ignoring the injection for the time being.

4. Use 100,000 particles on a 256×256 grid with a step size of 2 mm. These were tested to ensure numerical accuracy.

5. Set up various magnet errors or field errors.

In the simulations, two main cases concerning quadrupole settings are considered:

1. Random quadrupole alignment offsets to induce integer resonance.

2. Random quadrupole strength error to induce half-integer resonance.

Furthermore, we have tried various error amplitudes to test any amplitude

dependence and also tried various error distributions, particularly the Gaussian and uniform distributions.

3.3.2 Simulation Results and Analysis

In this section, we present our simulation and analysis results on resonance. Without loss of generality, we focus on horizontal tune only in all the discussions in this chapter. In the following simulation results, the maximum amplitude of the centroid is the maximum value over 20 turns; the maximum amplitude of the emittance is also the maximum value over 20 turns.

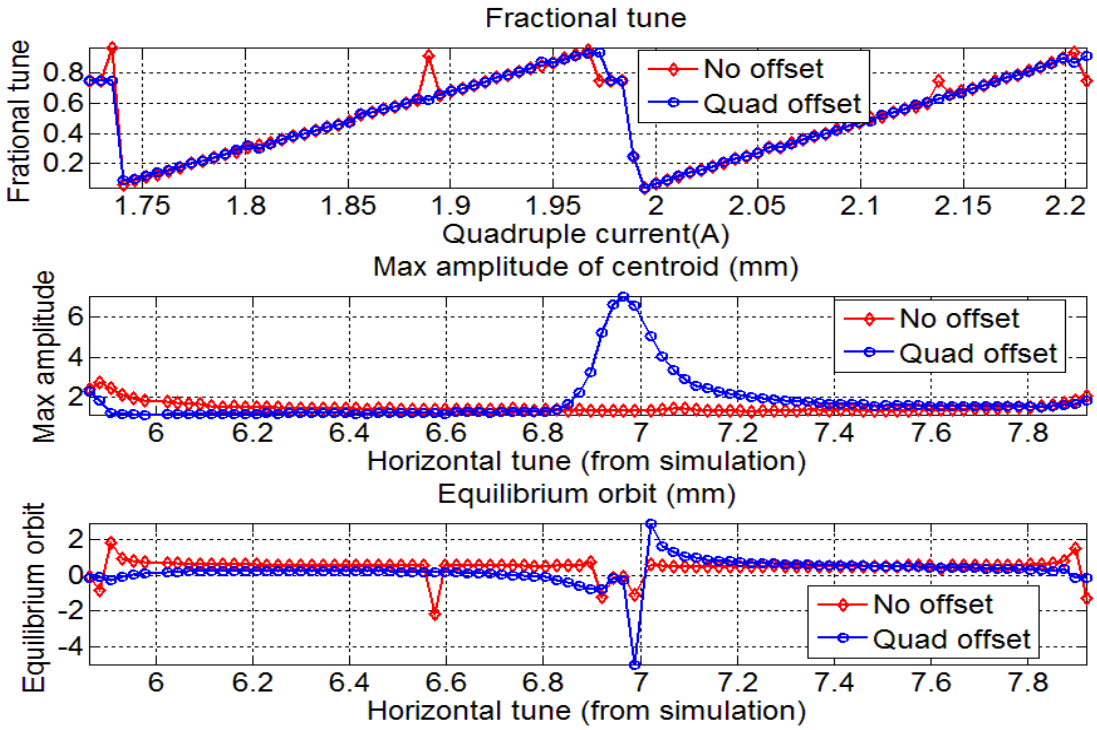

Figure 3.2: Simulation with and without random quadrupole alignment offset for the 0.7 mA beam. The red "diamond" line refers to the case without quadrupole offset. The blue "circle" line refers to the case with quadrupole offset.

In Figure 3.2, the top plot is of fractional tune versus quadrupole current. The middle plot is of maximum centroid amplitude versus calculated tune. The bottom plot is of equilibrium orbit versus calculated tune. It can be seen that the maximum amplitude of beam centroid will grow significantly around the integer tune point in the presence of random quadrupole misalignments. The equilibrium orbit is also distorted around the integer tune point. Without the errors, there is no centroid growth and no equilibrium orbit distortion.

In Figure 3.3, the top plot is the fractional tune and the bottom plot is the maximum centroid amplitude. It can be seen that the maximum amplitude of the beam centroid occurs for all three beams around the integer tune operating point. For the same errors, the amplitude for the 23 mA beam is twice as large as that for the 0.7 mA beam. On the other hand, the bandwidths of the resonance for these three different beams are almost the same. The tune shift agrees well with Table 3.1 for the three beams. The integer resonance for low current appears to be much stronger than for high current.

In Figure 3.4, the top plot depicts the fractional tune and the bottom plot depicts the maximum centroid amplitude. It can be seen that both the integer and the half-integer resonances appears upon introducing a random quadrupole strength error.

Next, we consider how the amplitude of the random error affects the beam. Three levels ($100\%, 150\%$ and 50%) of error amplitude are taken into consideration, where the 100% level corresponds to 0.2 mm. The maximum amplitude of the beam centroid and the maximum emittance are compared. In Figure 3.5, under the

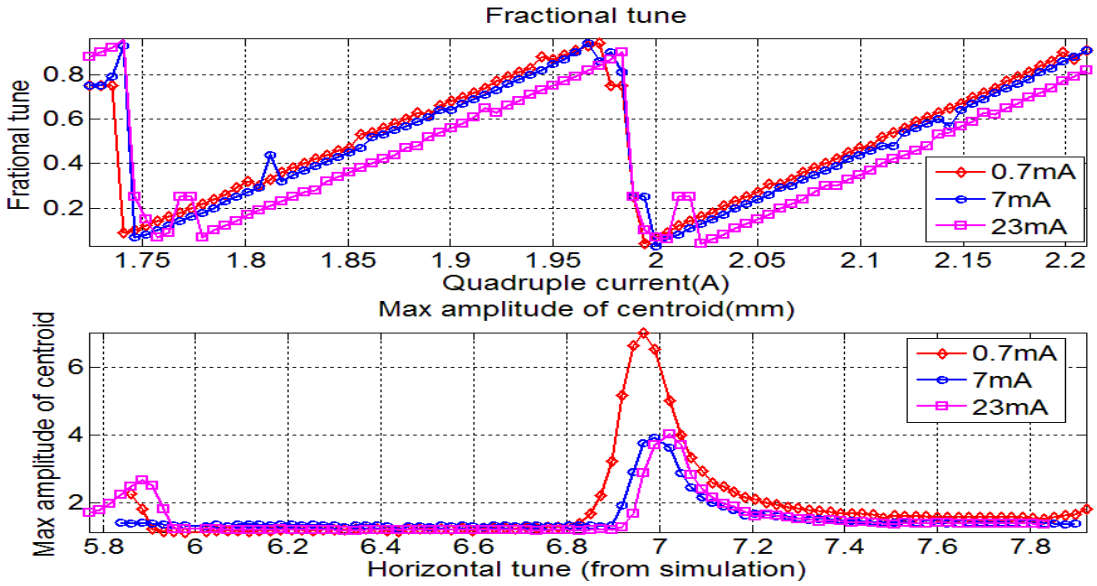

Figure 3.3: Simulation for the 0.7 mA, 7 mA and 23 mA beams with random quadrupole alignment error. The red "diamond" line refers to the 0.7 mA beam. The blue "circle" line refers to the 7mA beam. The purple "square" line refers to the 23 mA beam.

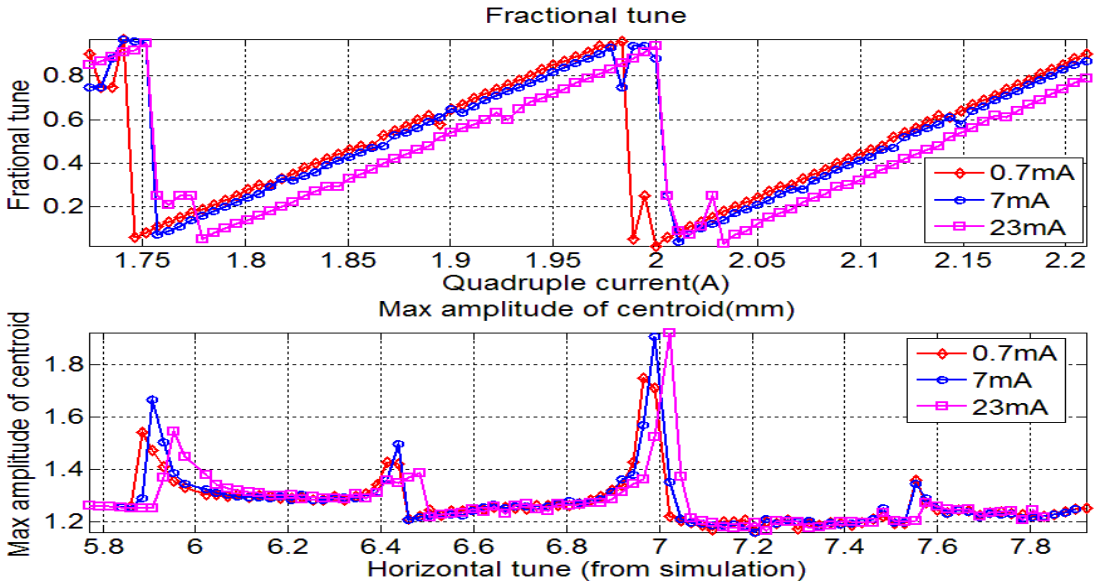

Figure 3.4: Simulation with quadrupole random strength errors for the 0.7 mA, 7 mA and 23 mA beams. The red "diamond" line refers to the 0.7 mA beam. The blue "circle" line refers to the 7mA beam. The purple "square" line refers to the 23 mA beam.

uniform error, the top plot is the maximum centroid and the bottom is the maximum emittance. It is clear from the plots that the larger amplitude of the noise, the larger are the centroid oscillations and beam emittance around the resonance points.

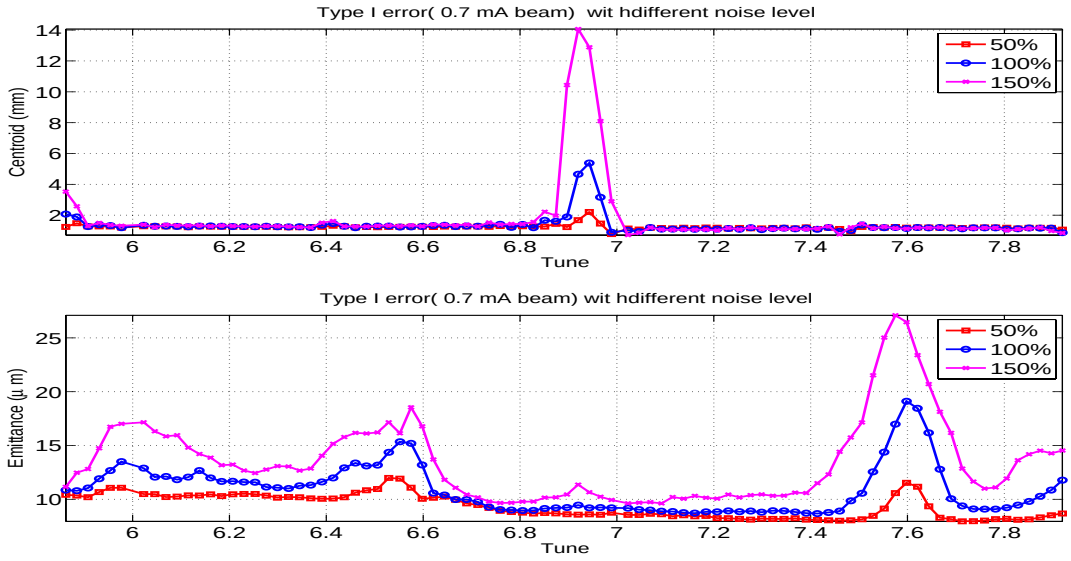

Figure 3.5: Simulation with quadrupole strength error of Gaussian-distribution for the 0.7 mA beam of three different amplitude levels.

Next, we explore how different types of noise affect beam resonance. Here, we consider both Gaussian noise and uniform noise. Both are selected with an amplitude of 0.2 mm. The simulation results are plotted in Figure 3.6 and Figure 3.7, respectively. These figures suggest that different types of noise may only affect the amplitudes of the maximum centroid and the maximum emittance.

3.3.3 Comparison of Models in Several Simulation Codes

Three particle simulation codes are used in our research group: WARP [22], WinAgile [23] and Elegant [26]. Each code has its own characteristics, and simula-

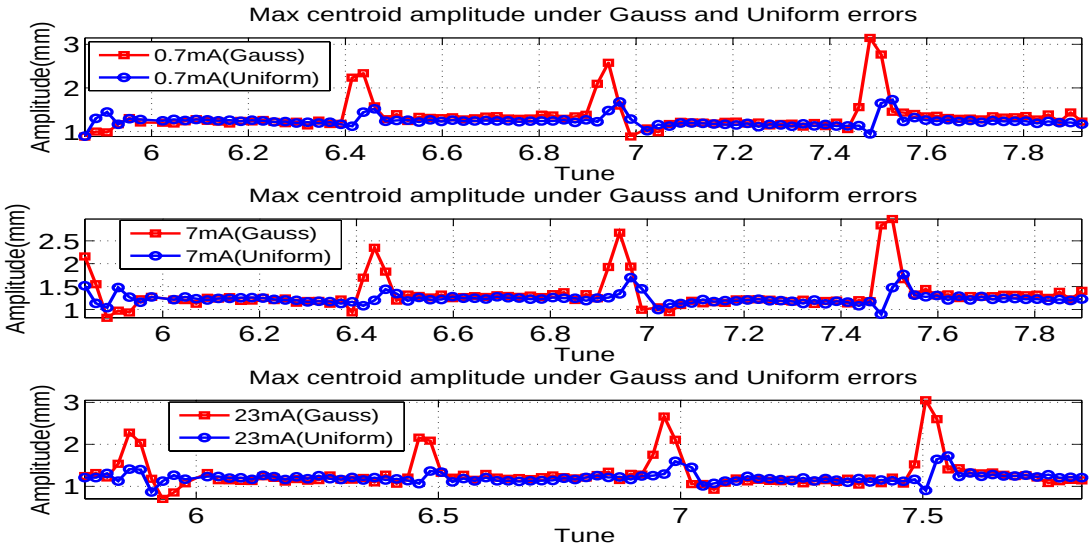

Figure 3.6: Simulation: Comparison of maximum centroid under different types (Gaussian and uniform) of quadrupole strength error for the 0.7 mA, 7 mA and 23 mA beams.

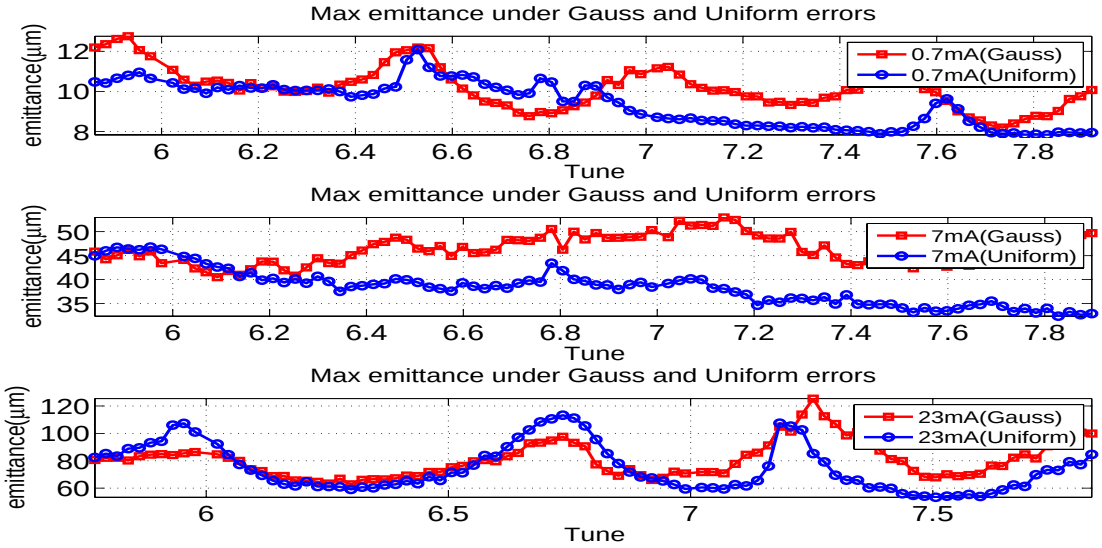

Figure 3.7: Simulation: Comparison of maximum emittance under different types (Gaussian and uniform) of quadrupole strength error for the 0.7 mA, 7 mA and 23 mA beams.

tion results based on each code are compared to crosscheck how good the modeling is. WARP can deal with various magnet models and space charge forces. WinAgile is a linear matrix code. Elegant is a particle-tracking code which does not include space charge. In this study, we choose to use WARP code and compare the obtained results with other codes.

First, we conducted a comprehensive study in WARP to compute the effect of different magnet models on tune. The results are shown in Table 3.2. The study shows evidence that the tune calculated with the magnet's nonlinearities is closer to the tune obtained from experiment. The bending dipoles contribute to a tune shift as well. These results were later crosschecked by experiment. In these simulations, we used the regular quadrupoles to substitute for the two complex magnets YQ and QR_1, which accounted for some discrepancy. The results in Table 3.2 give us confidence that these modeling approaches provide an accurate mean for modeling UMER quadrupole.

In Table 3.2, in the full quadrupole model, the quadrupole is modeled as "bgrd" [50] with nonlinear fringe field, and the fringe field is modeled as a nonlinear fringe field; in the ideal hard-edge model, the quadrupole is treated as hard-edge quadrupole. Detailed descriptions can be found in the technical report [46].

It is helpful to compare the tune calculation from different codes. As discussed earlier, whereas different methods for measuring tune should agree with one another, we have noted a discrepancy in the measured value of tune and the value calculated from different simulation codes and different quadrupole models. This discrepancy can be as much as 0.4 for the 7 mA as shown in Table 3.3. Understanding the source

Table 3.2: Tune values from WARP simulations for a 10 keV, 7 mA beam at the 83% operating point for different magnet models.

WARP Simulation	**Tune Value**
Full quadrupole model	6.51
Full quad model with Bz = 0	6.48
Full quad model with no dipoles	6.39
Quads with linear fringe fields	6.21
Ideal hard-edge quads	6.18

Table 3.3: Calculated and measured horizontal tunes for the 7 mA beam at the 83% operating point by different methods.

Measurement	**Tune Value**
4-Turn data	6.60
FFT	6.53
Fit to BPM data	6.57
Calculation	**Tune Value**
Matrix (hard-edge quads, no images)	6.17
WinAgile (hard-edge quads, no images)	6.13
ELEGANT (hard-edge quads, no images)	6.24
WARP (full quad model, images)	6.51

of the discrepancy is important for us in order to improve our lattice and magnet models in the simulation codes. Note that this difference is larger than the coherent tune shift (0.11) for the 7 mA beam as shown in Table 3.1.

3.4 Experimental Analysis of Tune and Resonance

As noted in Chapter 2, the wall current monitor is a device designed to measure the beam current without intercepting the beam [31]. The signal from the wall current monitor is proportional to the beam current. Thus when there is beam loss, the corresponding wall current monitor signals also decreases. In this section, we explore how the space charge affects the resonance by computing signals from the wall current monitor as influenced by changing quadrupole currents. Then, we check how the beam pulse length affects the resonance. In this study, in order to have sufficient precision, we collected data for up to 20 turns.

First, we define a parameter r_n which is intended to quantify beam loss in the ring. Without loss of generality, we use the signals from the wall current monitor in the definition:

$$r_n = \frac{\text{total current at turn } n}{\text{total current at turn 1}} = \frac{I_n}{I_1} \tag{3.39}$$

where, in general, the wall current monitor's location does not influence the result. The quantity r_n defines the beam loss, or the transmitted current. A larger r_n indicates a better quality of multi-turn operation. In the following experiment, we choose for our study the wall current monitor at RC 10.

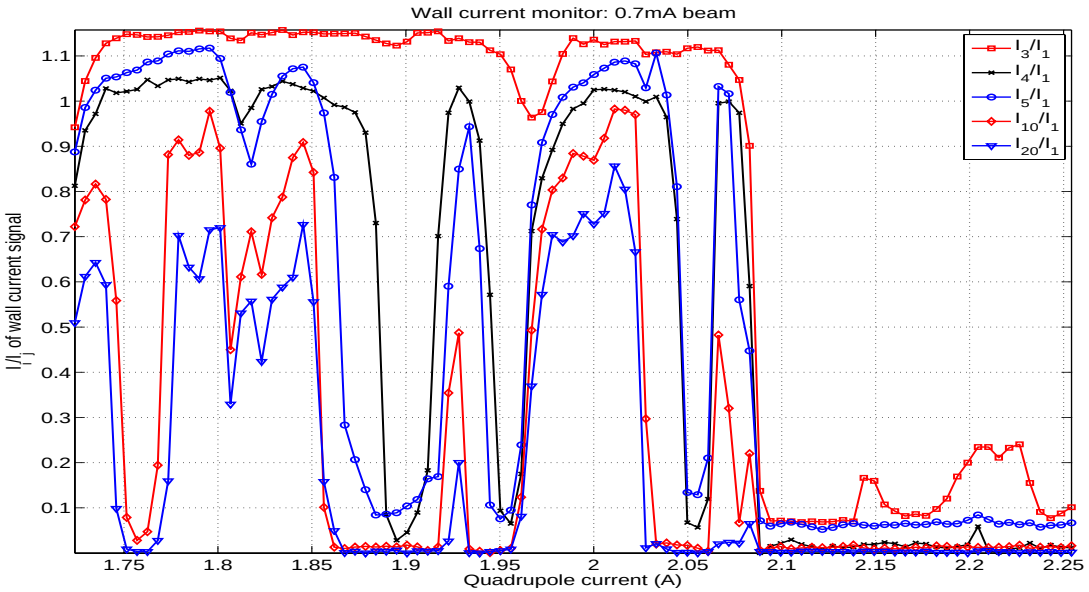

Figure 3.8: Experimental result of the transmitted current using wall current monitor signal: quadrupole current (horizontal axis) versus transmitted current (vertical axis) for the 0.7 mA beam.

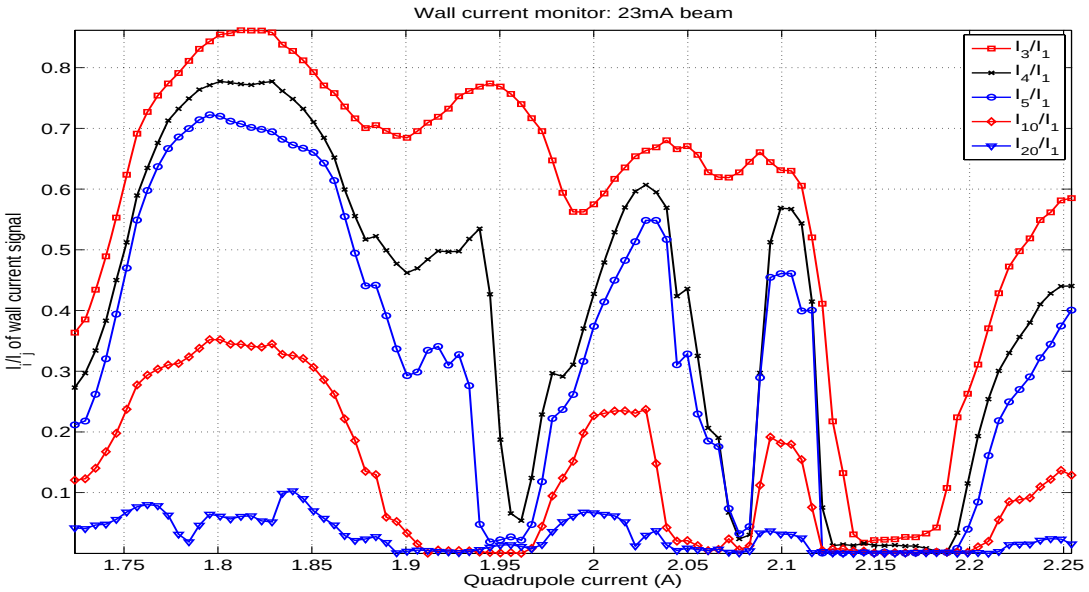

Figure 3.9: Experimental result of the transmitted current using the wall current monitor signal: quadrupole current (horizontal axis) versus transmitted current (vertical axis) for the 23 mA beam.

3.4.1 Effect of Space Charge

As discussed earlier, the space charge forces affect accelerator tune and resonance. We scanned two beams: the 0.7 mA beam and the 23 mA beam for a wide range of ring quadrupole currents. The experimental results are shown in Figure 3.8 and Figure 3.9. Comparing these two figures, we see that the space charge forces do affect the resonance in the experiment. The resonance point is shifted when scanning the quadrupole current for different beams.

Figure 3.10 gives the results of an experiment for two beams with different degrees of space charge. The 7 mA beam has low space charge and the 23 mA beam has intense space charge. The top plot is for the 7 mA beam, where we can see a large beam loss in three regions. The first region is 1.85-1.95 A which is the widest region. The second region is 2.03-2.07 A. The third region is around 2.17 A with only a drop of r_4. The bottom plot is for the 23 mA beam, where we see a significant beam loss in three regions. However, in this case there is a shift in the region of beam loss and the width of the region differs from that of the 7 mA beam. The first region is the range 1.94-1.96 A; the second region is the range 2.06-2.08 A; the third region is the range 2.12-2.2 A.

3.4.2 Effect of Longitudinal Pulse Length

As the beam circulates in the accelerator pipe, space charge forces push the beam head forward and the beam tail backward. After some time, the flat-top beam current will erode as more particles get trapped in the head and tail, which

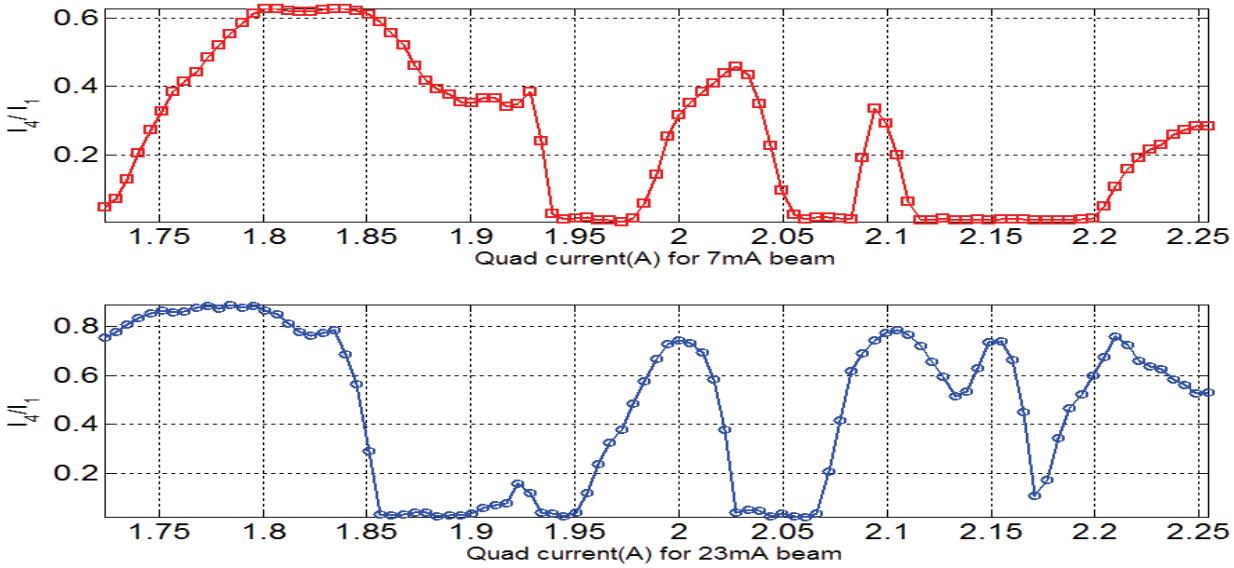

Figure 3.10: Comparison of experimental results of the transmitted current using wall current monitor signals for the 7 mA and 23 mA beams: quadrupole current (horizontal axis) versus transmitted current (vertical axis).

will shift beam resonance. In this subsection, we use the wall current monitor signal to investigate how beam resonance is affected by the pulse length.

We usually operate the machine with a beam of 100 ns pulse length. With current UMER settings, we can choose several other pulse lengths: 66 ns, 50 ns, and 25 ns. The experimental results for all these are plotted in Figure 3.11 and Figure 3.12. It is clear from both figures that the pulse length does not affect the point where resonance occurs, but does affect multi-turn beam decay speed.

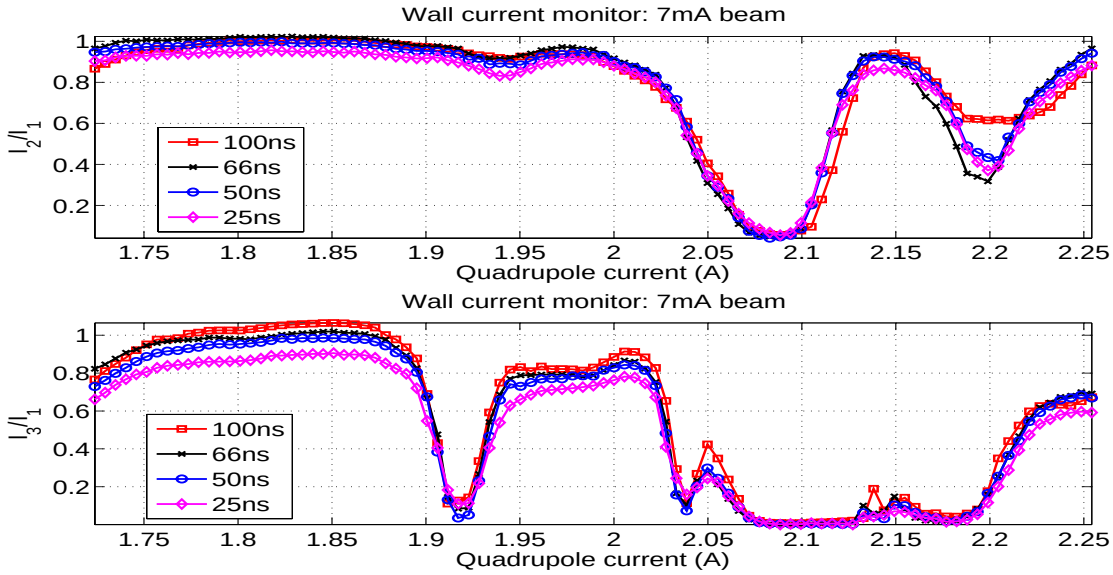

Figure 3.11: Experimental results of the transmitted current r_2, r_3 using wall current monitor signals for the 7 mA beam with different pulse length.

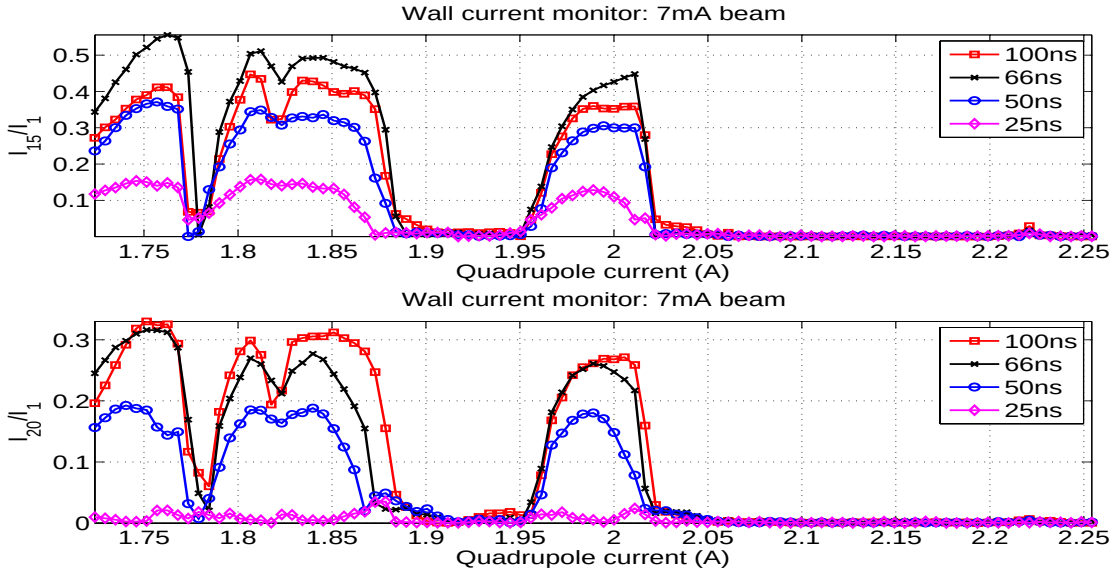

Figure 3.12: Experimental results of the transmitted current r_{15}, r_{20} using wall current monitor signal for the 7 mA beam with different pulse length.

Chapter 4

System Diagnosis with the Orbit Response Matrix

In this chapter, we introduce a new method of system diagnosis for UMER. UMER is a large and complex system with more than 72 quadrupoles, 35 horizontal dipoles and 18 vertical dipoles, 15 BPMs and many other elements. It is difficult to check by direct measurement whether any single element (dipole, quadrupole, BPM, etc) in the ring is working properly. The goal of this chapter is to introduce a method for diagnosing the system and finding faulty elements in the ring so that they can be repaired. We have successfully developed such a method using the orbit response matrix. Because the accelerator is constructed to be periodic from chamber to chamber, corresponding elements in the response matrix should be identical or so. If there is a problem with the quadrupoles, dipoles or BPMs, the periodicity will be broken, which will in turn be reflected in the response matrix. Using the developed technique, we have successfully detected errors in BPMs and dipoles on UMER. Previously, we have no systematic diagnosis method for locating sources of problems at UMER. We believe this approach can benefit others who are dealing with systems having periodicity in their structure.

The chapter is organized as follows. In the first section, we introduce the orbit response matrix. In the second section, we calculate certain elements of the response matrix by simulation and through transfer matrix computation. These results yield

predictions for the experimental results in the third section. In the third section, we present detailed procedures for experimental diagnosis of UMER. We have used these procedures to successfully identify several magnet and BPM errors in the ring in only three steps. In the last section, we show that there is a coupling effect between the horizontal and vertical kickers in the injector using the orbit response matrix.

4.1 Orbit Response Matrix

For simplicity, initially, we assume there is no coupling between the horizontal dipoles and vertical dipoles. The response matrix R is then defined as follows:

$$R_{ij} = \frac{\text{beam position change } \Delta x \text{ at BPM } j}{\text{current change } \Delta I \text{ at dipole } i} \tag{4.1}$$

The dimension of R is determined by the number of BPMs and the number of dipoles. If we choose the horizontal dipoles D_1, D_2, D_3, D_4, D_5 as shown in Figure 4.1, we consider the beam position change in the horizontal plane. If we choose the vertical dipoles RSV_1, RSV_2, RSV_3 as shown in Figure 4.1, we consider the beam position change in the vertical plane. In some cases, we should consider beam position changes in both planes if there is a coupling between the horizontal dipoles and the vertical dipoles, such as in the injection of UMER. This will be demonstrated in the last section of this chapter.

The response matrix approach has been widely used in system diagnosis [38, 39] and beam centroid control [16, 17]. Nishimura and Walter [40] gave some preliminary results on response matrix analysis for UMER. However, their results were not

complete and not used for system diagnosis at that time. In this chapter, we will present comprehensive results and analysis using the orbit response matrix.

4.2 System Diagnosis with Simulation and Theory

In this section, we present a system diagnosis method based on simulation and theoretical analysis. With this method, we were able to diagnose the BPMs and magnets in UMER. As mentioned earlier, the ring is designed to have identical sections (ring chamber). Referring to the schematic diagram of UMER in Figure 2.1 in Chapter 2, we now focus on only a part of the ring as illustrated in Figure 4.1.

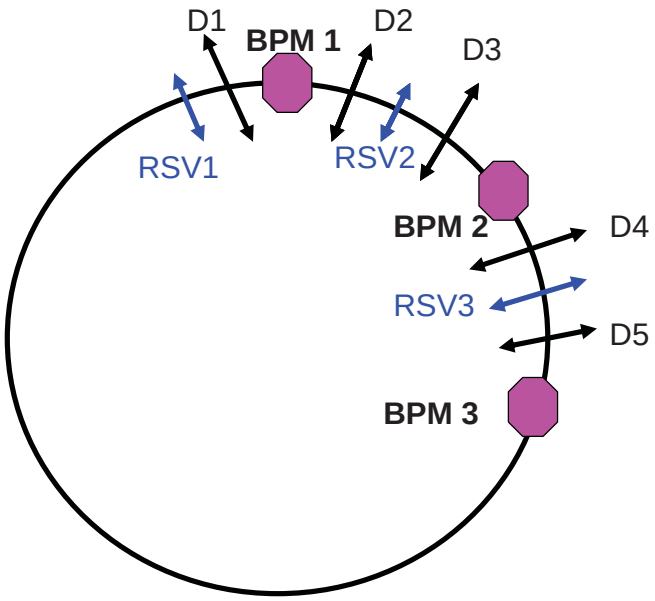

Figure 4.1: Schematic of part of UMER. D_i $(i = 1, 2, ..., 5)$ are the horizontal dipoles. RSV_i $(i = 1, 2, 3)$ are the vertical dipoles. Not to scale.

As shown in Figure 4.1, there is a horizontal beam position change (ΔX_1) in BPM 1 due to a current change ΔI_1 in dipole D_1 without any other changes

elsewhere. Similarly a change in current ΔI_2 in dipole D_3 resulted in a horizontal beam position change (ΔX_2) in BPM 2. If the ring chamber satisfies the periodicity condition as designed, the following identity should hold:

$$\zeta_1 = \frac{\Delta X_1}{\Delta I_1} = \frac{\Delta X_2}{\Delta I_2} \tag{4.2}$$

For vertical kickers, we consider the resulting vertical beam position change in the vertical plane. There is a vertical beam position change (ΔY_1) in BPM 1 due to a current change ΔI_1 in the vertical dipole RSV_1 with no changes applied elsewhere. Similarly a change in current ΔI_2 in vertical dipole RSV_2 resulted in a vertical beam position change (ΔY_2) in BPM 2. We expect the following to hold:

$$\zeta_2 = \frac{\Delta Y_1}{\Delta I_1} = \frac{\Delta Y_2}{\Delta I_2} \tag{4.3}$$

For UMER, we have selected several groups of pairs of interest as shown in Table 4.1. For each group in the table, the equations of (4.2) or (4.3) should hold. In the following, we focus only on the first two groups and they will help us identify two basic identities (4.2) and (4.3) as above.

For the horizontal pair, a schematic diagram is shown in Figure 4.2. Using the transfer function approach for the structure depicted in Figure 4.2, we have

$$M = M_{drift} \times M_{quad} \times M_{drift} \times M_{dipo} \tag{4.4}$$

such that

$$\zeta_1 = -6.89(mm/A) \tag{4.5}$$

A schematic diagram for the vertical pair is given in Figure 4.3. Using the

Table 4.1: Pairs of interest.

Group 1	Group 2	Group 3
(D1, BPM 1)	(RSV1, BPM 1)	(D2,BPM2)
(D3, BPM 2)	(RSV2, BPM 2)	(D4,BPM3)
(D5, BPM 3)	(RSV3, BPM 3)	(D8, BPM 5)
(D9, BPM 5)	(RSV5, BPM 5)	(D10, BPM 6)
(D11, BPM 6)	(RSV6, BPM 6)	(D12, BPM 7)
(D13, BPM 7)	(RSV7, BPM 7)	(D14, BPM 8)
(D15, BPM 8)	(RSV8, BPM 8)	(D16, BPM 9)
(D17, BPM 9)	(RSV9, BPM 9)	(D20, BPM 11)
(D21, BPM 11)	(RSV11, BPM 11)	(D22, BPM 12)
(D23, BPM 12)	(RSV12, BPM 12)	(D24, BPM 13)
(D25, BPM 13)	(RSV13, BPM 13)	(D26, BPM 14)
(D27, BPM 14)	(RSV14, BPM 14)	(D28, BPM 15)
(D29, BPM 15)	(RSV15, BPM 15)	(D32, BPM 17)
(D33, BPM 17)	(RSV17, BPM 17)	

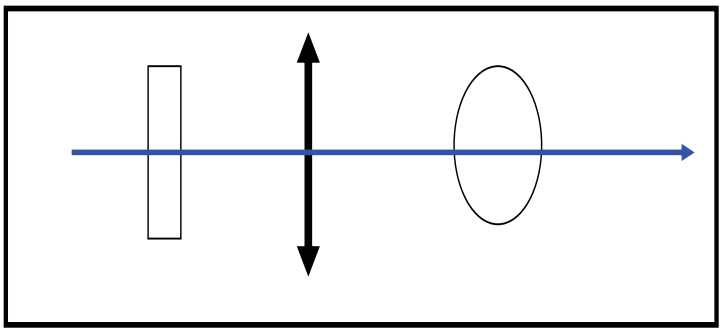

Figure 4.2: The horizontal pair. Along the sequence from left to right are the horizontal dipole, focusing quadrupole, and BPM.

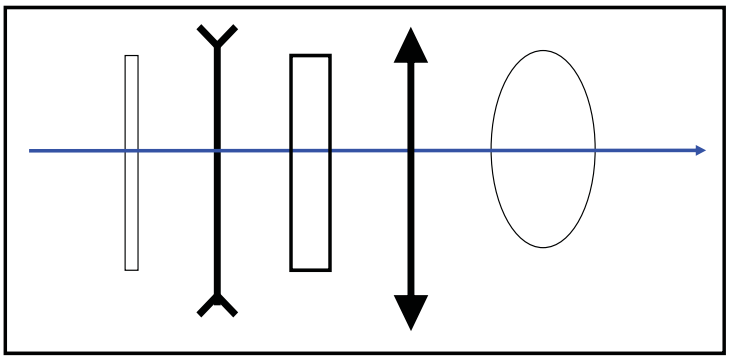

Figure 4.3: The vertical pair. Along the sequence from left to right are the vertical dipole, defocusing quadrupole, horizontal dipole, focusing quadrupole and BPM.

transfer function approach for the optics shown in Figure 4.3, we have

$$\begin{aligned} M &= M_{drift} \times M_{focu} \times M_{drift} \times M_{horizontal} \times M_{drift} \times M_{defocus} \\ &\quad \times M_{drift} \times M_{vertical} \end{aligned} \tag{4.6}$$

such that

$$\zeta_2 = -3.23(mm/A) \tag{4.7}$$

At the same time, we use simulation results from WARP (see the simulation

Table 4.2: Calibration factors of ζ_1 and ζ_2 from simulation and transfer matrix.

	Without earth field	With earth field	Transfer matrix approach
ζ_1	-6.68	-6.83	-6.89
ζ_2	-3.25	-3.26	-3.23

configuration in Figure 4.4) to calculate the same calibrated parameters, both with and without the earth field.

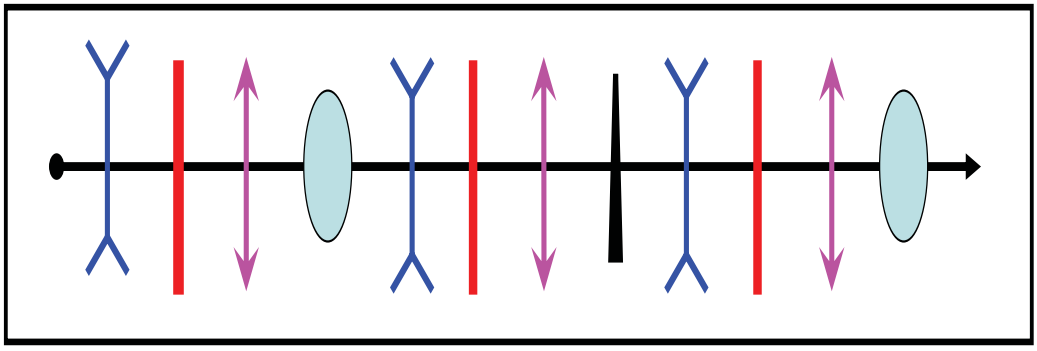

Figure 4.4: Magnets in WARP simulation configuration.

The results are shown in Table 4.2. Comparing the results from the transfer function approach and simulation with or without earth field, there is less than a 1% difference between these values. This implies: 1) The earth field does not make a large difference; and 2) The simulation model provides a model close to the analytical model.

4.3 System Diagnosis Through Experiment

In this section, we first provide a brief introduction of how the ring's periodicity is tested. Then we introduce a systematic diagnosis for UMER based on the orbit response matrix.

4.3.1 Basic Check of Periodicity

For simplicity, we first began with a basic check of periodicity by considering the first several dipoles and BPMs as shown in Figure 4.1.

Tables 4.3 and 4.4 contain the experimental data for the 80 mA beam and 7 mA beam, respectively. In these two tables, when there was a current change ΔI at dipole D_1, the corresponding beam position change ΔX was measured at all BPMs. The quantity $\zeta_1 = \frac{\Delta X}{\Delta I}$ was computed and shown in the tables. As we can see for both the 7mA beam and 80 mA beam, the quantity of ζ_1 was more close to each other at BPM 1 (in red color). At other BPMs (BPM 2,3,...,17), which are away from dipole D_1, the quantity of ζ_1 does not agree with each other and has bigger spread when Δ_I is different. That is the reason in later sections, we only consider the beam position change in the nearest downstream BPM.

Table 4.3: Analysis of experimental measurement of ζ_1 under different dipole currents on $D1$, with horizontal beam position change for the 80 mA beam. The quadrupoles were set at the 83% operating point. "x" means no measurement at that location.

ΔI	1	2	3	4	5	6	7	8	9	10	11	12	13	14	15	16	17
-0.4	-5.0	-10.6	13.3	x	-10.9	16.6	-5.6	-9.5	16.0	x	-9.5	12.0	-5.7	9.3	0.1	x	0.1
-0.2	-5.3	-10.7	16.2	x	-11.3	18.0	-6.5	-10.8	18.5	x	-11.1	14.2	-4.2	11.9	4.7	x	4.7
0.2	-5.7	-10.4	17.6	x	-11.3	15.5	-6.4	-10.5	15.7	x	-11.5	16.3	-4.7	11.3	8.5	x	8.5
0.4	-5.7	-10.3	17.5	x	-9.9	9.6	-6.2	-9.2	13.4	x	-9.3	14.2	-4.7	8.8	8.1	x	8.2
mean	-5.4	-10.5	16.2	x	-10.8	14.9	-6.2	-10.0	16.0	x	-10.3	14.2	-4.8	10.3	5.3	x	5.3

Table 4.4: Analysis of experimental measurement of ζ_1 under different dipole currents on $D1$, with horizontal beam position change for the 7 mA beam. The quadrupoles were set the 83% operating point. "x" means no measurement at that location.

ΔI	1	2	3	4	5	6	7	8	9	10	11	12	13	14	15	16	17
-0.4	-6.5	-8.3	15.4	x	1.2	11.5	-16.0	8.9	4.2	x	14.4	-1.9	-12.4	-16.4	-5.0	x	-5.0
-0.2	-6.7	-8.8	16.3	x	0.5	12.6	-16.6	8.0	5.8	x	14.0	0.3	-14.1	-16.5	-4.0	x	-4.0
0.2	-5.4	-7.9	16.4	x	-1.6	13.3	-14.7	5.6	8.4	x	11.8	3.1	-14.9	-16.1	-2.3	x	-2.3
0.4	-4.9	-6.1	13.0	x	-0.5	10.3	-12.0	4.7	6.7	x	9.6	2.4	-12.3	-13.8	-2.2	x	-2.2
mean	-5.9	-7.8	15.3	x	-0.1	11.9	-14.8	6.8	6.3	x	12.5	0.9	-13.4	-15.7	-3.4	x	-3.4

Table 4.5: Analysis of experimental measurement of ζ_1 between the 80 mA and 7 mA beams. The quadrupoles were set at 83% operating point. "x" means no measurement at that location.

$\frac{\Delta X}{\Delta I}$	1	2	3	4	5	6	7	8	9	10	11	12	13	14	15	16	17
80 mA	-5.4	-10.5	16.2	x	-10.8	14.9	-6.2	-10	15.9	x	-10.3	14.2	-4.8	10.3	5.3	x	5.3
7 mA	-5.9	-7.8	15.3	x	-0.1	11.9	-14.8	6.8	6.3	x	12.5	0.9	-13.4	-15.7	-3.4	x	-3.4

Table 4.6: Analysis of experimental measurement of ζ_1 between the 80 mA and 7 mA beams with horizontal beam position change. The quadrupoles were set at 83% operating point. "x" means no measurement at that location.

$\frac{\Delta X}{\Delta I}$	1	2	3	4	5	6	7	8	9	10	11	12	13	14	15	16	17
80 mA	0	-5.8	-8.5	x	-7.4	-6.6	14.3	-8.3	-7.2	x	-7.8	-7.4	12.7	6.9	-1.7	x	-1.7
7 mA	0	-5.5	-6.6	x	-13.7	1.8	11.1	-15.9	9.4	x	-16.1	13.9	-1.3	12.6	7.7	x	7.7

As we can see, from Tables 4.5 and 4.6, ζ_1 has an error of less that 10% both for the 80 mA beam and the 7 mA beam. Comparing the second column in Table 4.5 and the third column in Table 4.6, both in red color, the error in ζ_1 is less than 7%. These errors are acceptable for UMER. The results mean that dipoles D_1, and D_3 and BPMs 1 and 2 are working properly.

To aid in visualization of the response matrix, we plot the diagonal elements of the experimental response matrix. Because of the periodicity of the ring, there is no need to consider all the elements in the orbit response matrix. We only consider those elements which can lead to a direct corrector-BPM relationship, i.e., the diagonal elements. We only consider the second column in Table 4.5 and the third column in Table 4.6. In the following, we will present graphical results to illustrate how the response matrix can help in diagnosis of the system. Moreover, in order to verify the experimental results, we compare the results for the values of ζ_1 and ζ_2 with the results from the simulation and from the transfer matrix approach.

4.3.2 Systematic Diagnosis of UMER

We then extended the experimental computation to the whole ring. The experimental procedures are as follows:

1. Measure the initial beam positions under the current best steering solution;

2. Measure the beam positions in all BPMs, while changing the current in dipole D_1 by ΔI;

3. Set the current of dipole D_1 to its original current;

4. Go to the next horizontal/vertical dipole listed in Table 4.1 and repeat Step 2 and Step 3, until the last dipole listed in the corresponding group in Table 4.1.

Note that $\Delta I = [-0.25A, -0.15A, 0.15A, 0.25A]$ for the horizontal pairs and $\Delta I = [-1.0A, -0.50A, 0.50A, 1.0A]$ for the vertical pairs. We selected the changes in current them in a symmetrical way such that we can check the symmetry of beam position change from the closed orbit due to perturbation. Moreover, the current change should be small to ensure there is a linear response of the closed orbit; and the current change should be large to ensure the UMER beam possesses enough sensitivity of beam position change. For the vertical kickers, we applied larger values for Δ_I because vertical kickers have weaker strength. In the following experiments in this chapter, the ring was operated using the standard configuration file for the 7 mA beam which is summarized in the Appendices.

In the ideal case, all ζ_1 should be equal; all ζ_2 should be also equal, and so on. Therefore, we plot these values in Figures 4.5 and 4.7 to compare the results for different dipole current changes.

In our initial measurement of the response matrix, a problem appeared to occur at pair (D_{27}, BPM_{14}) as shown in Figure 4.5 in the horizontal plane. From

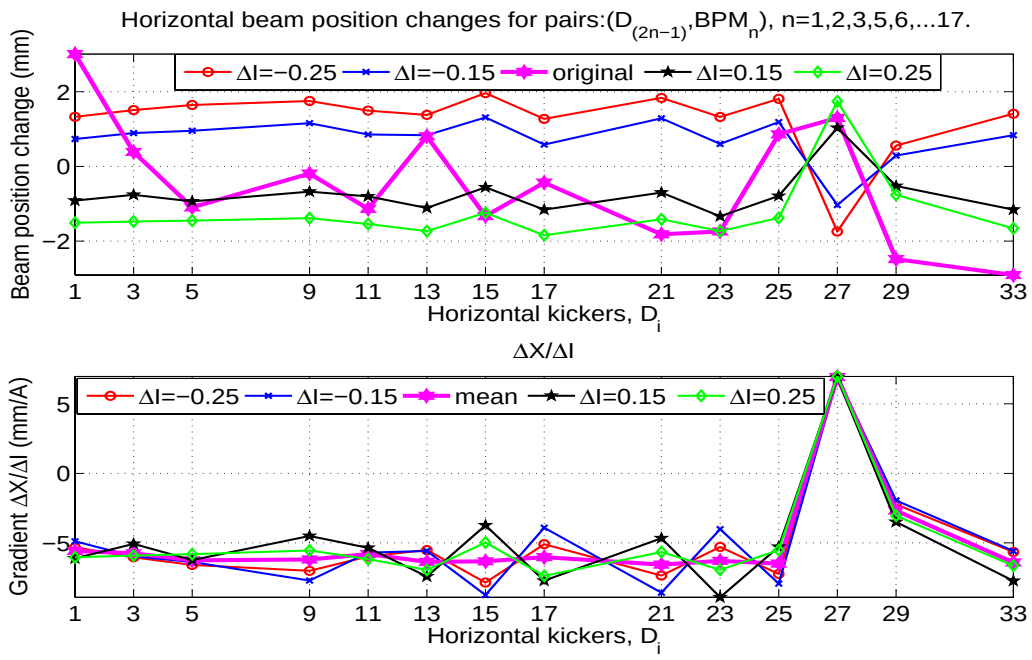

Figure 4.5: Diagnosis step 1.1. The horizontal axis is horizontal dipole number and the vertical axis is horizontal beam position change (in the top plot) or $\zeta_1 = \frac{\Delta X}{\Delta I}$ (in the bottom plot).

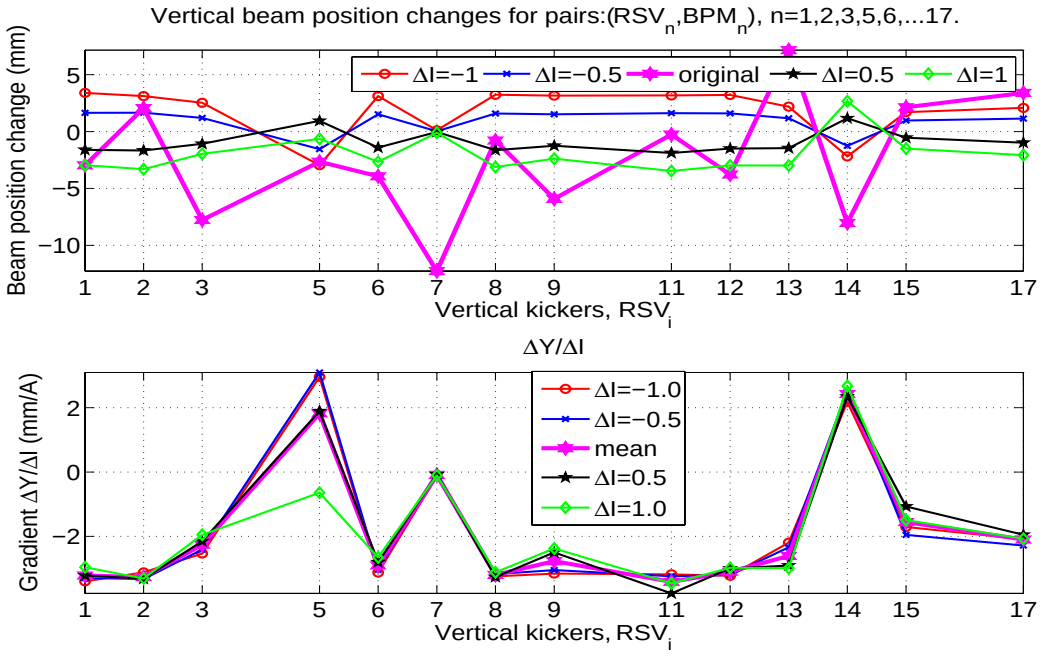

Figure 4.6: Diagnosis step 1.2. The horizontal axis is vertical dipole number and the vertical axis is vertical beam position change (in the top plot) or $\zeta_1 = \frac{\Delta Y}{\Delta I}$ (in the bottom plot).

Figure 4.6, we can see there was a problem at (RSV_5, BPM_5) and (RSV_{14}, BPM_{14}) in the vertical plane.

With respect to BPM 14, the sign of ζ_1 and ζ_2 (positive) is different from the sign of other values at other BPMs (negative). This led us to suspect that the cables in BPM 14 were connected to the wrong plates. We then exchanged the T (top)-B (bottom) and L (left)-R (right) cables of BPM 14. For the problem at BPM 5, we suspected that the vertical kicker RSV 5 was rotated. Upon checking, we found the magnet RSV_5 was loosely connected with its power line and it was also slightly rotated. We fixed this magnet.

After these operations, we took another set of measurements; the results were presented in Figures 4.7 and 4.8. The problems exhibited at BPM 14 disappeared. However, a new problem emerged as there were problems at pairs (D_{29}, BPM_{15}) and (RSV_{15}, BPM_{15}). The amplitudes of ζ_1 (horizontal) and ζ_2 (vertical) were only half of others in their corresponding groups.

We suspected there was another problem with the BPM cables. After inspecting BPM 15 again, we found out that the cable connections had been cross-wired. The T cable and R cable were interchanged. We re-connected these two cables and repeated the measurement. The results are shown in Figures 4.9 and 4.10. The problems with BPM 15 disappeared and the spreads of ζ_1 and ζ_2 became much smaller. The only remaining problem showed at vertical pair (RSV_7, BPM_7) agrees with our knowledge that one vertical plate of BPM 7 did not pick up signals at the time of this experiment. Then we could not measure a vertical beam position change at BPM 7 when we changed the vertical dipole current at RSV 7.

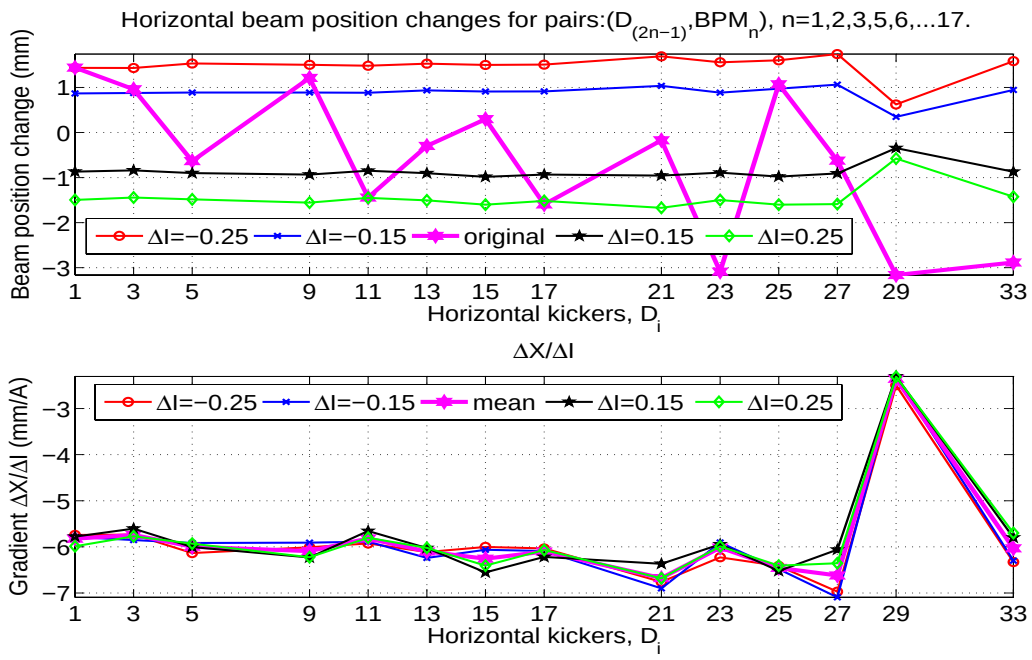

Figure 4.7: Diagnosis step 2.1. The horizontal axis is horizontal dipole number and the vertical axis is horizontal beam position change (in the top plot) or $\zeta_1 = \frac{\Delta X}{\Delta I}$ (in the bottom plot).

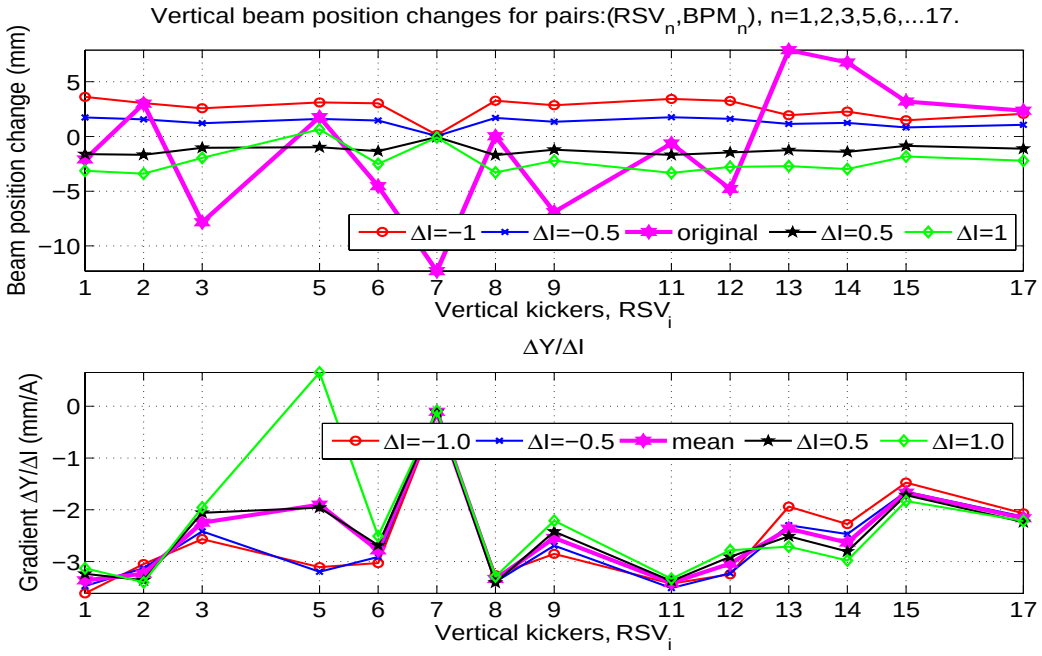

Figure 4.8: Diagnosis step 2.2. The horizontal axis is vertical dipole number and the vertical axis is vertical beam position change (in the top plot) or $\zeta_1 = \frac{\Delta Y}{\Delta I}$ (in the bottom plot).

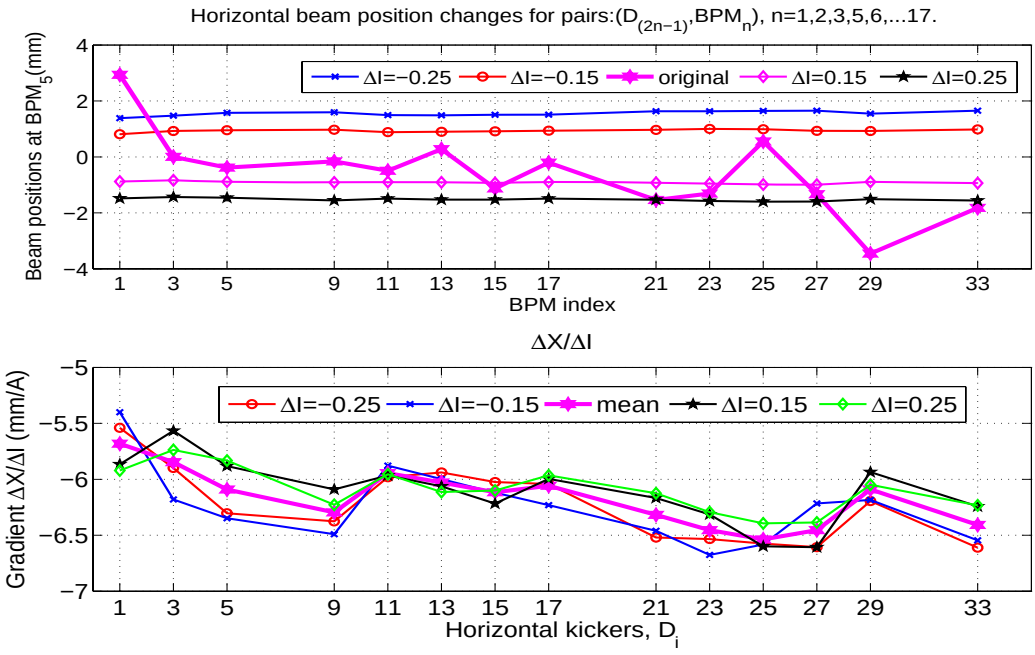

Figure 4.9: Diagnosis step 3.1. The horizontal axis is horizontal dipole number and the vertical axis is horizontal beam position change (in the top plot) or $\zeta_1 = \frac{\Delta X}{\Delta I}$ (in the bottom plot).

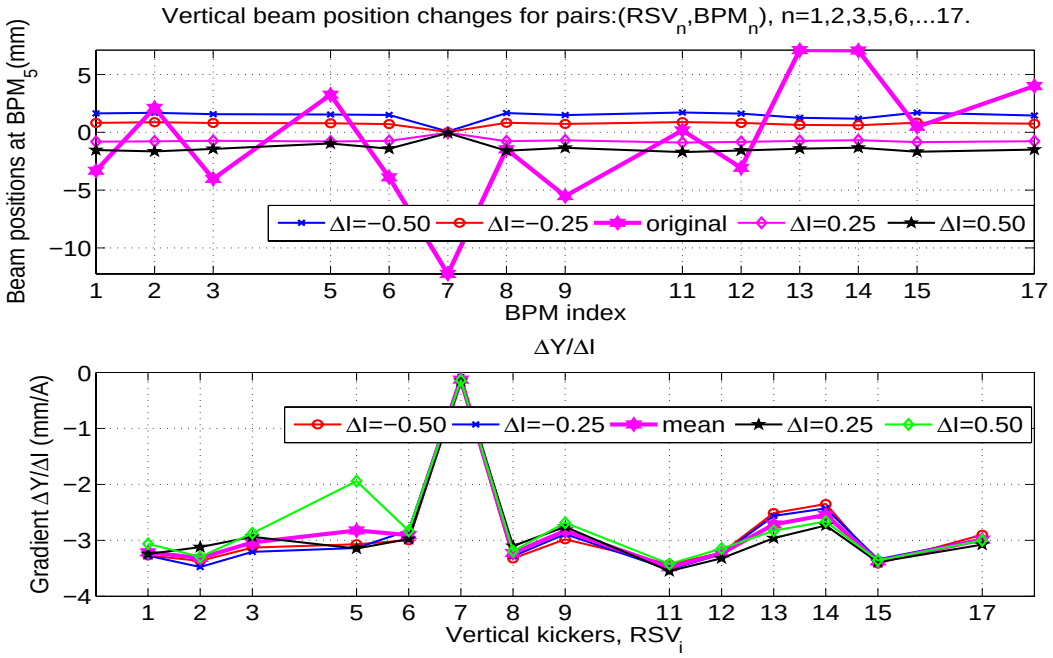

Figure 4.10: Diagnosis step 3.2. The horizontal axis is vertical dipole number and the vertical axis is vertical beam position change (in the top plot) or $\zeta_1 = \frac{\Delta Y}{\Delta I}$ (in the bottom plot).

This simple and fast diagnosis can help us find problems with the BPMs, dipoles and quadrupoles. The whole process takes less than an hour. We recommend this diagnosis as a routine check to identify magnets or BPM issues in UMER.

Comparing the results in the experiment in this section with the results from simulation and from the transfer matrix (theory) in Section 4.2, we found discrepancies between the experimental results and the simulation/theoretical results. The discrepancies come from the uncertainty associated with data acquisition. The beam positions taken from BPMs can achieve a precision of 0.1 mm. Then the precision of ζ_1 is around $\Delta\zeta_1 = \pm 0.2mm/0.25A = \pm 0.8mm/A$ for the horizontal plane, and $\Delta\zeta_2 = \pm 0.2mm/0.5A = \pm 0.4mm/A$.

From the simulations, we have $\zeta_1 = 6.83 \ \ mm/A$; this indicates the experimental ζ_1 should fall in $6.83 \pm 0.8 = 6.03$ and 7.63. Checking Figure 4.9, we find that most of the data points fall in this region except D_1, D_2 and D_3. This is probably due to the injected beam being away from the pipe center which introduces an error.

For the vertical plane, we have $\zeta_2 = 3.26m \ \ m/A$. The experimental value of ζ_2 should fall in region of $(2.86, 3.66)$. Checking the data in Figure 4.10, we find that each data point falls in this region, except RSV 7, where the vertical plates of BPM 7 did not work properly at the time of the experiment.

4.4 Coupling Effect

As stated earlier, a strong coupling exists in the injection and a weak coupling in the ring, both of which should not be neglected in beam matching and beam

steering. The orbit response matrix can help in checking the coupling effect. We confirmed this coupling effect in Figures 4.11 and 4.12. In Figure 4.12, the current change in the horizontal kickers led to vertical beam position change. This indicates that there is some coupling; otherwise, horizontal dipoles will not bend the beam vertically and the off-diagonal elements of the response matrix should vanish.

The coupling complicates our effort in improving the injection beam steering. We are working to find a way to mechanically adjust the steering dipoles and remove, or at least decrease, the coupling. We hope these efforts will improve beam control and ring performance.

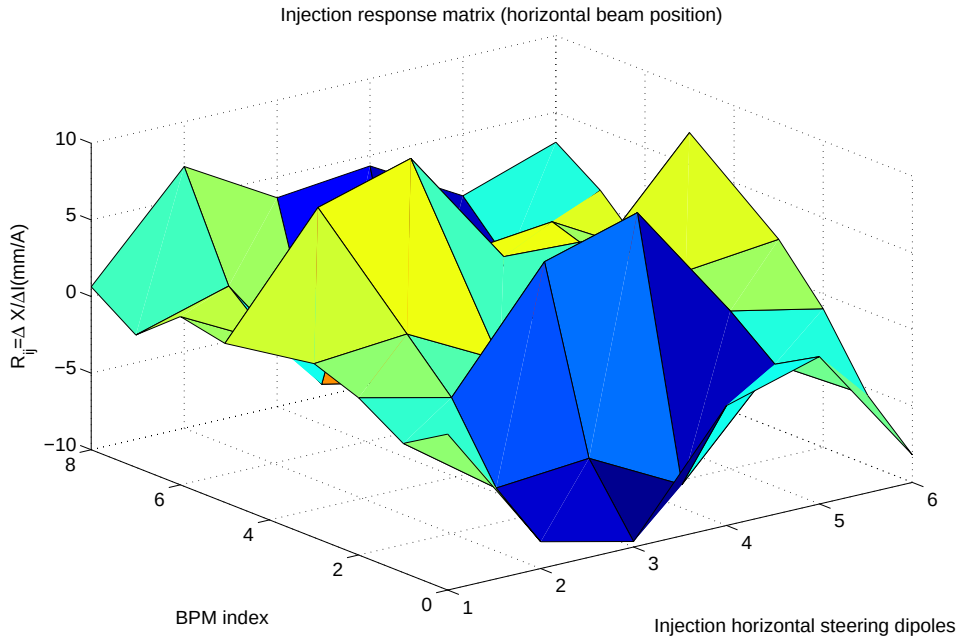

Figure 4.11: Injection response matrix (injection horizontal kickers versus horizontal beam positions). Colors used only to distinguish regions and indicate height.

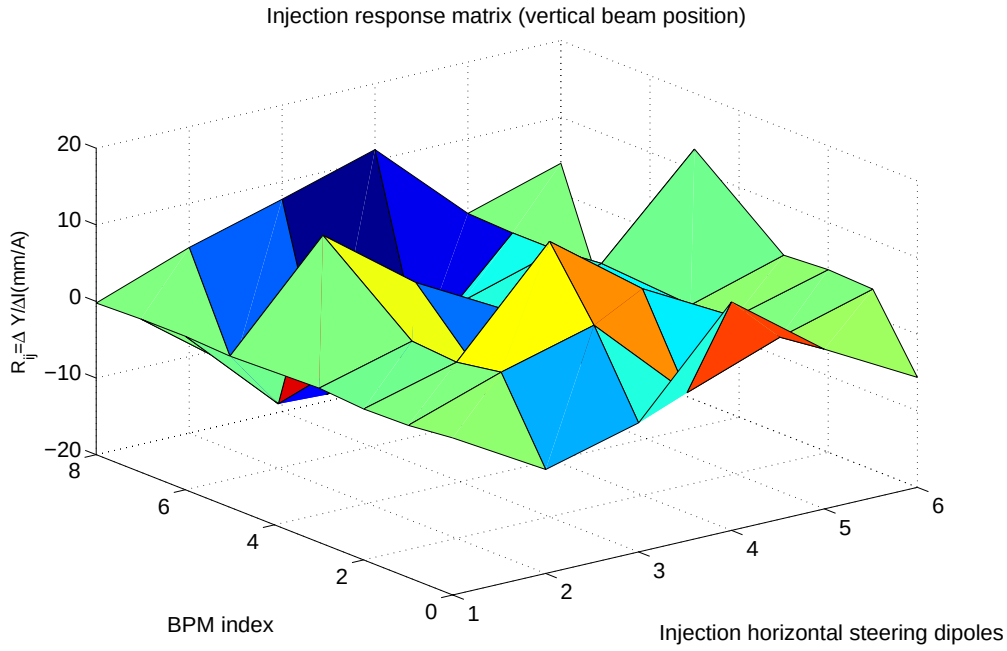

Figure 4.12: Injection response matrix (injection horizontal kickers versus vertical beam positions). Colors used only to distinguish regions and indicate height.

Chapter 5

Control of Electron Beams with Space Charge

In this chapter we focus on the control of electron beams in the University of Maryland Electron Ring. Our goal is to achieve a major improvement in beam quality in terms of several criteria: (1) minimizing particle loss; (2) achieving the largest number of turns and the highest current transmission rate; and (3) keeping the beam size and emittance constant. These three criteria are obviously closely linked.

The first difficulty we face is that the injection is unknown or barely known. If the injection beam is off-center, there will be a large oscillation of beam centroid, which leads to a large betatron oscillation and beam loss. Second, there are a limited number of beam position monitors, which leaves large spaces in the ring not being monitored. Third, there is a coupling between ring steering and injection steering because these share several magnets and measurement devices in the steering process. Our new approach to beam steering takes advantage of the coupling between injection steering and ring steering, employs all the beam position data up to four turns as well as the calculated closed orbit, and minimizes beam centroid oscillation. We also propose a new hybrid beam matching scheme to provide a comprehensive matching solution, and the solution proves to be successful.

This chapter is organized as follows. In Section 1, we give an overview to

problems in beam steering and matching at UMER. In Section 2, we discuss beam steering, introduce a new beam control algorithm and present the experimental results. In Section 3, we propose a new offline hybrid beam matching technique.

5.1 Problems in Beam Steering and Matching

Beam transport over a long distance or for multiple turns requires that beam centroid deviate as little as possible from the design orbit [7, 18, 33]. In order to achieve this, beam should be properly matched and steered. Beam matching involves beam envelope control, which can be achieved by proper quadrupole setting; beam steering involves beam centroid control which relies on the horizontal and vertical kickers. In general, beam matching and beam steering are dealt with separately. Only a well matched and steered beam can guarantee good multi-turn operation and excellent beam quality.

There are currently several major issues in beam steering yet to be solved at UMER. First, we do not know what is the best achievable beam centroid or the best closed orbit. Second, we do not have an algorithm to counter the effects of system environmental change. For example, when the room layout was altered such that the ambient magnetic field in the lab changed, the previous beam steering solution could not respond to this change and did not work well. It would be desirable to have a robust beam steering algorithm which will work under varying laboratory conditions.

5.2 Beam Steering

Beam steering and control have been critical issues for accelerators. In general, the goal is to pass the beam through the centers of the quadrupoles such that there is no deflection to the beam from the quadrupoles.

There have been many approaches for beam steering and control [14, 15, 16]. For example, in the harmonic correction method [14], the most dominated harmonics in the betatron oscillations was identified and corrected. Recently, the SVD and response matrix approach [16] has been widely used in many accelerators. In this approach, the response matrix, as introduced in Chapter 4, was measured and compared with the model response matrix, and the required dipole currents were obtained. A quadrupole-scans assisted beam steering approach was tried on UMER [47]. Although the simulation was successful in this approach, the experimental application on UMER failed to offer a satisfactory result due to insufficient beam position data points. As we can see, these approaches do not work well for UMER because of UMER's unique structure, as discussed in Chapter 2. Nevertheless, we also use the SVD technique, and present a new approach based on the closed orbit response matrix as following.

Beam steering is divided into injection steering, ring steering and recirculation steering at UMER. Injection steering is critical to the overall quality of multi-turn operation. Injecting a beam with a proper profile into the ring prolongs the lifetime of multi-turn operation. However, we find there are coupling effects among the injection steering dipoles and misalignment and rotations in the quadrupoles. These

complicate injection beam steering. In the ring, there are 36 horizontal and 18 vertical dipoles steering the beam. The problem is that not all the horizontal dipoles work unanimously, nor the vertical dipoles. Moreover, the earth magnetic field, which contributes around 20% of bending force for beam steering, is not constant around the ring. The amplitude and direction of the earth magnetic field vary along the ring as shown in Figure 5.1 [42]. In this figure, at every 10 degree, there is a horizontal dipole. For the recirculation steering, the pulses for the injection dipole (*PD_inj*) and recirculation dipole (*PD_rec*) have some jitter. This jitter add noise to the BPM signals, which makes the BPM measurement less reliable, especially for the pencil beam. Because of these problems, beam steering at UMER is very difficult.

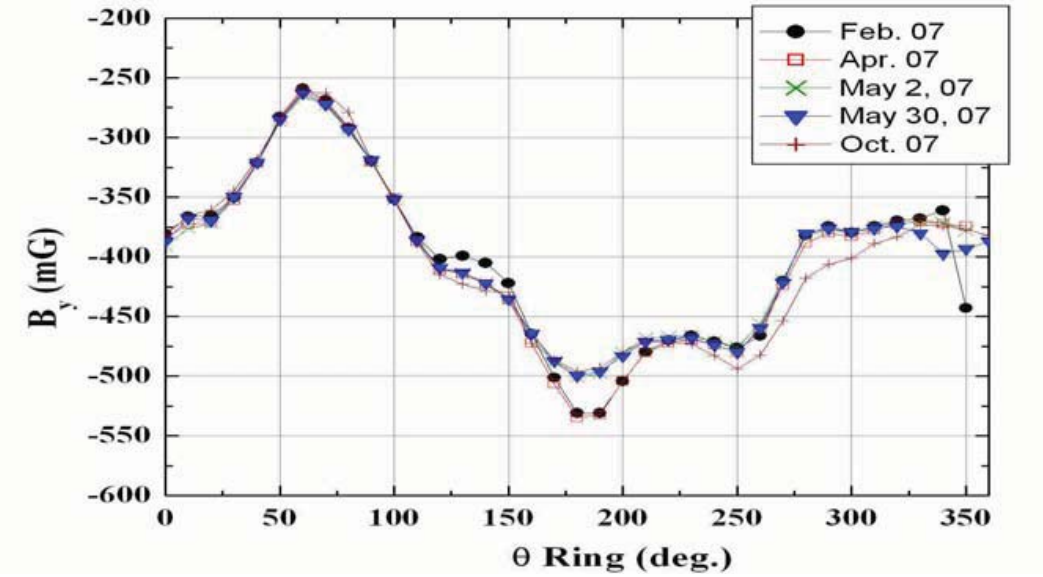

Figure 5.1: Measured laboratory magnetic earth field around the ring in 2007.

In the following subsections, we will introduce two approaches for UMER beam steering: iterative closed-orbit response matrix steering and beam-based alignment.

5.2.1 Iterative Beam Steering with the Orbit Response Matrix

Beam centroid control based on the orbit response matrix has been widely accepted in the accelerator community. This approach is easy to be understood and applied. However, the general orbit response correction method does not work for UMER because there is a strong coupling between the injection and the ring and there are not enough beam position monitors to measure the beam position changes.

Recall the singular value decomposition (SVD) technique in Chapter 2 and the response matrix in Chapter 4. Here we introduce how SVD is applied in beam centroid control. The elements in the horizontal response matrix R are defined as

$$R_{ij} = \frac{\text{horizontal beam position change } \Delta x \text{ at BPM } i}{\text{current change } \Delta I \text{ at horizontal dipole } j} \tag{5.1}$$

Assume the initial beam positions are x_0, we have

$$x_0 = R \times I \tag{5.2}$$

where R has a dimension of $n \times m$, x_0 is a vector of dimension $n \times 1$, and I is the dipole current, a vector of dimension $m \times 1$.

By the SVD, R can be expressed as

$$R = U \times S \times V \tag{5.3}$$

where $U \in R^{n \times n}$ and $U' \times U = I$, $V \in R^{m \times m}$ and $V' \times V = I$, I is the identity

matrix with appropriate dimension, and S is a diagonal matrix in the following form

$$S = \begin{bmatrix} s_1 & 0 & 0 & 0 & ... & 0 \\ 0 & s_2 & 0 & 0 & ... & 0 \\ 0 & ... & ... & ... & ... & 0 \\ ... & ... & 0 & s_L & 0 & ... \\ 0 & ... & ... & ... & ... & 0 \end{bmatrix} \tag{5.4}$$

where $L = \min(\text{m,n})$. Here, we indicate the matrix inverse with a prefix inv. Then the pseudoinverse of S is

$$invS = \begin{bmatrix} \frac{1}{s_1} & 0 & 0 & 0 & ... & 0 \\ 0 & \frac{1}{s_2} & 0 & 0 & ... & 0 \\ 0 & ... & ... & ... & ... & 0 \\ ... & ... & 0 & \frac{1}{s_k} & 0 & ... \\ 0 & ... & ... & ... & ... & 0 \end{bmatrix} \tag{5.5}$$

where $k \leq L$. Note that L is a free parameter to adjust in beam steering. Discussion of how to choose k will follow. The pseudoinverse of R is

$$invR = V \times invS \times U' \tag{5.6}$$

Then the required dipole currents I are given by

$$I = invR \times x_0 \tag{5.7}$$

Note that, x_0 are the beam positions measured when the ring dipoles run at some currents. These currents were the steering solutions obtained from former researchers Li [18] and Walter [19]. These steering solutions can steer the beam

around, but they are not the optimal solutions because we observe large beam loss in multi-turn operation.

As mentioned in Chapter 2, there are several difficulties in directly applying the orbit response matrix and the above formula (5.7). First, there are not enough beam position monitors in the ring. Second, beam steering in the injection must use the beam position monitors in the ring to assist beam position measurement, since there is only one BPM in the injection. This makes the injection steering and ring steering coupled. However, our new approach takes advantage of this coupling. Third, as stated earlier, there is a complicated Y section which focuses the beam and bends the beam, mingling beam matching beam steering.

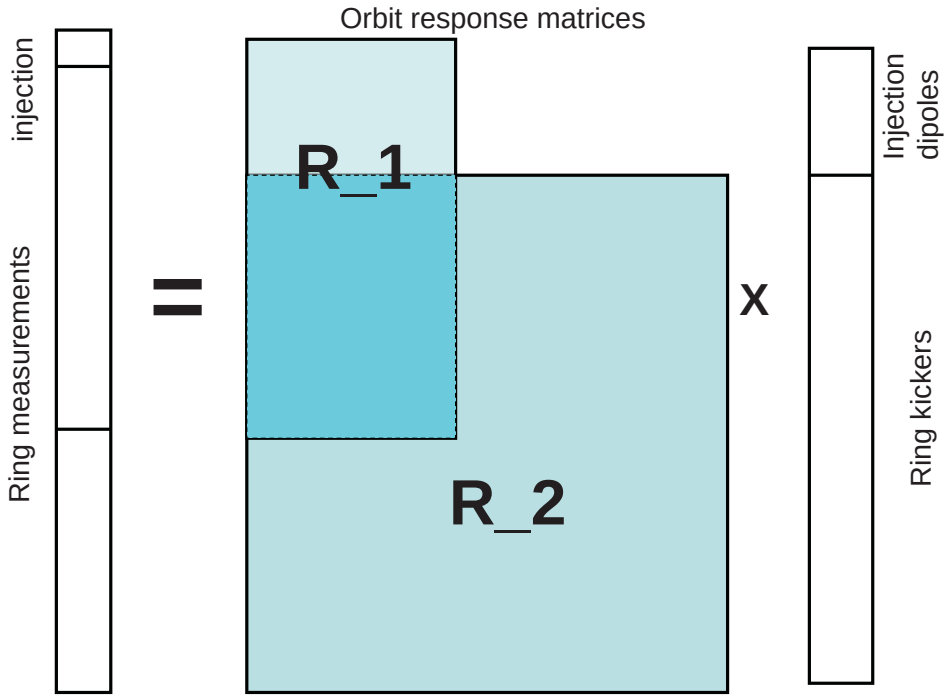

Figure 5.2: UMER Control schematic.

Thus, we propose an iterative beam steering technique using the orbit response

matrix which is illustrated in Figure 5.2. We notice the dark-blue area covers response matrices of R_1 and R_2 since we use BPMs in the ring when we measure the injection response matrix. And the steering procedures are described as follows.

1. Measure the initial beam positions;
2. Construct the injection orbit response matrix R_1;
   (a) Choose a proper k in $invR$;
   (b) Steer the beam in the injection;
3. Construct the ring orbit response matrix R_2;
   (a) Choose a proper k in $invR$;
   (b) Steer the beam in the ring;
4. Repeat above procedures until we get the optimal multi-turn operation and the closed orbit.

Note that in the ring response matrix R_2, there are three possible orbit response matrices, depending how the steering kickers are selected. We can select the ring horizontal kickers only, or the ring vertical kickers only, or both. At the same time, in each step, k is a free parameter for the user to choose. Larger k corresponds to faster convergence of the algorithm, but it may cause power supply saturation. Smaller k corresponds to slower convergence and the algorithm is more stable. The following is the recommended value for k in different situations. If we steer the injection only, $k = 2, 3$. If we steer the ring horizontally only, $k = 8, 9$. If we steer the ring vertically only, $k = 3, 4$.

The optimal multi-turn operation means that there is minimal beam loss from turn to turn. This can be judged from the turn by turn signals on the wall current monitor.

Besides the iterative steering approach above, we proposed a new orbit response matrix. Instead of using the conventional response matrix, we used the closed orbit response matrix. Here, the element in the closed orbit response matrix is different from 5.1. It is defined as the following

$$R_{ij} = \frac{\text{horizontal closed orbit change } \Delta x \text{ at BPM } i}{\text{current change } \Delta I \text{ at horizontal dipole } j} \tag{5.8}$$

where the closed orbit is computed using the four-turn beam position data as the following equation

$$x_{co} = \frac{x_2^2 - x_3^2 + x_2 x_4 - x_3 x_1}{3(x_2 - x_3) + x_4 - x_1} \tag{5.9}$$

where x_1, x_2, x_3 and x_4 are the BPM readings of the first four consecutive turns at the same location. This formula was taken from [36].

The following tables 5.1 and 5.1 present the experimental data for the vertical response matrix. The horizontal response matrix is in the Appendix B.

Table 5.1: Conventional vertical response matrix. "x" indicates no measurement at corresponding location. The quadrupoles were set at 83 % of the design values. To be continued at Table 5.2.

BPM 1	2	3	4	5	6	7	8	9	10	11	12	13	14	15	16	17
-3.23	-1.15	-2.08	x	3.29	0.88	1.93	-3.68	2.94	x	1.97	4.00	-2.95	0.32	-2.54	x	3.00
0.01	-3.42	0.93	x	3.54	2.90	-0.55	-2.28	3.67	x	-0.53	2.53	-3.66	2.59	0.01	x	3.97
0.08	0.05	-3.28	x	-1.42	-3.04	2.72	-0.73	-2.05	x	2.69	0.50	2.10	-3.23	-2.50	x	-2.10
-0.12	-0.04	-0.05	x	1.30	-1.48	3.14	-2.91	0.58	x	3.09	2.93	-0.52	-1.90	-3.15	x	0.48
-0.03	-0.01	-0.07	x	-3.25	-1.12	-1.40	3.29	-2.95	x	-1.67	-3.25	2.72	-0.59	2.10	x	-2.63
0.03	-0.10	-0.14	x	0.00	-3.22	1.00	1.80	-3.64	x	1.06	-2.14	3.48	-2.95	-0.39	x	-3.56
-0.01	-0.06	-0.06	x	-0.07	-0.09	-2.97	1.03	1.75	x	-3.29	-0.69	-2.20	3.49	2.89	x	2.39
-0.05	-0.08	-0.05	x	-0.02	-0.08	-0.10	-3.15	0.89	x	3.14	3.18	-0.72	-1.87	-3.29	x	0.74
-0.07	-0.12	-0.06	x	-0.04	-0.07	-0.14	0.05	-3.30	x	-1.39	-3.43	3.09	-0.92	1.89	x	-2.91
0.02	-0.09	0.03	x	-0.02	-0.08	-0.04	-0.07	-0.03	x	1.16	-1.59	3.19	-2.86	-0.79	x	-3.09

Table 5.2: Conventional vertical response matrix. "x" indicates no measurement at corresponding location. The quadrupoles were set at 83 % of the design values. This table follows Table 5.1.

BPM 1	2	3	4	5	6	7	8	9	10	11	12	13	14	15	16	17
-0.01	-0.04	-0.05	x	0.03	-0.16	-0.04	0.04	-0.07	x	-3.25	-1.05	-1.70	3.18	2.92	x	2.02
0.10	-0.13	0.00	x	-0.05	-0.03	-0.07	-0.03	-0.02	x	-0.09	-3.30	1.05	1.59	3.42	x	-0.77
0.05	-0.14	0.02	x	-0.06	0.01	-0.02	-0.07	-0.07	x	0.03	-0.01	-3.13	1.26	-1.52	x	3.30
0.01	-0.05	0.07	x	0.04	-0.02	0.00	-0.01	-0.01	x	0.01	-0.11	-0.03	-3.12	-1.08	x	-3.25
0.03	-0.08	0.04	x	0.03	-0.04	0.00	-0.04	-0.14	x	-0.04	0.03	-0.07	-0.09	-3.11	x	-1.50
-0.11	-0.03	-0.03	x	0.06	-0.04	-0.07	-0.05	-0.07	x	-0.02	0.06	0.02	-0.04	0.04	x	1.21
-0.05	-0.08	-0.08	x	0.05	-0.03	-0.10	-0.02	-0.01	x	-0.04	-0.04	0.01	0.01	0.02	x	-3.14
0.25	-0.13	0.23	x	-0.17	-0.06	-0.33	0.36	-0.30	x	-0.27	-0.36	0.13	0.10	0.28	x	-0.20

The closed orbit response matrix is given as in Table 5.3 and Table 5.4 based on the above conventional response matrix.

Table 5.3: Vertical closed orbit response matrix. "x" indicates no measurement at corresponding location. The quadrupoles were set at 83 % of the design values. To be continued at Table 5.4.

BPM 1	2	3	4	5	6	7	8	9	10	11	12	13	14	15	16	17
1.59	0.75	-1.91	x	-9.40	-0.62	1.63	4.20	5.19	x	1.73	2.07	-0.79	84.26	-1.78	x	4.25
-2.03	-1.20	-0.36	x	-7.20	2.75	0.17	4.62	9.33	x	0.37	2.31	-0.74	75.94	-0.50	x	1.54
0.66	-0.86	-1.22	x	-10.84	-2.72	1.37	22.78	6.86	x	1.13	-0.72	2.91	79.73	-1.07	x	-3.14
2.62	0.59	1.32	x	-8.75	-2.06	1.95	2.05	10.38	x	1.96	0.88	1.83	80.77	-1.82	x	-1.47
-2.59	-1.56	-0.05	x	-8.95	0.17	3.02	12.22	10.69	x	-0.64	-2.07	0.87	78.73	-0.31	x	-1.07
-1.31	-1.84	1.52	x	-7.54	-1.91	0.68	13.16	6.66	x	0.12	-2.54	2.86	81.12	-0.22	x	-3.03
-2.84	0.15	-1.87	x	-8.50	-21.45	-2.94	6.00	9.80	x	-1.78	1.24	-1.17	81.59	1.58	x	2.14
3.01	0.59	1.45	x	-10.80	-0.76	-1.03	0.76	8.94	x	2.03	1.00	1.99	81.40	-1.94	x	-1.90
-2.78	-1.73	0.04	x	-5.76	1.44	6.04	8.30	9.17	x	-0.65	-2.47	1.32	77.66	-0.98	x	-1.29
-1.10	-1.68	1.57	x	-7.56	1.29	-0.33	11.83	10.33	x	0.14	-2.15	2.60	81.23	-0.34	x	-2.73

Table 5.4: Vertical closed orbit response matrix. "x" indicates no measurement at corresponding location. The quadrupoles were set at 83 % of the design values. This table follows Table 5.3.

BPM 1	2	3	4	5	6	7	8	9	10	11	12	13	14	15	16	17
-3.48	0.04	-1.81	x	-8.37	-32.29	0.38	4.81	8.21	x	-1.69	0.92	-0.86	81.54	1.53	x	1.99
-2.99	-0.96	-1.17	x	-9.27	2.97	0.70	12.52	8.72	x	1.44	-0.93	-53.37	81.73	1.42	x	1.06
180.93	1.77	-0.34	x	-11.24	-1.49	0.14	7.12	5.53	x	0.07	-1.13	-0.13	60.96	-1.29	x	0.11
-0.99	-1.65	1.71	x	-8.05	1.08	-0.66	12.02	9.95	x	-1.34	-0.83	-0.07	80.63	-0.58	x	-2.91
1.38	-0.60	2.20	x	-10.10	-0.03	-1.41	-32.66	7.99	x	-1.90	-1.91	1.81	82.57	-1.30	x	-3.30
3.42	0.91	1.26	x	-15.32	-1.27	-0.90	6.24	7.53	x	-1.15	-2.23	3.20	82.17	1.30	x	-1.78
-2.70	-1.67	0.02	x	-6.37	1.23	20.11	8.19	11.45	x	1.14	0.78	-1.45	78.01	-9.41	x	-1.25
-0.73	-1.45	1.73	x	-8.26	0.85	-0.91	12.39	9.56	x	-1.41	-0.98	0.16	83.48	0.71	x	0.16

Figure 5.3 compares the singular values for these two response matrices. It is clear that in the closed orbit response matrix, the ratio of largest singular value to smallest singular value is larger than the ration in the conventional response matrix. That means in the closed orbit response matrix, the resulting control solution is more sensitive to the beam position change.

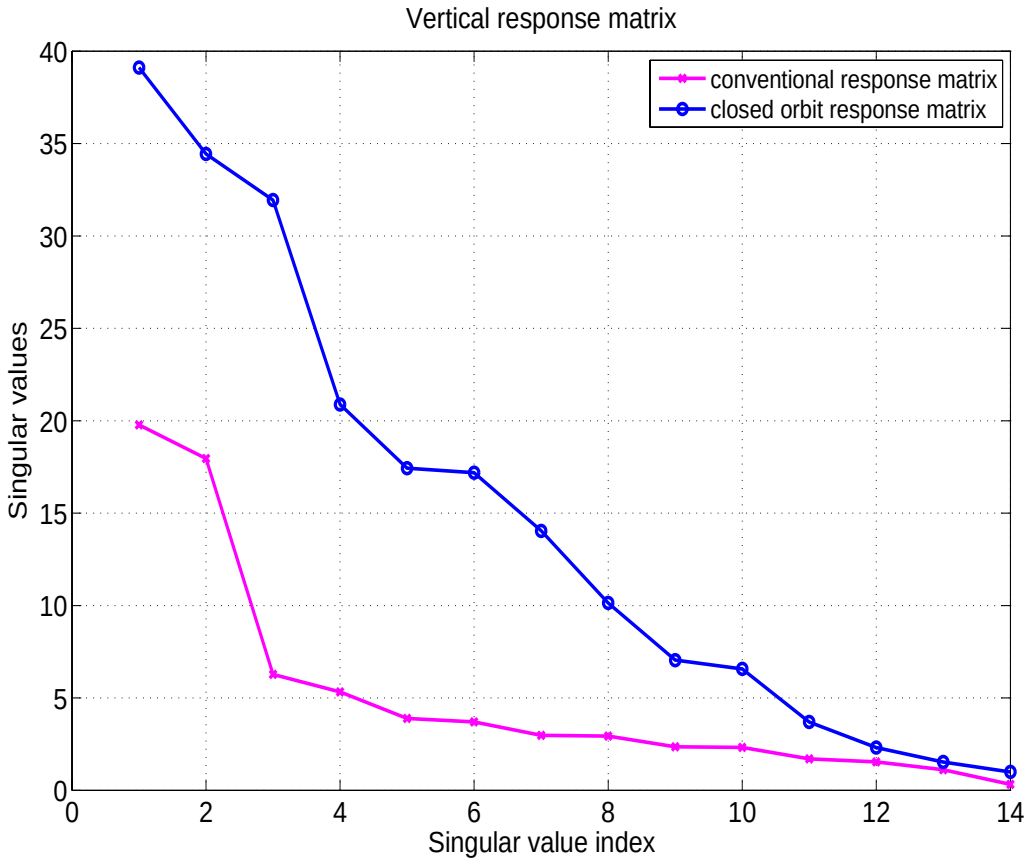

Figure 5.3: Singular values for two vertical response matrices (7 mA beam).

The advantage of this approach is that it directly minimizes the closed orbit distortion. The conventional orbit response matrix only minimizes the first turn beam positions. However, the closed orbit is affected by not only the first turn beam positions, but also beam positions of the other three subsequent turns. By

relating with beam positions of the other three turns, we are able to minimize the centroid oscillations along all the beam position monitors. In the steering process, we first use the conventional response matrix, then use the closed orbit response matrix until we get a satisfactory steering results.

The following two tables Table 5.5 and Table 5.6 summarize the steering solutions for UMER. For the measured conventional horizontal response matrix and the calculated closed orbit response matrix, please see tables in Appendix E.

Finally, we compared the beam positions (Figure 5.4), the closed orbit (Figure 5.5) and the wall current monitor signals (Figure 5.6) from the previous steering solution and the new steering solution. From Figure 5.4, we see there is a significant improvement in reducing both horizontal and vertical beam positions. From Figure 5.5, we see there is a big improvement in minimizing the closed orbit with the new steering solution. In Figure 5.6, we compared the wall current monitor signals with the old and new steering solutions. We see that with new steering solution, there is almost no beam lost for the first ten turns, while there is less than 10% current maintained at the tenth turn with the old steering solution.

With the new steering solutions, we have achieved significant improvement in beam steering for all five UMER beams, from low space charge to intense space charge. For the pencil beam, we have achieved 250 turns with little beam loss. For the 100 mA beam, we can maintain 70% of beam current at the tenth turn. These have never been achieved before.

Table 5.5: Steering solution for ring horizontal bending dipoles. The quadrupoles were set at 83 % of the design value.

Names	Pencil	7mA	23mA	100mA	Names	Pencil	7mA	23mA	100mA
D1	2.411	2.75	2.892	2.483	D19	2.244	2.257	2.257	2.24
D2	2.437	2.38	2.28	2.695	D20	2.8	2.835	2.863	2.929
D3	2.462	2.65	2.712	2.636	D21	2.7	2.641	2.641	2.811
D4	2.504	2.75	2.831	2.54	D22	1.7	1.85	1.778	1.758
D5	2.552	2.536	2.536	2.599	D23	1.8	2.05	2.1	2.013
D6	2.584	2.47	2.47	2.521	D24	2.238	2.443	2.443	2.467
D7	2.584	2.577	2.577	2.597	D25	2.226	2.318	2.318	2.391
D8	2.552	2.594	2.594	2.515	D26	2.239	2.492	2.492	2.474
D9	2.499	2.498	2.498	2.409	D27	2.277	2.443	2.443	2.454
D10	2.444	2.481	2.481	2.392	D28	2.32	2.463	2.463	2.382
D11	2.396	2.539	2.539	2.385	D29	2.348	2.407	2.407	2.382
D12	2.364	2.454	2.454	2.303	D30	2.364	2.194	2.194	2.317
D13	2.35	2.341	2.341	2.203	D31	2.382	2.321	2.321	2.423
D14	2.34	2.488	2.488	2.332	D32	2.398	2.598	2.598	2.504
D15	2.312	2.464	2.464	2.283	D33	2.404	2.347	2.347	2.434
D16	2.272	2.326	2.326	2.241	D34	2	2.004	2.004	1.973
D17	2.24	2.017	2.017	2.25	D35	1.8	1.807	1.807	2.024
D18	2.231	2.316	2.316	2.163					

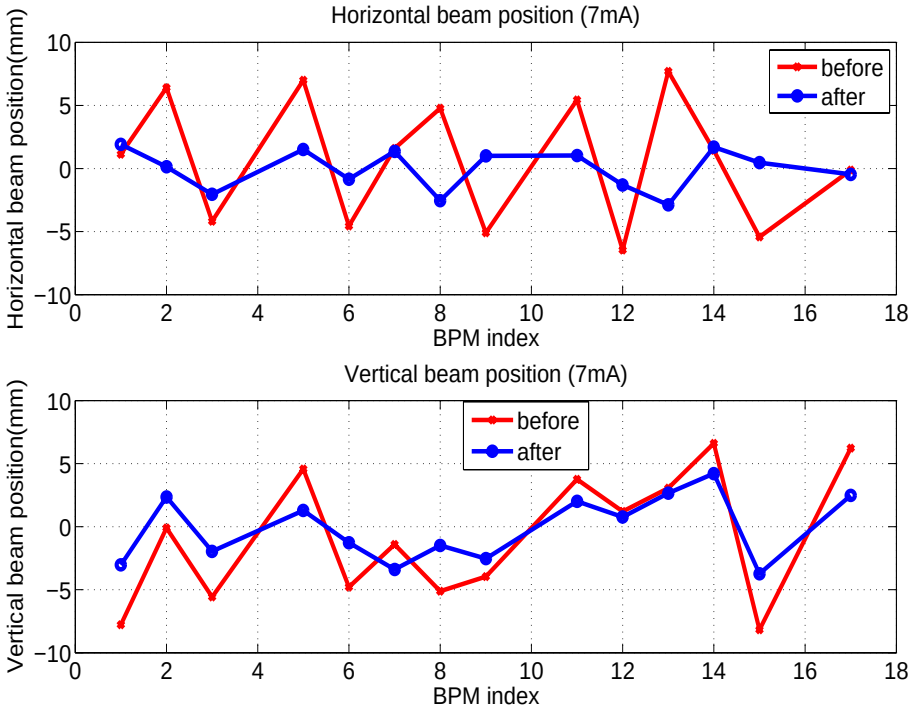

Figure 5.4: Comparison of beam positions before and after steering (7 mA beam).

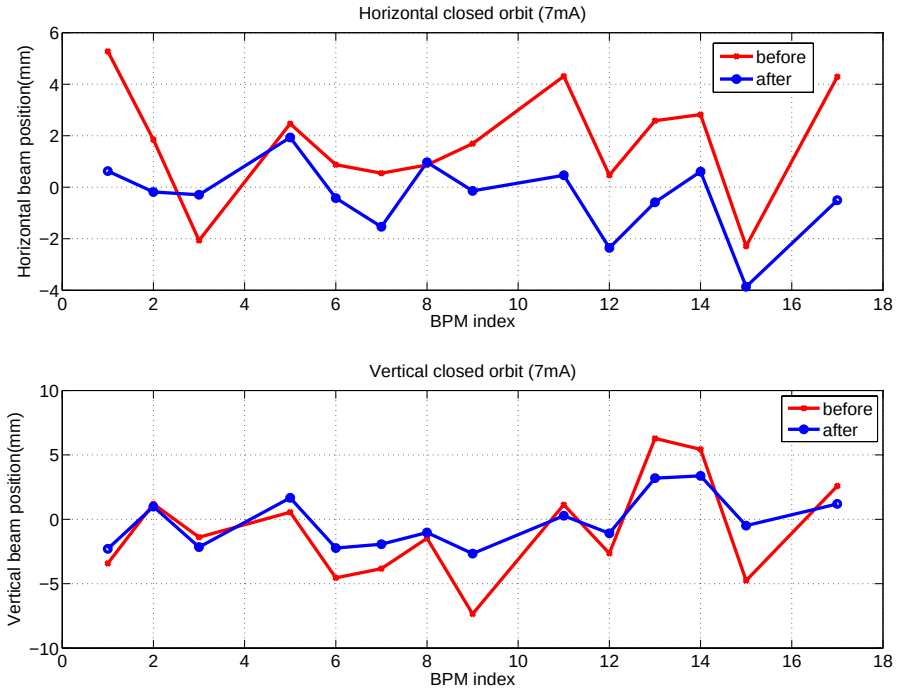

Figure 5.5: Comparison of closed orbits before and after steering (7 mA beam).

Table 5.6: Steering solution for ring vertical dipoles. The quadrupoles were set at 83 % of the design value.

Names	Pencil	7mA	23mA	100mA	Names	Pencil	7mA	23mA	100mA
RSV1	-0.5	1.1	-0.266	-0.876	RSV10	0	-0.4	0.445	0.532
RSV2	-0.5	-0.8	0.15	-0.144	RSV11	0	0.15	0.235	-0.85
RSV3	-0.25	-0.12	-0.155	-1.421	RSV12	0	0.175	0.21	0.496
RSV4	0	0.15	-0.177	0.694	RSV13	0	-0.168	-0.25	-0.835
RSV5	0	0.35	-0.15	-0.25	RSV14	0	0.189	-0.25	-0.225
RSV6	-0.5	-0.4	0.15	0.118	RSV15	0	0.445	-1.3	-0.439
RSV7	1.25	0.3	0.175	0.533	RSV16	0	0.235	-0.6	-0.361
RSV8	0	-0.3	-0.168	0.148	RSV17	0	0.21	0.356	0.44
RSV9	0	-0.5	0.189	0.15	RSV18	0.35	-0.25	0.135	-0.076

5.2.2 Beam-Based Alignment

Beam-based alignment is a common approach for beam steering. This approach was used by Li [18] to steer the beam. He used the phosphor screen to take beam photos and used those photos to calculate the beam positions. In this section, we present an approach which uses the beam position monitors and automates the steering process. It is relatively easy and fast. There is an assumption in this approach that horizontal(x) steering and vertical (y) steering are decoupled. This decoupling assumption does not hold in the injection, since there is a rela-

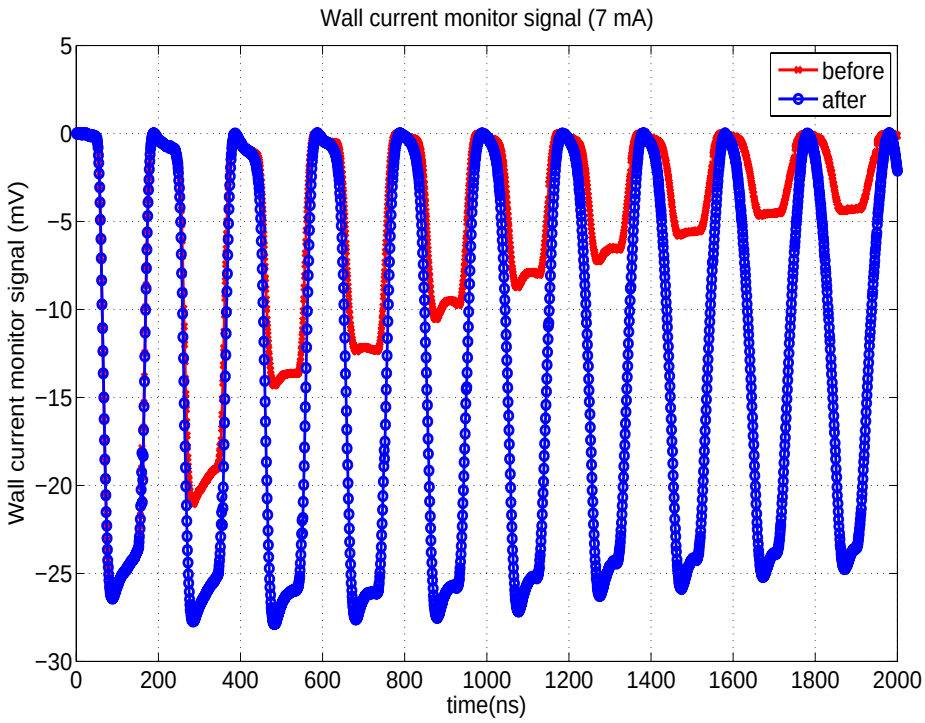

Figure 5.6: Comparison of wall current monitor signals before and after steering (7 mA beam).

tively strong coupling in the injection horizontal and vertical kickers, which has been demonstrated in Chapter 4. The coupling in the ring horizontal and vertical kickers is relatively weak so the assumption holds in the ring. This method applies to ring steering only. Since it was discussed in [18], here, we only explain how to implement this technique. Readers can refer to [18, 43] for detailed mathematical computations.

Figure 5.7 is the diagram for the beam-based alignment in an ideal optics where everything is aligned well. In this figure, two steering dipoles (S_1, S_2) steer the beam into the centers of quadrupole Q_1 and BPM. However, in practice, the center of the BPM is not precisely known, and the quadrupole center and BPM center are not

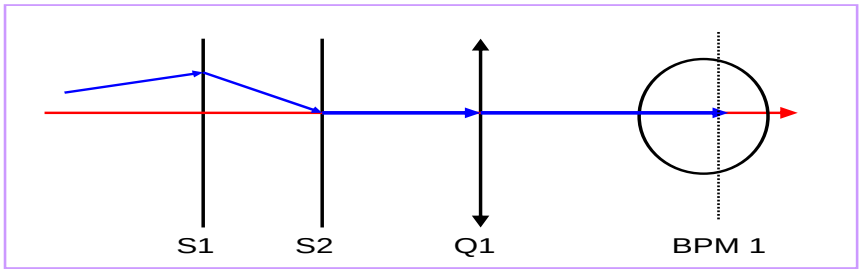

Figure 5.7: Schematic diagram of optics in an ideal beam-based alignment approach.

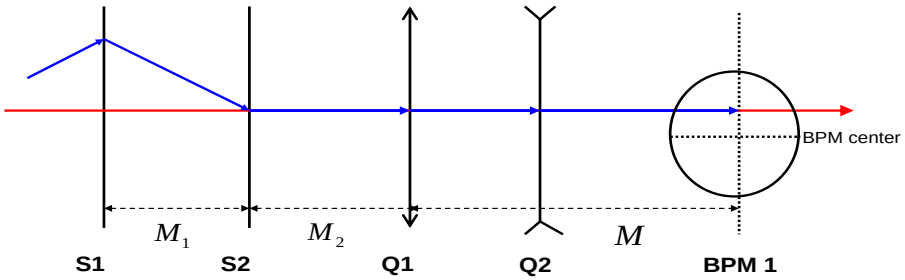

Figure 5.8: Schematic diagram of optics in an improved beam-based alignment approach.

perfectly aligned either. These problems are solved by two quadrupole scans as shown in Figure 5.8 and have the following procedures.

1. Find a group of (I_{s1}, I_{s2}) which steer the beam into the center of Q_1,

2. Scan Q_2 to detect the optimal (I_{s1}, I_{s2}).

In order to scan quadrupole Q_1, the experiment is set up as follows

1. Set a current pair (I_{s1}, I_{s2}),

2. Set Q_1 current at I_{q1} and measure the beam position x_1 at a specified BPM,

3. Set Q_1 current at $I_{q1} + \Delta I_{q1}$ and measure the beam position x_2 at the same BPM, where ΔI_{q1} is a reasonable constant,

4. Group data set $(I_{s1}, I_{s2}, x_i = x_2 - x_1)$,

5. Repeat Step 1-4 as above until enough data is obtained.

Here, "reasonable" means either the quadrupole currents exceed their maximum currents or the measured beam positions are beyond ± 10 mm.

From the experiment above, we will have a group of data (I_{s1}, I_{s2}, x) and we can do a linear regression fitting to find the relationship between (I_{s1},I_{s2} and x. Obviously, we need another set of equations to solve the whole problem. The additional equation is obtained by scanning quadrupole Q_2 as follows:

1. Set a reasonable value for I_{s1},

2. Set Q_2 current at I_{q2} and measure the beam position x_1 at a specified BPM,

3. Set Q_2 current at $I_{q2} + \Delta I_{q2}$ and measure the beam position x_2 at the same BPM, where ΔI_{q2} is a reasonable constant,

4. Group data set $(I_{s1}, x_i = x_2 - x_1)$,

5. Repeat Step 1-4 as above until enough reasonable data is obtained.

Similarly, from the experiment above, we will have another group of data (I_{s1}, x) and we can do a linear regression fitting on (I_{s1} and x as well. Combining those two equations, we have

$$\begin{cases} \Delta x_{q1} = \Delta(I_{s1}, I_{s2}) = A_0 + A_1 \cdot I_{s1} + A_2 \cdot I_{s2} \\ \Delta x_{q2} = \Delta(I_{s1}) = C_0 + C_1 \cdot I_{s1} \end{cases} \tag{5.10}$$

where Δx_{q1} is the beam position change when scanning Q_1, and Δx_{q2} is the beam position change when scanning Q_2.

Then, the optimal solutions $(I_{s1}^{opt}, I_{s2}^{opt})$ are given by the following formulae

$$\begin{cases} I_{s1}^{opt} = -\frac{C_0}{C_1} \\ I_{s2}^{opt} = -\frac{A_0}{A_2} - \frac{A_1}{A_2} I_{s1}^{opt} \end{cases} \tag{5.11}$$

This technique can provide us a basic first-turn steering solution. In some accelerators, this technique can provide a good multi-turn steering solution [41]. However, some limitations exist in this technique. For example, if A_2 in (5.11) is very small, the result will be unreliable. If the BPM signal is too noisy, the linear regression in scanning Q_1 and Q_2 will not converge. Another difficulty lies in the choice of dipoles and quadrupoles. In UMER, we can only steer the beam to the center of half of the quadrupoles; for the other half of quadrupoles, we don't know the beam positions inside those quadrupoles.

5.3 Beam Matching

There are many mathematical models for beam envelope dynamics [7]. Here, we use the Kapchinsky-Vladimirsky (K-V) equation to describe the transverse beam

envelope dynamics as the following:

$$\frac{dX^2(s)}{ds} = -k_x X(s) + \frac{2K}{X(s)+Y(s)} + \frac{\epsilon_x^2}{X(s)^3} \tag{5.12}$$

$$\frac{dY^2(s)}{ds} = -k_y Y(s) + \frac{2K}{X(s)+Y(s)} + \frac{\epsilon_y^2}{Y(s)^3} \tag{5.13}$$

where $X(s), Y(s)$ are the sizes of beam envelope in the transverse direction, κ_x and κ_y are the focusing/defocusing strength of the quadrupoles, ϵ_x, ϵ_y are the emittance, and K is the generalized perveance which is defined as follows

$$K = \frac{I}{I_0}\frac{2}{\beta^3\gamma^3} \tag{5.14}$$

Here I is the beam current and

$$I_0 = \frac{4\pi\epsilon_0 mc^3}{q} \tag{5.15}$$

is the characteristic current, and $\beta = \frac{v}{c}$ where v is the beam speed, c is the speed of light in vacuum, $\gamma = \frac{1}{\sqrt{1-\beta^2}}$, and $I_0 = 1.7e04$ amp for electrons.

The envelope equations for a matched beam using smooth approximation method [7] are

$$\begin{cases} \kappa_x X = \frac{2K}{X+Y} + \frac{\epsilon_x^2}{X^3} \\ \kappa_y Y = \frac{2K}{X+Y} + \frac{\epsilon_y^2}{Y^3} \end{cases} \tag{5.16}$$

The purpose of beam matching is to provide the correct quadrupole strength κ_x and κ_y such that Equation (5.16) is satisfied.

For a round beam where $X = Y = a, \epsilon_x = \epsilon_y = \epsilon$, the above equations are simplified as:

$$\kappa_0 a = \frac{K}{a} + \frac{\epsilon^2}{a^3} \tag{5.17}$$

where the beam is circular in the transverse plane.

5.3.1 Offline Beam Matching

The beam radius in the ring is determined by quadrupole settings which are typically fixed at one value. The matching problem hence consists of adjusting the quadrupole settings in the injection line so as to provide a beam with correct size and shape at the exit of the injector. Recirculation is complex, since two of the injection magnets are shared by the ring. Therefore, beam matching on UMER focuses on the injection matching. We have developed an offline beam matching approach, which is described in Figures 5.10, 5.11 and 5.12 in a sequential order.

Figure 5.9 is a schematic diagram of the injection and recirculation of UMER. The injection includes a solenoid and six quadrupoles (Q1, Q2, Q3, Q4, Q5, Q6). Each quadrupole has its own power supply. The beam is introduced through these quadrupoles into the ring. After that, the beam should have desired beam radii and slopes, which will later be fitted in the ring's quadrupole configuration. The injection is not periodic and has only one diagnostic device. Other problems are associated with the initial beam conditions, magnet modeling/locations, effects from the injection bending dipoles, etc. However, within proper handling of these undesired elements, good beam matching is still achievable. The initial beam conditions were measured through a tomography technique by a former student Stratakis [44].

It is difficult to have a good beam matching solution partly because of the unique ring structure where a single quadrupole YQ is shared between injection and recirculation and, is off-centered relative to both trajectories. Another quadruple, QR_1 is also different from other normal quadrupoles. Modeling both YQ and QR_1

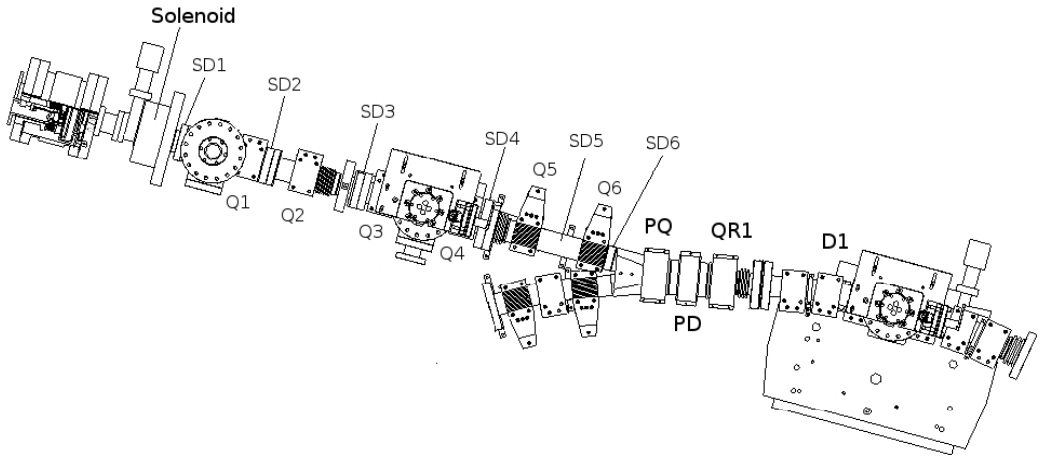

Figure 5.9: Schematic diagram of UMER injection.

is difficult. Moreover, these two magnets both focus and bend the beam such that beam steering and matching are coupled. The standard optimization codes like TRACE3D [45] cannot offer an accurate matching solution. We have performed experiments with different algorithms for selecting injection line magnet settings to achieve optimal matching in the ring and developed a hybrid scheme using WARP to model the solenoid and injection Y and TRACE for the optimization.

In the following three Figures 5.10, 5.11 and 5.12, we describe how the hybrid scheme works in three steps. Each figure discuss one step and the three steps were introduced in the sequential order.

In Figure 5.10, we present the result of the first step which optimizes *FODO* matching in the ring such that the beam starting from QR3 will match itself at QR5. Since the ring is periodic, it will be automatically matched in the following chambers until QR_{70}. This step determines all ring quadrupole settings from QR_3 to QR_{70}.

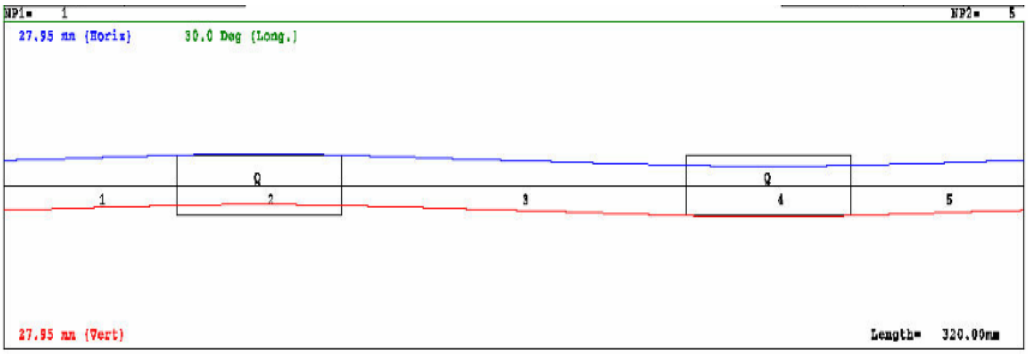

Figure 5.10: Beam matching step I.

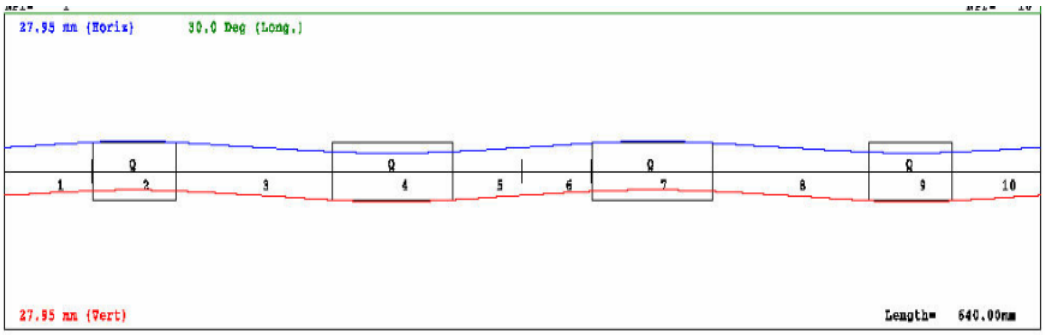

Figure 5.11: Beam matching step II.

In Figure 5.11, we show the results of the second step which optimizes matching in the recirculation, from QR71 to QR2. This step determines the magnet setting for YQ, QR_1 and QR_2. Since the recirculation is shared by the injection line and recirculation line, the values obtained here will be used in the next step-injection matching.

In Figure 5.12, we present the results of the third and last step which optimizes the matching in the injection. This step computes and optimizes the quadrupole currents from Q_1 to Q_5 in the injection line.

At the most commonly used operating point, the ring quadrupoles operate at

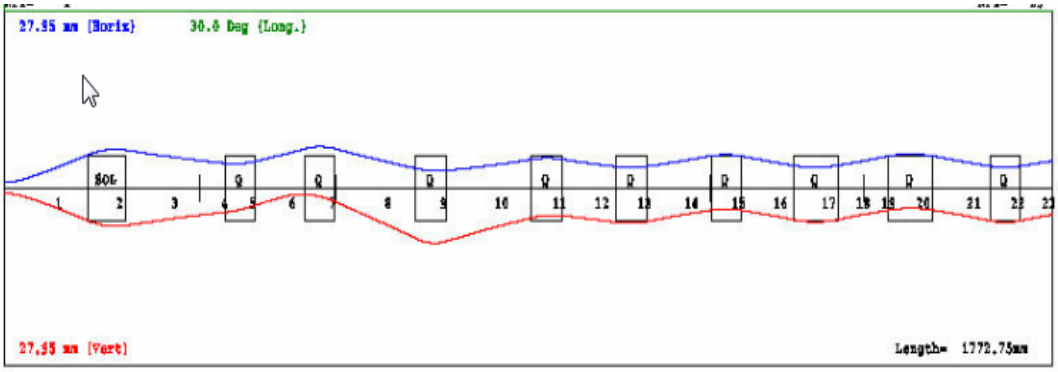

Figure 5.12: Beam matching step III.

83% of their design value of 2.21 A. In Table 5.7, we summarize the new matching solution for the pencil (0.7 mA) beam. Other matching solutions are documented in the technical notes [46] and Appendix C.

Because YQ and QR_1 are constructed different from other quadrupoles, we do not have a very accurate model for them at the time being. Thus the currents for them calculated from Table 5.7 are not reliable. We manually adjust the currents of YQ and QR_1 in order to optimize the matching scheme for the ring. When we manually adjust the currents of YQ or QR_1, we measure the first turn wall current monitor signal strength on an oscilloscope. When the signal achieves maximum, the corresponding values for YQ and QR_1 are the best matching solutions for that beam.

With the three steps described above, the parameters for the final matched beam are obtained. We call the beam with those parameters the target beam. The parameters of the target beam shown in Table 5.8 can be used for future simulations and experiments.

Table 5.7: Calculated injection matching solution for the pencil beam at 83% operating point. Note that YQ and QR_1 need manual adjustment.

Magnet	Position [cm]	Peak Field[G]/Gradient[G/cm]	Current [A]
SOL	17.39	98.10	5.50
Q1	39.86	4.30	1.19
Q2	53.41	7.22	2.00
Q3	72.19	6.54	1.81
Q4	91.76	4.03	1.12
Q5	106.12	2.75	0.76
Q6	122.10	6.73	1.86
YQ	137.28	4.83	4.74
QR1	153.28	4.83	4.79
QR2	169.28	6.73	1.86
QR3	185.28	6.61	1.83
QR70	1257.28	6.61	1.83
QR71	1273.28	6.73	1.86

Table 5.8: The calculated target beam parameters at the middle plane of the dipole between QR_2 and QR_3, where $a0$ is the beam position, $ap0$ is the beam angle in x direction, and $b0$ is the beam position and $bp0$ is the beam angle in y direction. The ring quadrupoles operate at the 83% operating point.

	a0	ap0	b0	bp0
pencil	1.85	4.75	1.85	4.75
7 mA	3.80	14.55	3.80	14.55
23 mA	6.13	22.96	6.13	22.96
100 mA	12.42	46.24	12.42	46.24

Chapter 6

Conclusions and Suggestions for Future Work

6.1 Conclusions

In this dissertation we reported results of beam control and simulation applied to the University of Maryland Electron Ring (UMER).

In Chapter 2, we discussed some of main issues and problems being faced in simulation and experimental studies on UMER.

In Chapter 3, we studied the resonance and tune of UMER. We compared tune calculation results from several simulation codes and using several quadrupole models, and concluded that a nonlinear quadrupole model with a fringe field is the best available model for UMER quadrupoles. We confirmed that random quadrupole position alignment error (either in the normal distribution or in the uniform distribution) in the lattice triggers integer resonance, while random quadrupole strength error in the lattice triggers the half-integer resonance. In the experiment, from the wall current monitor signals, we detected in the beams the effects of space-charge forces which shift resonance points. We also found that the pulse length of the beam does not affect the resonance point, but it affects the beam decay speed in multi-turn beam transport.

In Chapter 4, we presented a system diagnosis method based on the orbit response matrix which is aimed at detecting malfunctioning BPMs and dipoles.

Because of the periodicity of the ring structure, certain elements in the orbit response matrix should be identical or nearly so. We started with a simple test on dipoles $D1$ and $D3$, which proved to be successful. Then we applied the method to the whole ring. In only three consecutive steps, we identified problems of failing power and signal cable connections, and fixed those problems. We believe this diagnosis method can help others in diagnosing their systems if their systems present some kind of periodicity or other special properties.

In Chapter 5, we developed a new iterative beam steering algorithm based on the closed orbit response matrix and successfully applied this algorithm to UMER. For systems which have limited number of beam position monitors and coupling between injection and ring, such as UMER, this method provides a new approach for beam control. And we presented the experimental procedures for the beam-based alignment. Furthermore, in this chapter we developed a new offline hybrid beam matching algorithm which offers a good matching solution. We applied the iterative beam steering and the hybrid beam matching on UMER, and obtained the best multi-turn operation results for all UMER beams.

6.2 Suggestions for Future Work

Several suggestions for further work are given as follows:

1. BPM malfunction is always a concern for beam diagnostics and control. It will be helpful to find an algorithm to decide how many BPMs are needed for sufficient measurement and where the BPMs should be located to achieve

the best beam steering. If we call these BPMs resources, this is a resource optimization problem [51], of a type which has attracted interest from many researchers.

2. Beam diagnostics, as described in Chapter 4, have been very successful in detecting malfunctioning parts of the ring. A full coverage of analysis on every magnet and BPM would be very useful. Such a study would help make system maintenance easy and smooth.

3. There is an error in computing the tune for beams with intense space charge, such as the 23mA beam, because there is a large beam loss during beam transport. A research opportunity exists to improve the tune computation with improved multi-turn beam recirculation. At the same time, quantifying how much the tune changes during multi-turn beam recirculation would also contribute to the study of the space-charge-dominated beams.

4. Simulations of UMER, which have difficulty in accurately modeling YQ and QR_1, can be improved after we obtain an improved understanding of these two magnets. We believe this would be key to closing the gap between simulations and experiments in resonance studies and tune computations.

Appendix A

Introduction to Matlab-Based Program *UMER_Control*

The program *UMER_Control* has been developed for data acquisition, system diagnosis and beam control. This program is based on Matlab. We use Labview programs for controlling the power supplies of quadrupoles and dipoles. As introduced in Chapter 2, there are three main beam measurement devices: the beam position monitor, phosphor screen and wall current monitor. In beam control, beam position monitors are used and a switch box controls how to select the corresponding beam position monitor. The program *UMER_Control* communicates with the Labview-based computer to control power supplies through TCP-IP connection. The program controls the BPM switch box to select the corresponding BPM and then takes all BPM signals from the oscilloscope. After the data is collected, the program analyzes the data and makes corresponding decision upon request.

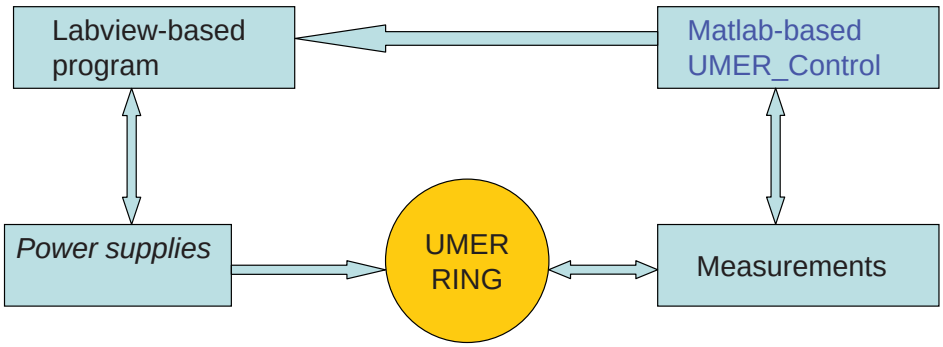

Figure A.1: UMER Control methodology.

The program *UMER_Control* separates the hardware operation (power supply configuration) from the beam measurement and beam optimization. As shown in Figure A.1, the Labview-based program is in charge of controlling the power supply and the power supply controls the ring. The Matlab-based *UMER_Control* only talks to the Labview-based computer, which in turn controls the power supply. In addition, *UMER_Control* talks to the oscilloscopes and records the BPMs signals.

Figure A.2 is a screenshot of this program. It includes beam steering, system diagnosis and other functions.

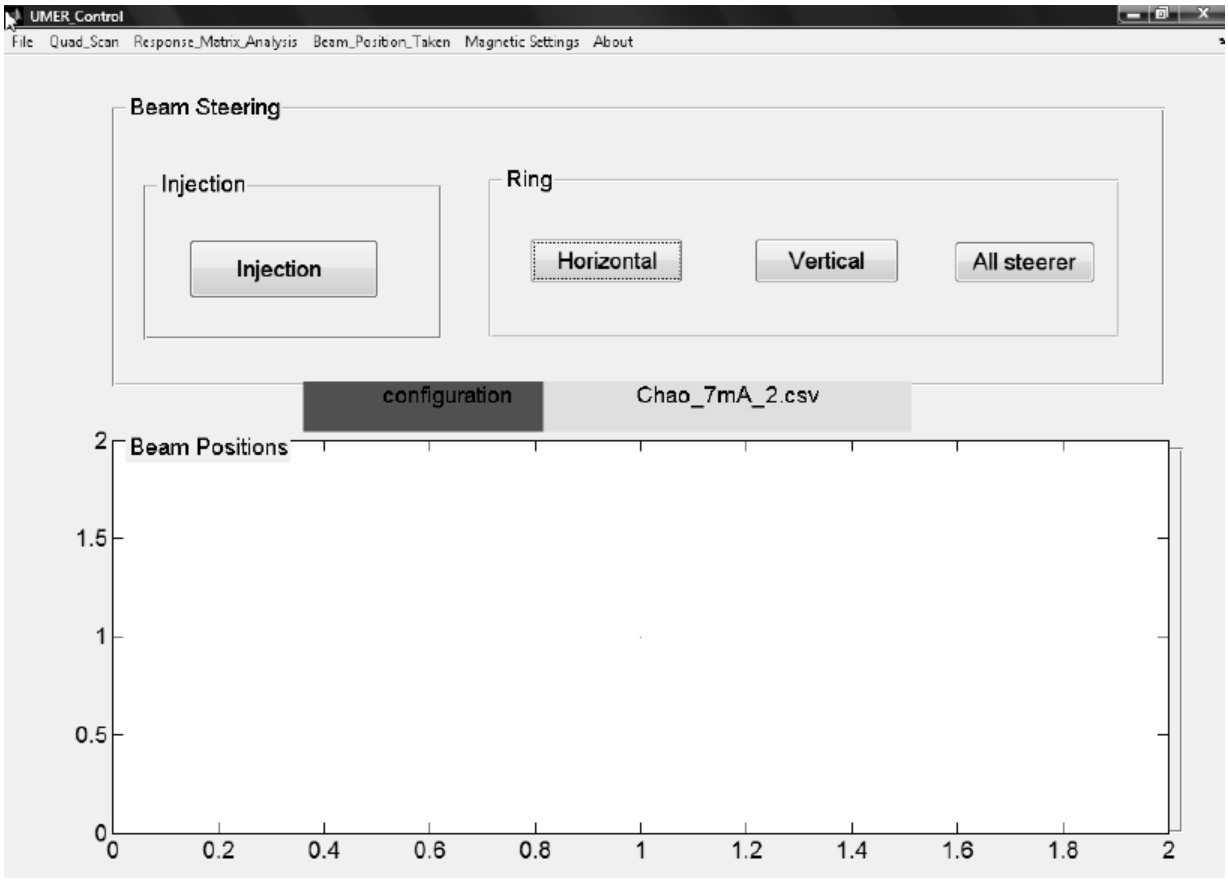

Figure A.2: UMER Control interface.

Appendix B

Beam Steering Solutions

The following tables summarize the best steering solutions for UMER that were obtained using the methods presented in Chapter 5.

Table B.1: Best steering solutions of ring horizontal bending dipoles at 83% operating point.

Name	pencil	7mA	23mA	80mA	100mA	Name	pencil	7mA	23mA	80mA	100mA
D1	2.411	2.750	2.892	2.483	2.483	D19	2.244	2.257	2.257	2.240	2.240
D2	2.437	2.380	2.280	2.695	2.695	D20	2.800	2.835	2.863	2.929	2.929
D3	2.462	2.650	2.712	2.636	2.636	D21	2.700	2.641	2.641	2.811	2.811
D4	2.504	2.750	2.831	2.540	2.540	D22	1.700	1.850	1.778	1.758	1.758
D5	2.552	2.536	2.536	2.599	2.599	D23	1.800	2.050	2.100	2.013	2.013
D6	2.584	2.470	2.470	2.521	2.521	D24	2.238	2.443	2.443	2.467	2.467
D7	2.584	2.577	2.577	2.597	2.597	D25	2.226	2.318	2.318	2.391	2.391
D8	2.552	2.594	2.594	2.515	2.515	D26	2.239	2.492	2.492	2.474	2.474
D9	2.499	2.498	2.498	2.409	2.409	D27	2.277	2.443	2.443	2.454	2.454
D10	2.444	2.481	2.481	2.392	2.392	D28	2.320	2.463	2.463	2.382	2.382
D11	2.396	2.539	2.539	2.385	2.385	D29	2.348	2.407	2.407	2.382	2.382
D12	2.364	2.454	2.454	2.303	2.303	D30	2.364	2.194	2.194	2.317	2.317
D13	2.350	2.341	2.341	2.203	2.203	D31	2.382	2.321	2.321	2.423	2.423
D14	2.340	2.488	2.488	2.332	2.332	D32	2.398	2.598	2.598	2.504	2.504
D15	2.312	2.464	2.464	2.283	2.283	D33	2.404	2.347	2.347	2.434	2.434
D16	2.272	2.326	2.326	2.241	2.241	D34	2.000	2.004	2.004	1.973	1.973
D17	2.240	2.017	2.017	2.250	2.250	D35	1.800	1.807	1.807	2.024	2.024
D18	2.231	2.316	2.316	2.163	2.163						

Table B.2: Best steering solutions of ring vertical dipoles at 83% operating point.

Names	Pencil	7mA	23mA	80mA	100mA
RSV1	-0.524	-0.777	-0.415	-0.876	-0.876
RSV2	-0.395	0.573	-0.029	-0.144	-0.144
RSV3	-0.750	-0.956	-0.09	-1.421	-1.421
RSV4	-0.010	-0.712	-0.189	0.694	0.694
RSV5	-0.428	-0.487	-0.093	-0.25	-0.25
RSV6	-0.679	-0.105	0.114	0.118	0.118
RSV7	-0.137	0.375	0.137	0.132	0.533
RSV8	-0.535	0.078	-0.053	-0.252	0.148
RSV9	0.249	-0.186	-0.02	0.150	0.15
RSV10	-0.235	0.696	0.359	0.532	0.532
RSV11	0.375	-0.229	0.111	-0.85	-0.85
RSV12	0.145	0.210	0.215	0.496	0.496
RSV13	-0.652	-0.236	-0.216	-0.848	-0.835
RSV14	-0.258	-0.253	-0.283	-0.225	-0.225
RSV15	0.184	-0.807	-0.876	-0.827	-0.439
RSV16	-0.450	-0.618	-0.597	-0.758	-0.361
RSV17	0.432	0.356	0.356	0.448	0.44
RSV18	-0.258	0.135	0.135	-0.076	-0.076

Table B.3: Best steering solutions of injection dipoles at 83% operating point.

Names	Pencil	7mA	23mA	80mA	100mA
SD1H	-0.400	-0.200	-0.238	-0.800	-0.800
SD2H	-1.200	-1.250	-1.738	-1.355	-1.355
SD3H	0.400	0.400	0.493	-0.350	-0.350
SD4H	0.200	-0.950	-0.22	0.0350	0.0350
SD5H	1.100	0.850	0.846	0.685	0.685
SD6H	-1.500	-1.30	-1.594	-1.652	-1.652
SD1V	0.600	1.100	1.198	0.480	0.480
SD2V	-0.600	-0.800	-1.000	-0.559	-0.559
SD3V	0.300	-0.120	0.453	-0.699	-0.300
SD4V	-0.300	0.150	-0.268	-0.350	-0.350
SD5V	0.050	0.350	0.286	-0.056	-0.056
SD6V	0	0	0	0	0

Table B.4: Best steering solutions of pulsed dipoles at 83% operating point.

Names	Pencil	7mA	23mA	80mA	100mA
PD-Rec	14.5	14.5	13.5	10.4	10.4
PD-Inj	26	28	28	24.7	24.6

Appendix C

Beam Matching Solution

The following tables summarize the matching solutions for UMER beams that were obtained using the methods presented in Chapter 5.

Table C.1: Best matching solutions of ring quadrupoles at 83% operating point.

Name	pencil	7mA	23mA	80mA	100mA
Q1	0.15	1.83	1.28	1.37	1.28
Q2	0	2.09	2.04	2.12	2.10
Q3	0.54	2.17	1.93	1.84	1.83
Q4	1.80	1.75	1.84	1.66	1.60
Q5	2.12	1.54	1.96	1.81	1.71
Q6	2.15	1.86	1.86	1.86	1.86
QR1	6.00	5.80	5.00	5.60	5.60
QR2-71	1.826	1.826	1.826	1.826	1.826
YQ	8.0	8.6	7.5	8.6	8.6

Appendix D

Beam Position Data Processing

This Appendix discusses how the BPM data is processed to get the beam positions. As shown in Figure D.1, there are two red bold rectangular boxes in the second turn of the BPM signals.

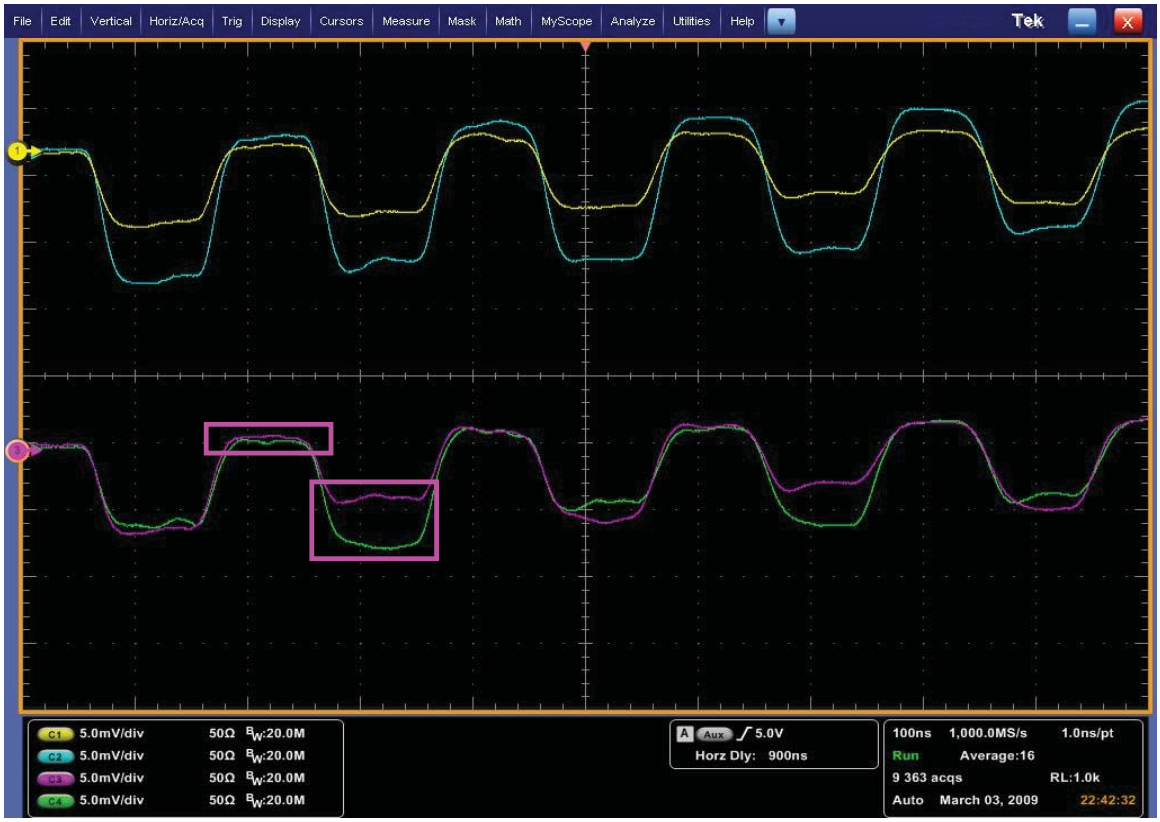

Figure D.1: Screenshot of typical BPM signals on an oscilloscope.

where the magneta rectangular boxes are not to scale.

Then, we take an average of the signals in the box window, subtract these two

average values and the resulting value is the BPM signal strength in that channel. The size of the window is flexible and should be adjusted adaptively to reflect the change of the beam pulse length. For the first four turns, the window size could be set around 60-80 ns for the 7 mA, 23 mA, 100 mA beams. For the pencil (0.7 mA) beam, the BPM signals in the first several turns are small and very sensitive to noise, and it needs special care. This windowing method is sensitive to the signal noise and the shape of the signal too.

Appendix E

Horizontal Response Matrix of the 7 mA Beam

This Appendix includes tables for the conventional horizontal response matrix and closed orbit response matrix for the 7mA beam of UMER.

Table E.1: Horizontal response matrix. The horizontal index is the BPM number (1-17) and the vertical index is the dipole number (1-35). x indicates no measurement at corresponding location. The quadrupoles were set at 83 % of the design values. To be continued at Table E.2.

index	1	2	3	4	5	6	7	8	9	10	11	12	13	14	15	16	17
1	-6.05	-8.29	14.79	x	0.16	12.59	-16.86	8.72	6.24	x	15.72	-0.88	-14.81	18.35	-10.24	x	15.95
2	0.09	-15.81	10.04	x	-14.62	15.58	-5.95	-9.73	18.41	x	-1.98	15.67	-18.10	6.54	8.41	x	14.58
3	0.11	-6.11	-6.95	x	-12.44	0.53	12.42	-16.75	8.79	x	-17.79	13.20	0.47	-14.25	14.67	x	-4.51
4	0.15	0.05	-16.60	x	4.92	-16.74	15.68	-3.19	-12.38	x	-10.58	-7.61	18.87	-16.08	1.38	x	-18.43
5	-0.01	0.06	-6.17	x	17.11	-13.84	-0.36	14.18	-18.13	x	9.58	-19.56	13.60	2.57	-16.54	x	-7.51
6	0.18	0.10	0.03	x	9.99	4.26	-15.52	15.67	-4.62	x	18.46	-11.58	-5.93	17.61	-17.76	x	10.68
7	0.03	0.04	0.01	x	-8.43	16.54	-14.04	0.02	14.35	x	8.80	8.83	-19.18	14.97	-0.96	x	17.72
8	0.01	0.07	0.06	x	-16.42	10.14	3.74	-16.17	16.98	x	-12.32	17.80	-11.49	-4.61	14.43	x	7.29
9	0.11	-0.03	0.00	x	-6.30	-8.93	17.71	-13.98	-0.74	x	-18.72	5.64	11.16	-19.15	11.63	x	-14.23
10	0.16	-0.03	-0.01	x	-0.09	-17.71	10.14	4.80	-16.77	x	-2.26	-14.29	18.77	-9.30	-6.99	x	-15.76
11	0.07	-0.02	0.10	x	-0.17	-6.40	-8.86	17.63	-14.14	x	16.18	-18.78	5.59	11.19	-20.02	x	1.20
12	0.08	-0.03	0.08	x	-0.14	0.03	-16.94	10.41	3.98	x	16.57	-3.52	-13.06	18.21	-11.85	x	14.92
13	0.12	-0.02	-0.05	x	-0.16	0.02	-6.42	-8.78	17.81	x	-1.32	15.04	-17.70	6.46	7.82	x	14.35
14	0.10	-0.06	0.06	x	-0.11	-0.01	0.12	-18.21	10.92	x	-18.43	14.93	-1.47	-13.66	15.71	x	-3.42
15	0.05	-0.10	0.02	x	-0.22	0.03	0.07	-6.94	-9.20	x	-13.95	-3.49	17.38	-17.79	4.92	x	-17.98
16	0.09	-0.05	0.13	x	-0.17	0.00	0.05	-0.11	-18.14	x	5.79	-18.50	16.06	-1.79	-13.67	x	-10.61
17	0.15	-0.10	0.00	x	-0.17	-0.01	0.11	-0.18	-6.93	x	17.89	-13.34	-3.21	15.87	-18.05	x	8.52

Table E.2: Horizontal response matrix. The horizontal index is the BPM number (1-17) and the vertical index is the dipole number (1-35). x indicates no measurement at corresponding location. The quadrupoles were set at 83 % of the design values. This table follows Table E.1.

index	1	2	3	4	5	6	7	8	9	10	11	12	13	14	15	16	17
18	0.15	-0.02	0.07	x	-0.11	0.09	0.12	-0.15	0.10	x	10.30	6.92	-18.30	15.34	-2.58	x	17.13
19	0.15	0.03	-0.04	x	-0.26	0.10	0.07	-0.17	0.13	x	-10.67	18.11	-13.76	-2.31	13.69	x	9.02
20	0.18	-0.09	0.09	x	-0.25	0.09	0.12	-0.28	0.05	x	-20.09	10.16	6.83	-18.35	14.04	x	-10.81
21	0.20	-0.02	-0.02	x	-0.20	0.06	0.07	-0.26	0.16	x	-7.68	-10.69	19.78	-14.05	-1.91	x	-18.17
22	0.08	-0.02	0.07	x	-0.29	0.10	0.05	-0.16	0.06	x	-0.17	-19.38	10.37	5.94	-17.76	x	-3.91
23	0.18	0.03	0.00	x	-0.19	-0.04	0.11	-0.25	0.09	x	-0.24	-7.12	-10.45	18.28	-14.74	x	13.55
24	0.15	0.00	0.06	x	-0.24	0.07	-0.01	-0.18	0.11	x	-0.31	0.30	-19.10	10.85	3.89	x	16.27
25	0.08	0.07	0.02	x	-0.17	0.11	0.13	-0.16	0.10	x	-0.33	0.26	-7.38	-9.11	15.79	x	2.74
26	0.19	-0.02	0.06	x	-0.34	0.10	0.07	-0.21	0.23	x	-0.24	0.23	-0.24	-19.55	10.11	x	-15.54
27	0.19	0.00	-0.01	x	-0.24	0.06	0.13	-0.18	0.15	x	-0.32	0.27	-0.15	-7.52	-8.94	x	-15.14
28	0.11	0.07	0.05	x	-0.22	0.11	0.09	-0.21	0.17	x	-0.23	0.23	-0.27	-0.12	-18.64	x	3.78
29	0.16	-0.06	0.10	x	-0.21	0.03	0.04	-0.18	0.13	x	-0.18	0.25	-0.33	-0.24	-6.76	x	16.62
30	0.19	-0.05	0.02	x	-0.28	0.04	0.04	-0.22	0.15	x	-0.23	0.32	-0.41	-0.11	0.26	x	12.25
31	0.21	-0.03	-0.05	x	-0.29	0.12	0.15	-0.21	0.18	x	-0.24	0.27	-0.18	-0.25	0.18	x	-6.80
32	0.16	-0.05	0.08	x	-0.31	0.14	0.06	-0.14	0.14	x	-0.26	0.31	-0.31	-0.21	0.29	x	-18.43
33	0.22	-0.16	0.10	x	-0.09	0.09	0.09	-0.20	0.13	x	-0.36	0.23	-0.18	-0.10	0.56	x	-6.67
34	-0.18	-0.24	0.02	x	-0.27	0.03	-0.12	-0.14	0.23	x	-0.05	0.42	-0.06	0.07	0.36	x	0.34
35	0.09	-0.99	0.81	x	-1.04	1.02	-0.65	-0.36	1.09	x	0.12	1.44	-1.39	0.68	0.71	x	1.40

Table E.3: Horizontal closed orbit response matrix. The horizontal index is the BPM number (1-17) and the vertical index is the dipole number (1-35). "x" indicates no measurement at corresponding location. The quadrupoles were set at 83 % of the design values. To be continued at Table E.4.

index	1	2	3	4	5	6	7	8	9	10	11	12	13	14	15	16	17
1	-1.68	-4.92	6.64	x	-0.31	5.47	-7.10	3.41	1 2.49	x	6.13	-0.12	-6.30	7.90	-5.98	x	7.63
2	-3.89	-8.36	3.77	x	-8.12	6.79	-1.91	-5.39	2 8.39	x	-1.88	8.14	-7.88	1.94	4.37	x	6.78
3	-7.06	-3.69	-3.29	x	-6.63	0.96	5.70	-8.92	3 4.74	x	-8.76	7.35	-0.24	-7.31	8.45	x	-2.08
4	-0.91	-6.10	-7.75	x	2.02	-7.42	7.12	-1.75	4 -5.12	x	-5.15	-2.46	8.49	-8.16	1.16	x	-9.37
5	7.00	-7.46	-3.52	x	8.45	-6.79	0.18	6.56	5 -9.09	x	4.14	-9.14	7.11	0.76	-8.42	x	-4.41
6	7.34	-0.91	-5.77	x	4.44	1.69	-6.81	6.81	6 -1.50	x	7.79	-4.98	-2.38	7.85	-9.18	x	5.15
7	0.35	6.03	-8.13	x	-4.87	7.52	-5.48	-1.13	7 6.87	x	2.89	5.17	-8.60	5.92	-0.75	x	8.70
8	-6.98	6.12	-1.75	x	-8.62	4.51	2.44	-8.31	8 7.91	x	-6.71	9.29	-5.10	-3.32	8.16	x	3.12
9	-5.82	-10.00	7.64	x	-3.59	-2.45	7.85	-6.75	9 0.32	x	-9.11	3.74	5.55	-9.81	6.43	x	-6.74
10	2.96	-7.33	6.82	x	-5.18	-9.70	4.70	2.31	10 -7.87	x	-1.27	-6.26	8.37	-4.88	-3.46	x	-8.49
11	8.41	-4.53	-1.84	x	-7.11	-3.41	-3.92	8.20	11 -7.30	x	7.06	-8.68	3.04	4.98	-10.00	x	0.23
12	4.83	2.57	-7.74	x	-1.81	-5.20	-7.17	3.69	12 2.31	x	6.46	-0.45	-6.41	8.11	-6.20	x	7.79
13	-3.69	7.05	-5.91	x	5.91	-7.61	-2.28	-5.20	13 8.51	x	-1.49	8.18	-8.29	2.42	4.16	x	6.91
14	-3.92	3.14	3.19	x	6.50	-0.55	-5.66	-8.22	14 5.41	x	-9.02	7.94	-1.00	-7.09	8.49	x	-1.50
15	-2.52	-4.98	8.63	x	-1.22	7.74	-8.25	-3.09	15 -3.88	x	-6.67	-0.85	7.90	-9.06	2.85	x	-10.00
16	6.06	-7.03	3.41	x	-6.82	7.53	-1.07	-5.03	16 -8.81	x	2.85	-8.65	7.85	-0.79	-6.96	x	-5.46
17	7.50	-1.27	-5.59	x	-5.14	-1.51	6.05	-7.62	17 -3.31	x	7.89	-5.55	-1.74	7.66	-9.23	x	4.79

Table E.4: Horizontal closed orbit response matrix. The horizontal index is the BPM number (1-17) and the vertical index is the dipole number (1-35). "x" indicates no measurement at corresponding location. The quadrupoles were set at 83 % of the design values. This table continues with Table E.3.

index	1	2	3	4	5	6	7	8	9	10	11	12	13	14	15	16	17
18	1.05	5.67	-8.12	x	2.24	-7.59	6.16	-2.75	18 -4.74	x	3.43	4.75	-8.87	6.66	-1.48	x	8.71
19	-6.39	6.78	-2.94	x	7.86	-6.07	-0.14	6.52	19 -7.99	x	-5.62	9.40	-6.43	-1.55	7.43	x	4.40
20	-6.86	0.14	6.31	x	4.26	3.17	-8.12	7.89	20 -1.22	x	-9.88	5.58	3.02	-9.39	7.38	x	-5.13
21	0.86	-6.94	8.06	x	-4.04	8.72	-6.59	-0.13	21 6.96	x	-3.52	-4.47	9.19	-7.04	-0.89	x	-9.35
22	7.66	-5.95	0.04	x	-7.19	4.51	2.11	-7.04	22 7.15	x	-5.46	-8.91	4.92	3.16	-9.32	x	-1.76
23	5.96	1.54	-7.66	x	-2.99	-4.52	7.16	-6.91	23 0.68	x	-7.98	-2.21	-5.49	8.72	-7.69	x	7.53
24	-1.93	6.77	-7.17	x	4.55	-8.12	4.62	0.37	24 -6.97	x	-2.79	-4.43	-8.92	4.33	2.36	x	8.04
25	-3.49	5.25	0.09	x	7.68	-3.47	-3.20	7.58	25 -6.62	x	6.47	-7.99	-3.51	-5.03	8.63	x	1.48
26	-4.98	-2.77	8.19	x	1.20	6.14	-8.80	5.38	26 2.18	x	7.68	-0.24	-7.30	-9.85	5.56	x	-7.59
27	4.13	-7.69	6.00	x	-6.06	8.09	-3.69	-3.37	27 8.19	x	-0.35	7.16	-9.14	-3.48	-4.79	x	-7.87
28	7.74	-3.08	-3.71	x	-5.96	0.59	4.89	-7.55	28 4.61	x	-7.38	6.96	-1.20	-5.36	-9.73	x	2.53
29	2.46	5.07	-8.72	x	0.79	-7.50	6.95	-4.02	29 -3.84	x	-6.32	0.13	6.74	-7.97	-3.13	x	9.15
30	-5.35	7.30	-5.00	x	7.25	-7.40	1.85	4.66	30 -8.33	x	1.57	-7.66	7.09	-2.08	-4.64	x	6.09
31	-4.79	1.88	4.50	x	5.66	1.06	-6.88	8.06	31 -3.14	x	8.32	-5.39	-1.55	7.98	-7.70	x	-3.07
32	-1.09	-6.26	8.80	x	-2.53	8.46	-7.78	1.61	32 5.77	x	4.69	3.72	-9.50	8.09	-0.74	x	-8.98
33	7.17	-6.08	0.96	x	-6.84	4.96	1.18	-6.23	33 7.22	x	-4.89	7.76	-5.49	-1.77	5.48	x	-2.88
34	6.23	1.50	-8.06	x	-3.09	-4.76	7.38	-6.82	34 0.47	x	-8.16	4.09	4.10	-8.22	4.93	x	-4.86
35	-1.66	7.16	-7.83	x	4.29	-8.65	5.28	-0.41	35 -7.01	x	-3.46	-4.03	7.83	-6.18	-0.25	x	-7.79

Bibliography

[1] R.O. Bangerter, *"The Induction Approach to Heavy-Ion Inertial Fusion: Accelerator and Target Considerations,"* Nuovo Cimento A 106, N 11, pp 1445-1446, 1993.

[2] R.A. Kishek, S. Bernal, Y. Cui, T.F. Godlove, I. Haber, J. Harris, Y. Huo, H. Li, P.G. O'Shea, B. Quinn, M. Reiser, M. Walter, M. Wilson, and Y. Zou, *"HIF Research on the University of Maryland Electron Ring (UMER),"* Nuclear Instruments and Methods in Physics Research Section A, 544, pp 179-186, 2005.

[3] P.G. OShea and H.P. Freund, *"Free-Electron Lasers: Status and Applications,"* Science, 292, pp 1853-1858, 2001.

[4] A. Sessler and E. Wilson, *Engines of Discovery: A Century of Particle Accelerators,* World Scientific Publishing Company, Singapore, 2007.

[5] H. Wiedemann, *Particle Accelerator Physics I, Basic Principles and Linear Beam Dynamics,* 2nd edition, Springer-Verlag Berlin Heidelberg New York, 2003.

[6] E. Wilson, *An Introduction to Particle Accelerators,* Oxford University Press Inc., New York, 2001.

[7] M. Reiser, *Theory and Design of Charged Particle Beams,* Wiley-VCH Verlag GmbH & Co. KGaA, Weinheim, 2004.

[8] M. Venturini and R. Gluckstern, *"Resonance Analysis for a Space Charge Dominated Beam in a Circular Lattice,"* Physical Review Special Topics - Accelerators & Beams, V.3, 034203, 2000.

[9] R. Baartman, *"Betatron Resonances with Space Charge,"* AIP Conference Proceedings CP448, 1998.

[10] M. Reiser, P.G. O'Shea, R.A. Kishek, S. Bernal, S. Guharay, Y. Li, M. Venturini, J.G. Wang, V. Yun, W. Zhang, Y. Zou, M. Pruessner, T. Godlove, D. Kehne, P. Haldemann, R. York, D. Lawton, L.G. Vorobiev, I. Haber, and H. Nishimura, *"The Maryland Electron Ring for Investigating Space-Charge Dominated Beams in a Circular FODO System,"* Proceedings of the 1999 IEEE Particle Accelerator Conference, New York City, NY, 234, 1999.

[11] P.G. O'Shea, M. Reiser, R.A. Kishek, S. Bernal, H. Li, M. Pruessner, V. Yun, Y. Cui, W. Zhang, Y. Zou, T. Godlove, D. Kehne, P. Haldemann, and I. Haber,

"The University of Maryland Electron Ring (UMER)," Nuclear Instruments and Methods in Physics Research Section A, V 464, pp 646-652, 2001.

[12] S. Bernal, H. Li, T. Godlove, I. Haber, R.A. Kishek, B. Quinn, M. Reiser, M. Walter, Y. Zou, and P.G. O'Shea, *"Beam Experiments in the Extreme Space-Charge Limit on the University of Maryland Electron Ring (UMER),"* Physics of Plasmas, 11(5), 2907, 2004.

[13] R.A. Kishek, G. Bai, B. Beaudoin, S. Bernal, D. Feldman, R. Feldman, R. Fiorito, T.F. Godlove, I. Haber, T. Langford, P.G. O'Shea, B. Quinn, C. Papadopoulos, M. Reiser, D. Stratakis, D. Sutter, K. Tian, J.C.T. Thangaraj, M. Walter, and C. Wu, *"The University of Maryland Electron Ring (UMER) Enters a New Regime of High-Tune-Shift Rings,"* Proceedings of the 2007 IEEE Particle Accelerator Conference, Albuquerque, NM, ed. C. Petit-Jean-Genaz, IEEE Cat. No. 07CH37866, 820, 2007.

[14] A. U. Luccio, *"Computer Study of Harmonic Orbit Correction in the AGS Booster,"* AD Booster Technical Note, No. 131, Oct. 1988.

[15] A. Friedmann and E. Bozoki, *"Eigenvector Method for Optimized Orbit Correction",* AIP Conference Proceedings, 315, Upton, NY, 1993.

[16] J. Safranek, *"Experimental Determination of Storage Ring Optics Using Orbit Response Measurements,"* Nuclear Instruments and Methods in Physics Research A, 388, pp 27-36, 1997.

[17] J. Safranek, *"Linear Optics from Closed Orbits (LOCO)–An Introduction,"* Beam Dynamics Newsletter, No. 44, International Committee for Future Accelerators, Issue Editor A. Ghodke, Editor in Chief: W. Chou, Dec. 2007.

[18] H. Li, *"Control and Transport of Intense Electron Beams,"* PhD dissertation, Department of Electrical and Computer Engineering, University of Maryland, College Park, 2004.

[19] M. Walter, G. Bai, S. Bernal, D. Feldman, T. Godlove, I. Haber, M. Holloway, R.A. Kishek, P.G. O'Shea, C. Papadopoulos, B. Quinn, M. Reiser, D. Stratakis, D. Sutter, J. Thangaraj, M. Wilson, and C. Wu, *"Beam Control and Steering in the University of Maryland Electron Ring (UMER),"* Proceedings of 12th Workshop on Advanced Accelerator Concepts (AAC), Lake Geneva, WI, 10-15 July, 2006.

[20] M. Walter, G. Bai, B.L. Beaudoin, S. Bernal, D. Feldman, T. Godlove, I. Haber, R.A. Kishek, P.G. O'Shea, C. Papadopoulos, B. Quinn, M. Reiser, D.

Stratakis, D. Sutter, J.C.T. Thangaraj, and C. Wu, *"Multi-turn Operation at the University of Maryland Electron Ring (UMER),"* Proceedings of the 2007 IEEE Particle Accelerator Conference, Albuquerque, New Mexico, 2007.

[21] R.A. Kishek, Private Communication, 2009.

[22] D.P. Grote, A. Friedman, I. Haber, W. Fawley and J.L. Vay, *"New Developments in WARP: Progress Toward End-to-End Simulation,"* Nuclear Instruments and Methods in Physical Research A, 415, pp 428-432, 1998.

[23] S. Bernal, D. Sutter, M. Cornacchia, B. Beaudoin, I. Haber, R.A. Kishek, M. Reiser, C. Wu, and P.G. O'Shea, *"Operational Studies of the 10 keV Electron Storage Ring UMER,"* Proceedings of 13th Workshop on Advanced Accelerator Concepts (AAC), p. 738-740, Santa Cruz, CA, July/Aug, 2008.

[24] C. Wu, E.H. Abed, B. Beaudoin, S. Bernal,I. Haber, R.A. Kishek, C. Papadopoulos, M. Reiser, D. Sutter, and P.G. O'Shea, *"Linear Resonance Analysis of Beams with Intense Space Charge in the UMER,"* 42nd ICFA Advanced beam dynamics workshop on high-intensity, high-brightness hadron beams, Nashville, TN, 2008.

[25] C. Wu, E.H. Abed, B. Beaudoin, S. Bernal, I. Haber, R.A. Kishek, C. Papadopoulos, M. Reiser, D. Sutter, J. Thangaraj and P.G. O'Shea, *"Error and Resonance Analysis of Beams with Intense Space Charge in the University of Maryland Electron Ring,"* Presentation at 2008 Advanced Accelerator Concepts Work, Santa Cruz, CA, 2008.

[26] M. Borland, *"Elegant: A Flexible SDDS-Compliant Code for Accelerator Simulation,"* Advanced Photon Source, LS-287, September, 2000.

[27] S. Bernal, H. Li, R.A. Kishek, B. Quinn, M. Walter, M. Reiser, P.G. OShea, and C.K. Allen, *"RMS Envelope Matching of Electron Beams from "Zero" Current to Extreme Space Charge in A Fixed Lattice of Short Magnets,"* Physical Review Special Topical– Accelerator Beams, No. 9, 064202, 2006.

[28] C. Wu and R.A. Kishek, *"Investigation on YQ and QR_1,"* UMER Technical Notes UMER-090310-CW, IREAP, University of Maryland, unpublished, 2009.

[29] M.G. Minty and F. Zimmermann, *Measurement and Control of Charged Particle Beams,* Springer-Verlag, Berlin Heidelberg, 2003.

[30] W.S. Levine, (Editor), *The Control Handbook,* CRC press, 1996.

[31] B. Beaudoin, *"Longitudinal Space-Charge Waves Induced by Energy Modulations,"* Master thesis, Department of Electrical and Computer Engineering, University of Maryland, College Park, MD, 2008.

[32] E.D. Courant and H.S. Snyder, *"Theory of the Alternating-Gradient Synchrotron (reprinted),"* Annals of Physics, Volume 281, Issue 1-2, pp 360-408, 2000.

[33] S.Y. Lee, *Accelerator Physics,* 2nd Edition, World Scientific Publishing Co., 2004.

[34] R. Bartolini, M. Giovannozzi, W. Scandale, A. Bazzani and E. Todesco, *"Algorithms for A Precise Determination of the Betatron Tune,"* Proceedings of the 1996 European Particle Accelerator Conference, 1996.

[35] H. Li, Private Communication, 2008.

[36] J. Koutchouk, *"Trajectory and Closed Orbit Correction,"* Frontiers of Particle Beams: Observation, Diagnosis and Correction, Proceedings, Anacapri, Isola di Capri, Italy, (Lectures Notes in Physics 343, M. Month, S. Turner Eds), p 46, 1988.

[37] R.A. Kishek, I. Haber, M. Venturini and M. Reiser, *"PIC Code Simulations of Collective Effects in the Space-Charge-Dominated Beam of the University of Maryland Electron Ring (UMER),"* Proceedings of the 1999 IEEE Particle Accelerator Conference, New York City, NY, 1999.

[38] W.J. Corbett, M.J. Lee, and V. Ziemann, *"A Fast Model Calibration Procedure for Storage Rings",* SLAC Report, SLAC-PUB-6111, May, 1993.

[39] D. Robin, J. Safranek, W. Decking, *"Realizing the Benefits of Restored Periodicity in the Advanced Light Source,"* Physical Review Special Topics- Accelerators & Beams, V. 2, 044001, 1999.

[40] H. Nishimura and M. Walter, *Notes on a Measured Smatrix,* UMER Technical Notes, UMER-LON-001, Sept. 12, 2005.

[41] T. Tenenbaum, T.O. Raubenheimer, *"Resolution and Systematic Limitations in Beam-Based Alignment,"* Physical Review Special Topics-Accelerator and Beams, V.3, 052801, 2000.

[42] D. Sutter, Private Communication, 2009.

[43] H. Li, S. Bernal, T. Godlove, Y. Huo, R.A. Kishek, I. Haber, B. Quinn, M. Walter, Y. Zou, M. Reiser, and P.G. O'Shea, *"Beam Control and Matching for the Transport of Intense Beams,"* Nuclear Instruments and Methods in Physics Research Section A, 544, pp 367-373, 2005.

[44] D. Stratakis, *"Tomographic Measurement of the Phase-Space Distribution of a Space-Charge-Dominated Beam,"* PhD dissertation, Department of Electrical and Computer Engineering, University of Maryland, College Park, 2008.

[45] D.P. Rusthoi and K.R. Crandall, *"TRACE 3-D Documentation,"* LA-UR-97-886, LANL, 1997.

[46] C. Wu, *"Report on the Injection Quadrupole Scan,"* UMER Technical Notes UMER-081114-CW, IREAP, University of Maryland, unpublished, 2008.

[47] C. Wu, E.H. Abed, B. Beaudoin, S. Bernal,I. Haber, R.A. Kishek, C. Papadopoulos, M. Reiser, D. Sutter, and P.G. O'Shea, *"A Robust Orbit-Steering and Control Algorithm Using Quadrupole-Scans as a Diagnostic,"* Proceedings of the 2007 IEEE Particle Accelerator Conference, Albuquerque, New Mexico, 2007.

[48] C. Wu and R.A. Kishek, *"Note on Measured Response Matrix of UMER,"* UMER Technical Note UMER-090125-CWRK, IREAP, University of Maryland, unpublished, 2009.

[49] C. Wu and R.A. Kishek, *"Note on Measured Response Matrix of UMER (2),(3),(4),"* UMER Technical Notes UMER-090125-CWRK, UMER-090202-CWRK, UMER-090218-CWRK, IREAP, University of Maryland, unpublished, 2009.

[50] C. Wu and R.A. Kishek, *"Summary of Meeting on Tune Computation,"* UMER Technical Note UMER-081028-CWRK, IREAP, University of Maryland, unpublished, 2008.

[51] F. Li, M. C. Oliveira and R. Skelton *"Integrating information architecture and control or estimation design,"* SICE Journal of Control, Measurement, and System Integration, Vol 1. No. 2, pp. 12-128, March 2008.

[52] P. Marchand, *Graphics and GUIs with Matlab,* 2nd edition, CRC Press, 1999.